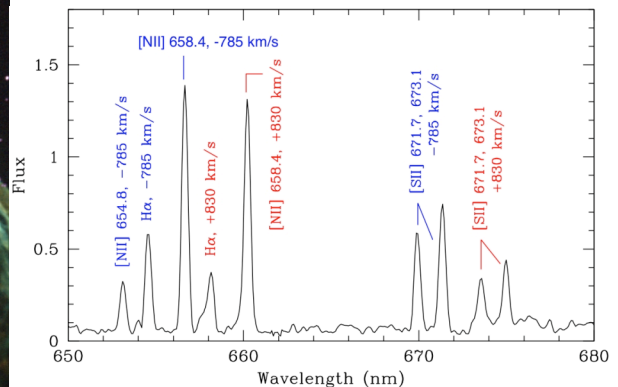


SITELLE

(Spectromètre Imageur à Transformée de Fourier
pour l' Etude en Long et en Large
de raies d'Emission)



A wide-field imaging Fourier transform spectrometer
for the Canada-France-Hawaii Telescope



Feasibility Study - October 1st, 2008



Science team :

Laurent Drissen, Université Laval, PI

Département de physique, de génie physique et d'optique
1045 avenue de la médecine, Université Laval, Québec, Qc
G1V 0A6 Canada
Phone : (418) 656 2131 ext. 5641 Fax : (418) 656 2040
ldrissen@phy.ulaval.ca

Jean-Pierre Maillard, Institut d'Astrophysique de Paris

Anne-Pier Bernier, Université Laval

François Boulanger, IAS

Maxime Charlebois, Université Laval

Daniel Devost, Canada-France-Hawaii Telescope

Daniel Durand, Herzberg Institute of Astrophysics

Gilles Joncas, Université Laval

Carmelle Robert, Université Laval

Luc Simard, Herzberg Institute of Astrophysics

Simon Thibault, Université Laval (Optical design)

Juan Zorec, Institut d'Astrophysique de Paris

Technical & engineering team, ABB Bomem:

Henry Buijs	Chief Technology Officer
Frederic Grandmont	System Engineer
Stephane Lantagne	System Scientist
Martin Larouche	Optical Engineer
Fabien Lalisie	Mechanical designer
Louis-Phillipe Bibeau	Mechanical Engineer
Sylvio Laplante	Electronic Engineer
Gaetan Perron	Project Manager

Executive summary

This document describes the concept of a new instrument for the CFHT, SITELLE (Spectromètre Imageur à Transformée de Fourier pour l'Etude en Long et en Large de raies d'Emission), as well as a clear science case and a technical study of its preliminary design. SITELLE will be an imaging Fourier transform spectrometer capable of obtaining the visible (350 nm – 950 nm) spectrum of every source of light in a field of view of 14.4 arcminutes, with 100% spatial coverage and a spectral resolution ranging from $R = 1$ (deep panchromatic image) to $R = 10^4$ (for gas dynamics). SITELLE will cover a field of view 100 to 1000 times larger than traditional integral field spectrographs, such as GMOS-IFU on Gemini or the future MUSE on the VLT. It is a legacy from BEAR, the first imaging FTS installed on the CFHT and the direct successor of SpIOMM, a similar instrument attached to the 1.6-m telescope of the Observatoire du Mont-Mégantic in Québec. SITELLE will be used to study the properties of comets, the structure and kinematics of HII regions and ejecta around evolved stars in the Milky Way, emission-line stars in clusters, abundances in nearby gas-rich galaxies, and the star formation rate in distant galaxies.

1 - Introduction

1.1 – The imaging FTS in context

There are basically two traditional approaches to obtaining spectral information on extended astrophysical objects. Imagery with filters allows the observer to map a target in selected wavelength ranges and to extract the required physical information by comparing the relative flux of the sources in these bands. This technique is used to obtain color-magnitude diagrams of star clusters or resolved galaxies (Johnson UBVRI broad-band filters for example), or to map abundance, temperature or density gradients in nebulae or gas-rich galaxies (using narrow-band interference filters centered on specific emission lines such as H α , [NII] or [OIII]). Images of the targets in the different band passes must be obtained one after the other, rejecting each time all photons excluded by the selected filters (up to 99.8%). Moreover, this technique is severely limited in terms of spectral resolution and is limited to face-on galaxies. Dispersive spectroscopy with slits allows a much finer spectral resolution at the expense of spatial information on the targets. The use of multi-object spectrographs (Sloan ^[1] ; 2dF ^[2]) and integral field spectrographs (GMOS-IFU on Gemini ^[3] , or VIMOS-IFU ^[4]) on large telescopes has revolutionized data collection by allowing respectively to obtain spectra of a large number (up to 1000) of objects dispersed in a large field or to spatially sample relatively small (of the order of 10 arcseconds) objects. An integral field spectrograph allowing observations across a relatively large field of view (41 x 33 arcseconds at a spectral resolution $R \sim 1000$), SAURON ^[5] , has revolutionized the study of late-type galaxies ^[6] , and a similar, but much more complex, instrument, MUSE, is being built for the VLT. High spectral resolution of single lines are also performed with instruments such as Fabry-Perot interferometers ^[7] to determine, for instance, the rotation curves of galaxies.

A large number of research programs (see Section 2 below) would benefit from an instrument capable of simultaneously obtaining spatially resolved, high quality spectra on extended areas (of the order of 10 arcminutes) and with a resolution up to $R \sim 10^4$. Fourier transform imaging spectroscopy is very promising in that regard. Based on the principle of the Michelson interferometer, Fourier Transform Spectrometers (FTS) are extremely efficient because all photons are collected and analysed. Moreover, by using appropriate optical configurations, it is possible to transform the traditional one-pixel FTS into a truly integral field spectrometer ^[8] . Although FTS are most widely used in military and chemical industries, they have also been very successful in planetary exploration (on board the Mariner, Voyager and more recently Cassini spacecrafts ^[9]) and in the analysis of the Earth's atmosphere (a recent example being the ACE-FTS instrument on board the SCISAT-1 remote sensing Canadian satellite ^[10]). The use of FTS in astronomy is not widespread, mostly because of the technical difficulties in building such instruments, but some examples need to be mentioned. The FTS at Kitt Peak's Mayall telescope was used the 1970's and 1980's to provide exquisite spectra of late-type stars ^[11a,11b] . At the CFHT (see section 1.2), the high-resolution FTS was widely used on a large variety of planetary and stellar programs. Made able to work on an imaging mode in the early 1990's, the called BEAR, it provided integral field spectra such as planetary nebulae, massive star clusters and star-forming regions in a 24 arcsecond field of view ^[11c] , see section 1.2. Other examples include the FTS built by D. Naylor (U. Lethbridge) on the JCMT ^[11d,11e] , an FTS for SPIRE, one of three instruments to fly on ESA's Herschel Space Observatory ^[12] , a far-infrared FTS on the Japanese satellite AKARI, a mid-IR FTS (CIRS) on the Cassini spacecraft and for the near-IR, PFS on Mars Express with a copy on Venus Express. We should also mention another imaging FTS prototype, working in the visible part of the spectrum that was built at the Lawrence Livermore Lab ^[13] , but which development ceased about a few years ago for lack

of funding. The advantages and disadvantages of the imaging FTS technique, as well as the relative merit of different approaches to 3-D imagery are discussed by Ridgway & Brault ^[14] and, more recently, by Bennett ^[15]. The development of imaging FTS in astronomy was given a strong incentive during the early definition phases of the NGST (now known as the James Webb Space Telescope): astronomers supported by the three participating space agencies (NASA, ESA and the Canadian Space Agency) presented studies of imaging FTS at the NGST Instrumentation meeting in Hyannis in 1999 september ^[16, 17, 18].

1.2 - History of Fourier transform spectroscopy at CFHT

The adventure of the FTS at CFHT, according to the title of a presentation made by Maillard at the CFHT User's meeting in May 2001, started in Oct. 1977 when a convention to build a high resolution Fourier transform spectrometer for the infrared domain (1 – 5 μ m) was signed between the CFH Corporation and CNRS. This was based on the experienced previously gained with such an instrument at the OHP 193-cm telescope and with a visiting instrument on 5-m Palomar telescope. The new FTS, capable of a resolution up to 5×10^5 at 2 μ m (60 cm maximum optical path difference), was delivered at Mauna Kea in Jul. 1980. However, it was able to really start its scientific life only in 1983 when the f/35 infrared Cassegrain focus, for which it was designed, was fully ready. Some highlights of the FTS in the high-resolution mode were the first detection of the molecular ion H_3^+ in the Jovian aurorae ^[20], the spectroscopy of the Venus night-side ^[21], and the detection of the hot and cold gas on the line of sight of a set of embedded high-mass young stellar objects ^[22]. In parallel, the possibility of adapting the FTS to an imaging mode was considered as early as 1990 with a first test with a CCD camera. The instrument being initially built with a step-by-step data acquisition mode, it was potentially easy to adapt it to this mode. Besides an optical coupling of the camera to the FTS, a synchronization of the camera data recording with the scanning of the optical path difference of the interferometer had to be made. The final mode, named BEAR, to continue with the tradition of multi-object spectrometers at the CFHT as PUMA and TIGER, was developed with the near infrared CFHT camera Redeye equipped with a 256x256 HgCdTe mosaic. An optical interface imaged the two output beams side-by-side on the single camera, using 128x256 pixels. Since the FTS was not initially designed for the imaging mode, the field of view was small, 24'' in diameter, but with all the capabilities of resolution of the instrument.

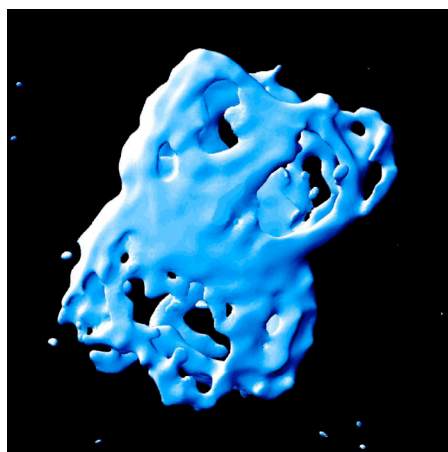


Figure 1 – 3D representation of the H_2 1-0 S(1) emission in the young planetary nebula NGC 7027 from BEAR data ^[19]. The view shows surface contours of the H_2 as seen from the front.

The operation of the BEAR mode, completed by the full development of the specialized data reduction package, really started in mid-1996 and was available until the decommissioning of the infrared focus at the beginning of 2001, which meant the end of the FTS. The main astronomical targets for BEAR were the planets Venus and Jupiter, young planetary nebulae (Figure 1), reflection nebulae, star forming regions, the inner region of the Galactic Center, providing on all these sources unique results with spectral imagery at 10 km/s resolution in the K band ^[11c,23,24]. With the capability of shifting back and forth from the standard mode to the imaging mode the FTS at CFHT had a versatility which explains its unique longevity. It triggered numerous collaborations between the members of the three CFH scientific communities. The BEAR instrument opened the door to another method of doing integral field spectroscopy, which can be continued by the access to a wide field, a specific property of an imaging FTS, which will be fulfilled by SITELLE.

1.3 – SPIOMM as a prototype

The design of SITELLE will directly benefit from our combined experience with BEAR and SpIOMM (**S**pectromètre **I**mageur de l'**O**bservatoire du **M**ont-**M**égantic), an imaging Fourier transform spectrometer attached to the bonnette of the 1.6-m telescope of the Mont Mégantic Observatory (OMM) in southern Québec. Because SITELLE will essentially be an improved version of SpIOMM, working in the same wavelength range, we present in this section the main characteristics of SpIOMM, its concept and some science highlights to provide the reader with a flavor of what to expect from SITELLE.

SpIOMM is capable of obtaining the entire visible spectrum (from 350 to 850 nm) of every light source in a 12 arcminute (circular) field of view of the 1.6-m OMM telescope. The spectral resolution is variable, depending on the need of the observer, from $R = 1$ (broad-band image) to $R = 25\,000$; the spatial resolution is limited by the seeing (pixel size = $0.5''$; CCD camera as detector with 1340×1300 pixels), resulting in $\sim 10^6$ spectra. The dual input, dual output design of SpIOMM ensures that virtually every photon collected by the telescope reaches the detector and is analyzed; a by-product of the spectral data cubes is therefore a very deep panchromatic image of the targets. Its early development phase was presented by Grandmont, Drissen and collaborators ^[25 - 28].

SpIOMM was developed at Université Laval (F. Grandmont's Ph. D. thesis ; Plaskett medal for 2007) with close collaboration with ABB-Bomem, a world leader in the development FTS and Québec City-based Institut National d'Optique (INO), with grants from the Canadian Foundation for Innovation, NSERC, FQRNT and the Canadian Space Agency. Although SpIOMM saw first light in 2004, numerous stability and electronics problems inherent to a prototype postponed the acquisition of the first usable science cubes to early 2007. SpIOMM is unique in the world, offering the largest field of view of any integral field spectrograph; by comparison, Gemini's GMOS-IFU can sample a field of smaller than 10×10 arcseconds (4000 times smaller than SpIOMM) with a maximum resolution of $R = 5000$. Currently, only one output port is used on SpIOMM. The detector is a LN_2 -cooled, Princeton Instruments VersArray CCD, with 1340×1300 pixels covering a field of view of 12 arcminutes \times 12 arcminutes. The CCD is read at 100 kHz to reduce the readout noise and the pixels are binned 2×2 during readout to increase the S/N ratio and reduce the readout time.

After five years of research and development, we have demonstrated ^[27] that the concept behind SpIOMM is sound and viable, and that such an instrument is capable of producing high quality hyperspectral data cubes over a very extended field of view.

1.3.1 – The principle behind an imaging FTS

An imaging FTS is basically composed of a traditional camera coupled at its core with a Michelson interferometer. Spectral information is obtained by acquiring multiples panchromatic images of the scene that are modulated in intensity in a precisely controlled fashion. Figure 2 illustrates the imaging FTS *modus operandi*.

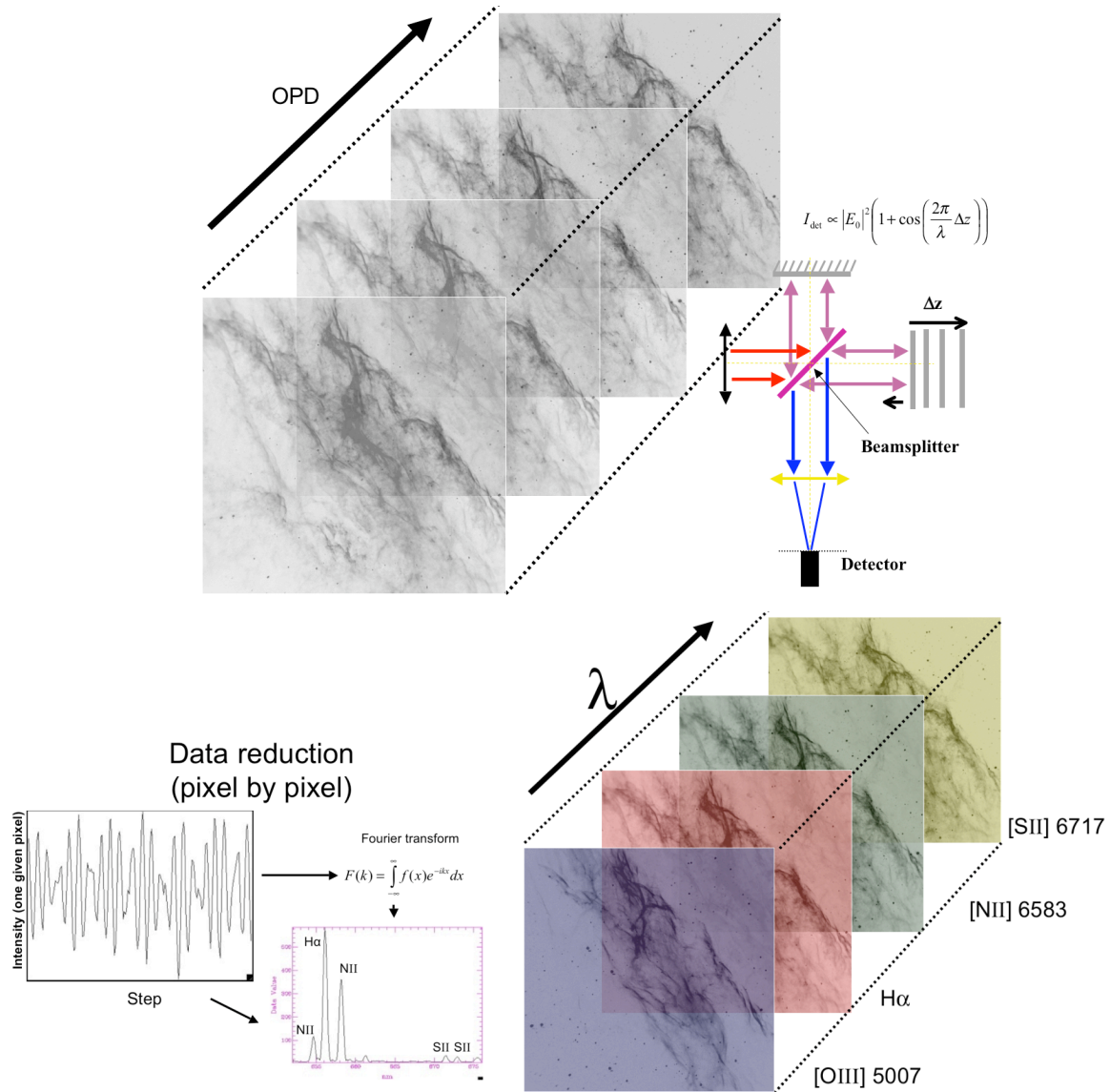


Figure 2 - Data acquisition with an imaging FTS. (a) By scanning the Optical Path Difference (OPD) of the interferometer and taking images at every step, one gets a datacube composed of one interferogram for every pixel. (b) For a given pixel, the recorded intensity varies as a function of the OPD with a pattern that depends on the spectral content of the source; for example, a monochromatic laser beam would produce a sinusoidal pattern. A Fourier transform of the signal produces a spectrum for every pixel in the image. (c) After Fourier transforming every interferogram, one gets a spectral datacube (RA, DEC, λ) from which monochromatic images corresponding to the emission lines of interest can be extracted.

The Michelson interferometer, inserted in series within the camera optical design, modulates the image intensity from total dark to total brightness according to the optical path difference (OPD) between the

two interferometer arms. This OPD being a function of wavelength, the resulting image intensity is the sum of all individual wavelength contributions. A recording of these panchromatic images generated at equally spaced OPD positions creates the raw data cube from which spectral information can be extracted.

A Fourier transform calculation performed on a given pixel intensity recording across the multiple images of the raw datacube leads to a spectrum. Repeating this calculation for every pixel of the detector leads to a 3D spectral data set, producing one spectrum for every pixel of the detector.

Spectral images are thus obtained without the need for image reconstruction, which increases the photometric and astrometric precision over standard IFU systems. Dual port interferometers provide access to the two complementary outputs. Their subtraction reconstructs the total incident flux of the interferogram and cancels the continuous term while their sum provides the total intensity of the sources, useful to monitor the sky transmittance over the data acquisition time.

1.3.2 – Some science results with SpIOMM

As we will see in the next section, the « niche » we have chosen for SpIOMM is the mapping of emission lines in extended gaseous regions in the nearby universe : nebulae in the Milky way, and large gas-rich galaxies. While the observations could be done without any filter, thereby covering the entire visible range (from 350 nm to 850 nm), we take advantage of the fact that our preferred targets emit most of their flux in a series of emission lines clustered around 500 nm and 660 nm (rest wavelength). The observations are therefore performed in two steps, with a blue (450 – 520 nm) and a red (650 – 680 nm) filter to cover the most intense and diagnostic-rich emission lines (listed in Table 1).

Table 1. Filter settings for SpIOMM

Filter	Blue (450 – 520 nm)	Red (650 – 680 nm)
Emission lines (λ_0 , nm)	He II 468.6 H β 486.1 [OIII] 485.9 [OIII] 500.7	[NII] 654.8 H α 656.3 [NII] 658.4 He I 667.8 [SII] 671.7 [SII] 673.1
Resolution ($\Delta\lambda$, nm)	0.9	0.3
Number of steps	180	325

The use of filters also significantly increases the contrast between the targets (nebulae) and the underlying continuum sources (stars) and dramatically reduces the background sky intensity, especially when the Moon is up. Table 1 summarizes the filter settings. The most important criterium to define the spectral resolution is the capacity to unambiguously separate the lines from the [SII] doublet (whose ratio is a good indicator of the gas density). Such a resolution also ensures a clear separation of the [NII] doublet from the strong H α line. On the red part, the line's full width at half maximum corresponds to ~ 130 km/s, but the centroid of each line can be determined with a precision better than 10 km/s, depending on the line strength, therefore allowing crude kinematical analysis of nebulae and rotation curves of galaxies. Exposure times vary from 7 seconds per step for the observations of bright nebulae in the red filter to 60 seconds per step for the observations of galaxies in the blue filter. A typical data cube

therefore requires a total exposure time between one and five hours. During four observing runs in 2007 – 2008, we have obtained about 30 datacubes of galactic HII regions, planetary nebulae, Wolf-Rayet ring nebulae, supernova remnants, nearby spiral galaxies and groups of interacting galaxies.

One of our first targets, the planetary nebula M27 (Figure 3) illustrates both the imaging and spectroscopic capabilities of an imaging FTS. Because of the high quality of its instrumental line shape, monochromatic images can be extracted from the data cubes to simulate the use of a perfect interference filter. The ratio map of $[\text{NII}] 658.4 / \text{H}\alpha 656.3$ as well as the BPT diagnostic diagram (Baldwin, Phillips & Terlevich ^[28b], see Figure 4) demonstrate the non-homogeneity of the physical conditions inside the nebula. This type of diagram is frequently used to characterize the ionization source of distant, often unresolved, nebulae or galaxies and classify them (as HII regions, liners, AGNs, ...). In most cases, every object in a BPT diagram is represented by a single point; each class of objects occupies a well-defined region. Truly wide-field integral spectroscopy such as provided by SpIOMM clearly shows that a single object actually samples a very wide range of physical conditions. The improved efficiency and light gathering power of SITELLE attached to the CFHT will allow us to probe fainter emission lines in nebulae (such as $[\text{OI}] 630.0 \text{ nm}$, $[\text{OII}] 372.7 \text{ nm}$, $[\text{OIII}] 436.3 \text{ nm}$ or $[\text{NII}] 575.5 \text{ nm}$), to better study their kinematics with an increased spectral resolution and to extend the spectroscopy to their much fainter halo (see section 2.3).

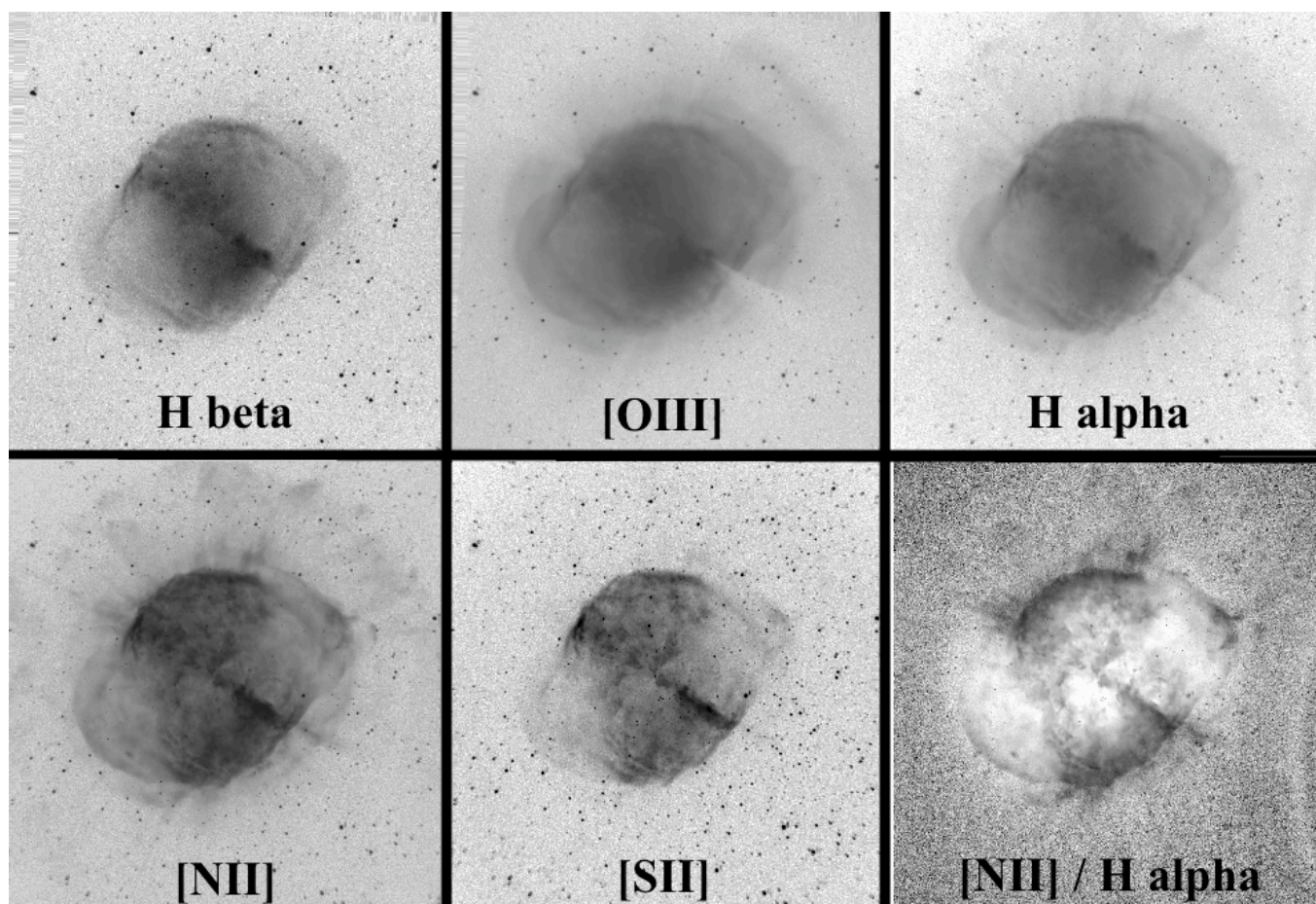


Figure 3 – Monochromatic images of the planetary nebula M27 in the brightest emission lines, obtained from SpIOMM data cubes. Each image results from the weighted average of 9 frames which sample the emission lines.

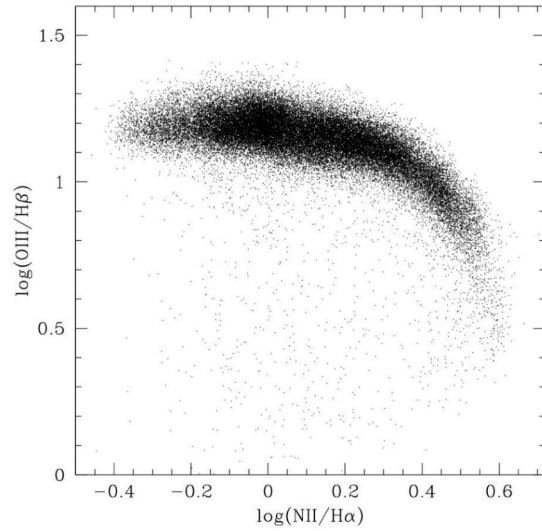


Figure 4 – BPT diagnostic diagram of M27, based on the data cube shown in Figure 3. Only the $\sim 175\,000$ spectra with the best signal-to-noise ratio are included in this diagram. The few outliers are pixels around stars which have not been filtered.

We have also targeted two supernova remnants of very different ages and evolutionary status : the Cygnus Loop and the Crab nebula. Figure 5 depicts some characteristics of a single red datacube from a small section of the Cygnus Loop illustrates the global kinematics of the nebula showing well-defined filaments approaching and receding from us.

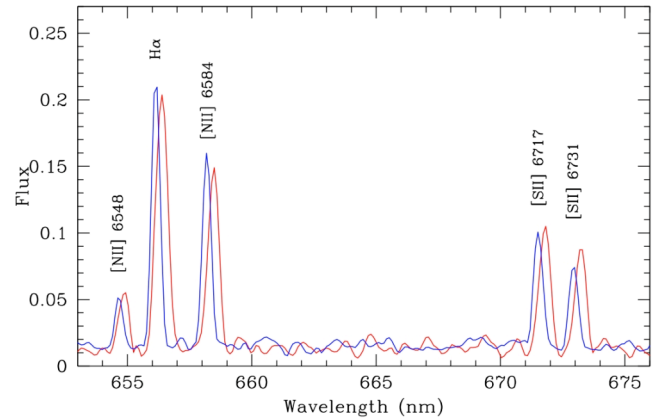
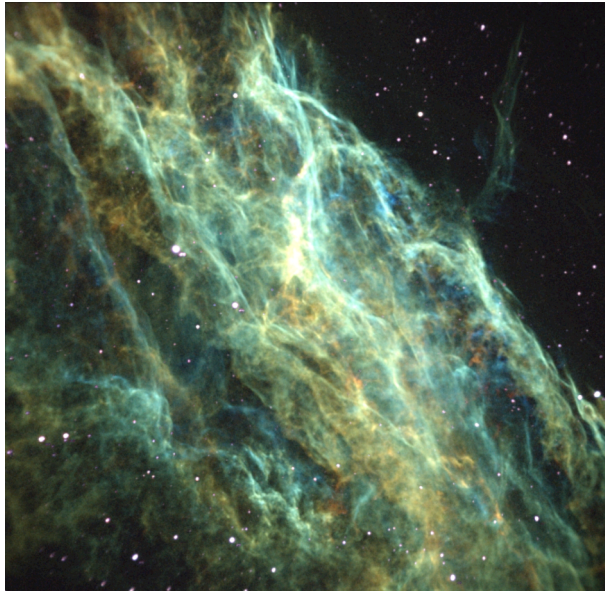


Figure 5 – **(left)** Velocity map of a small section ($12' \times 12'$) of the supernova remnant NGC 6992 (part of the Cygnus Loop), derived from all the lines available in a red data cube: [NII] 6548, H α , [NII] 6584, [SII] 6717 and [SII] 6731. Velocities range from -65 km/s (coded as blue) to +60 km/s (coded as red). **(right)** Spectra of two filaments in NGC 6992 (average of 5 pixels each) with different velocities, extracted from the same cube.

The case of the young supernova remnant M1 (the Crab nebula) is particularly interesting since it illustrates the full power of SpIOMM: because of the presence of shocks, the forbidden lines of [NII] 654.8 and 658.4, as well as the [SII] 671.7, 3.1 doublet are almost as strong as the (usually strongest) H α . Moreover, the gas is globally expanding at a velocity of 1500 km/s. Therefore, often 10, and sometimes 15 emission lines are seen in regions where approaching and receding filaments are superimposed on the line of sight (Figure 6). Using a spectral deconvolution technique, we have been able to obtain for the first time the tridimensional structure of the Crab in all 8 major emission lines. The much better image quality, spectral resolution and sensitivity of SITELLE's data will allow us to probe fainter lines to refine our view of this young supernova remnant.

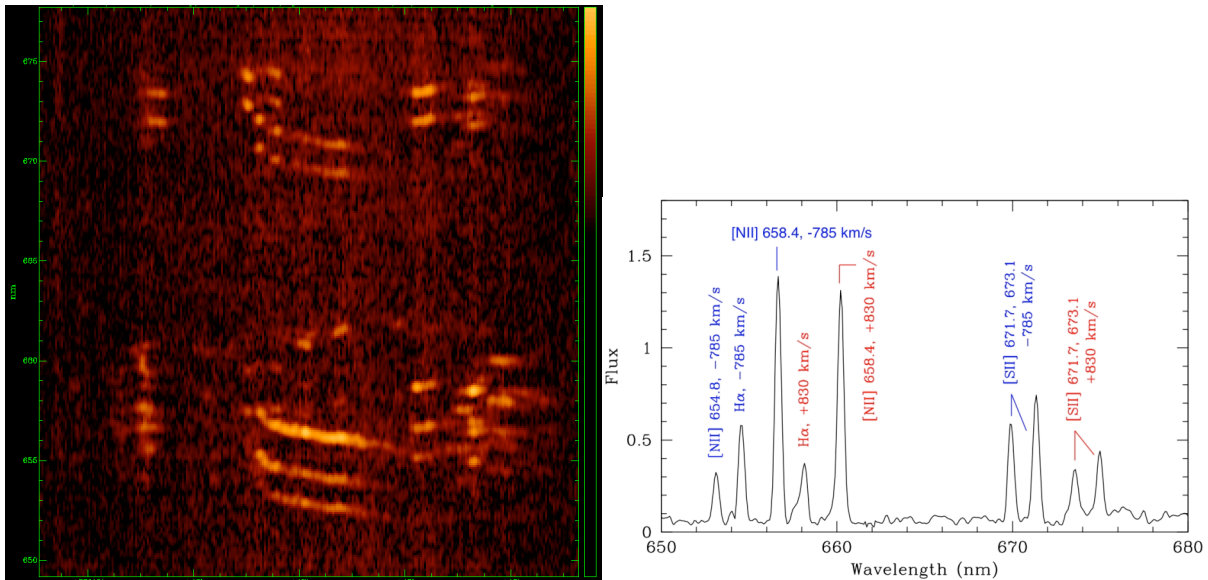


Figure 6 - (left) Slice extracted from a red data cube of the Crab nebula, simulating a long-slit spectrogram. **(right)** Spectrum of a region of the Crab where two filaments on opposite sides are superimposed on the line of sight.

We finally show two examples of extragalactic work which will represent key projects for SITELLE. The free spectral range being much wider with an imaging FTS than that of a traditional Fabry-Perot or a narrow-band filter, SpIOMM is ideal to study the outer regions of high-inclination galaxies. A filter such as the one we use with SpIOMM can sample all the [NII] 654.8 nm to [SII] 673.1 nm lines shifted by about 2500 km/s. Figure 7 shows the H α map of the spiral galaxy M106 (NGC 4258), which hosts an AGN. Similar maps can be built from the other emission lines, and a map of line ratios as well as a BPT diagram, can be produced.

We also show in Figure 8 images from a datacube of Stephan's quintet, a group of interacting galaxies at redshift $z \sim 0.02$ in front of which lie a nearby interloper, NGC 7320. The datacube clearly separates the star-forming HII regions in NGC 7320 from the more distant galaxies and allows a study of the kinematics of each galaxy. The active galactic nucleus in the Seyfert galaxy NGC 7319 is also well detected.

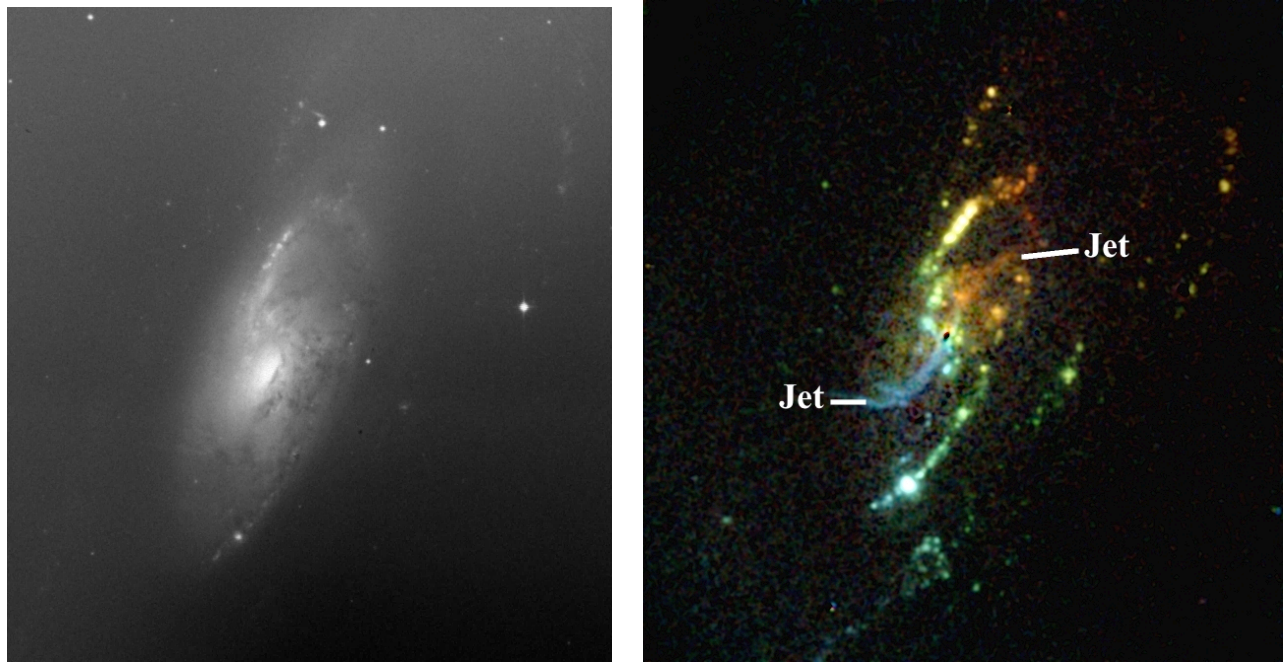


Figure 7 - Spiral galaxy NGC 4258, as seen from the digitized sky survey (left) and Spiomm (right). The right-hand image is a velocity map in H α , extracted from a red data cube. Notice the presence of the jet emanating from the central AGN. 9 x 9 arcminutes FOV.

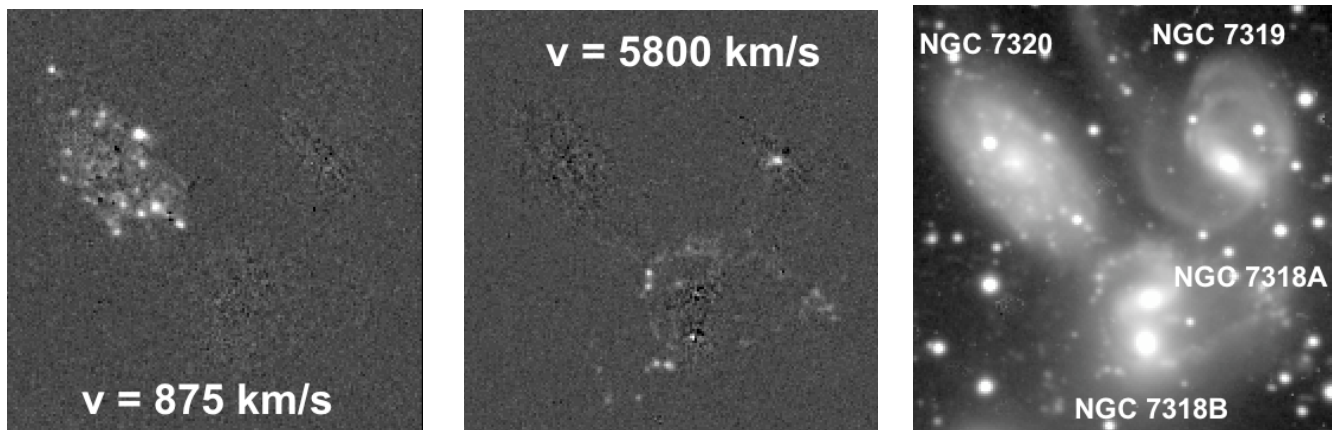


Figure 8 - (Left and center) Slices extracted from the data cube of Stephan's Quintet, showing the ionized gas in the foreground galaxy NGC 7320 and the HII regions from the highly disturbed spiral arms in NGC 7318A. Notice also, in the middle panel, the strong emission coming from the Seyfert nucleus of NGC 7319. The right-hand panel shows the deep panchromatic (650 – 680 nm) image resulting from the addition of all the interferograms.

1.3.3 – Improvements from SpIOMM to SITELLE

Our team has learned a lot from the development of SpIOMM and especially from its use on a regular basis at a telescope. All the potential improvements we have identified will be fully integrated in SITELLE (see ABB document, section 3.6.1). In particular, we expect:

- Better sensitivity in the blue.
- Use of two detectors, each with an improved quantum efficiency and reduced noise; not only will this at least double the signal, but it will also greatly improve the quality of the interferograms, which will directly be reflected in a reduced noise in the spectra, especially for continuum and absorption line studies.
- Better stability.
- Improved modulation efficiency.
- Ease of use and maintenance.

Taking into account the telescope size (a factor of 5), the image quality (a factor of two for point sources), a larger field of view (a 40% increase; see ABB document), and the technical improvements mentioned above, we expect that SITELLE will be about 20 times more sensitive than SpIOMM and will allow us to carry the ambitious projects described in the next section.

2 – Science drivers

An integral field spectrometer covering a 15 arcminute field of view is the instrument of choice for a wide variety of scientific projects. We have however focused on five topics that will dictate the technical requirements for SITELLE:

- Comets
- Galactic HII regions: turbulence, temperature and density fluctuations.
- Evolved stars and their ejecta : enrichment of the ISM, kinematics, shocks.
- Nearby galaxies : chemical abundances, population synthesis, and kinematics.
- Distant galaxies : star formation rate and kinematics.

2.1 – Solar system : Observations of comet

2.1.1 – Introduction

Comets represent the nearest class of extended and complex gaseous sources which will benefit from the use of an instrument like SITELLE. Comets can become very extended objects, particularly when approaching perihelion, with a tail which can cover several degrees on the sky, as shown by wide-field images. In regard to imagery, spectroscopic observations of comet are generally made with long slit spectrometers, giving a very limited view of the spatial distribution of the excited species. Spectral imaging is attempted with wide-field telescopes through narrow-band filters, but the exact separation of different molecular species is not possible, or with a Fabry-Perot, which cannot easily cover a large spectral range. Obviously, the complete spectroscopic coverage of a comet remains out of reach. However, resolved spectral information over a whole 15' field of the head region or in other parts of the coma would be a major achievement in cometary science.

2.1.2 – Scientific interest of wide-field spectral imagery of comets

Comets are important objects because they carry key information on the origin and evolution of the Solar System. Depending on the particular history of each observed object, new comet, long or short-period comets, they bring to analysis the building blocks of the early Solar System. Observable comets are rapidly evolving objects, spatially and temporally, as a function of heliocentric distance. The most useful information for a comet is likely to be a detailed determination of these variations in the molecular and atomic emission features, at a spectral resolution which makes possible to separate the numerous lines in a crowded spectrum for their identification and analysis, and able to provide detailed velocity information, which is the case with a 10^4 resolution, even if a somewhat higher spectral resolution would be preferable.

The 350 – 900 nm range is rich of the lines from several important radicals and molecular ions allowing to study the complex chemistry of cometary atmospheres. The parent molecules as H_2 , H_2O , CO_2 , and HCN have ground state transitions outside this region. However, the main photo-dissociated products from these molecules are observable by their strong lines in the domain, C_2 with its isotopic varieties ^{12}C , ^{12}C , ^{12}C ^{13}C and ^{13}C ^{13}C , C_3 , CN , NH_2 for the radicals, CO^+ and H_2O^+ for the molecular ions. There are also few atomic lines due to O (1D) and Na (doublet). The observation with SITELLE can provide the structure of the coma emission for these different species, their production rate, at a given distance from the Sun and as a function of heliocentric distance. For a comet at a geocentric distance of 1AU, with a spatial resolution of 1'', the projected resolution in the coma will reach a value 750 km, which is already an interesting scale for a detailed analysis of the molecule distribution sunward and antisunward

direction. A higher spatial resolution might be accessible only for bright comets, the comet tail being generally of low surface brightness.

2.1.3 – Observing program

Apparitions of bright comets are fortuitous, and can be only targets of opportunity. However, every year there are at least half a dozen comets with a visual magnitude of 10 or brighter, often periodic comets, which can be of interest since such type of observation is new. Observation should be made in priority with a set of filters centered on the main band heads of the molecular species.

2.2 – Milky Way : The internal structure of HII regions

This project is argued along three different but complementary aspects of the physics of HII regions : the gas thermodynamics, the determination of relative gas abundances and the impact of shock fronts originating from the massive stars' stellar winds on the ionisation structure. Despite significant progress made in recent years, there remains very severe uncertainties : the behaviour of small and large scale temperature inhomogeneities in ionized nebulae is almost completely unknown, abundance variations within them are still being debated and the impact of stellar winds from O stars is still unknown.

Photoionized nebulae are essential to determine the chemical composition of the ISM in galaxies, including the primordial helium abundance ^[29,30] : HII regions provide constraints on galactic chemical evolution models while planetary nebulae constrain nucleosynthetic theories and our understanding of the late stages of stellar evolution. For oxygen, the basic method is to assume an isothermal nebula and use a single value for the electronic temperature, derived directly from specific line ratios like $([\text{OIII}] 495.9 + [\text{OIII}] 500.7)/[\text{OIII}] 436.3$ or $([\text{NII}] 654.8 + [\text{NII}] 658.4)/[\text{NII}] 575.5$ ^[31]. All semi-empirical models which relied on other line ratios are calibrated using abundances obtained from the « direct » method. Stasinska ^[32], however, argued that the direct method is unreliable since it is assumed that temperature inhomogeneities are small in nebulae. This problem, identified and quantified by Peimbert ^[33], has been fully studied via photoionization models by Refs. ^[34,35,36]. Observationally, the rms temperature fluctuations on the surface of the HII regions (noted t^2) can be estimated as described by ^[37]. The effect of these fluctuations on the abundances can then be evaluated through photoionization models. Stasinska's models show that abundances can be underestimated by up to a factor of 2 if $t^2 \sim 0.04$. Although some observations have been performed, there is still a lot of controversy about actual temperature fluctuations in HII regions. For example, ^[38] found an upper limit of $t^2 \sim 0.015$ for galactic HII regions and ^[39] found $t^2 = 0.001$ in M42. For M42, very different results have been obtained by ^[37] ($t^2 \sim 0.055$) and ^[40] ($t^2 \sim 0.03$). Part of this discrepancy originates from the poor spatial sampling covered in these nebulae with long-slit spectrographs. Thus, despite its significance for abundance determination (galactic, extragalactic and cosmological) the problem of temperature fluctuations in HII regions is still not solved while its importance is well established.

Hence evidence exists for temperature variations in HII regions ^[41]; however its mapping is sorely missing while it would provide needed information to improve the dynamical modeling of these objects ^[42,43]. So far every derivation of the fluid dynamics equation either with or without shocks have been done using isothermal conditions. If this condition is not supported on large scales by observations a serious reassessment of the physical conditions would be needed. In fact, photoionized nebulae are not simple objects, homogeneous distributions of gas and monotonous velocity gradients are not recommended initial conditions. For example, kinematical studies made by Joncas and others ^[44] proved the presence of turbulence in HII regions via the behavior of the radial velocity fluctuations. One of

several statistical tools available to examine the characteristics of turbulence is the probability density function (PDF) increment^[45]. It checks for the presence of deviations from the famous Kolmogorov energy cascade where energy from the fluid flow is transferred from the large turbulent eddies to the smallest ones permitted by viscosity. These deviations are called intermittency. It describes the fact that turbulent activity can be confined at the end of the cascade to a small fraction of space leading to an uneven distribution in space and time of regions of large vorticity (shear) and DISSIPATION. This energy dumping translates into local areas of increased temperature. Observationnally these areas are detected through a non-gaussian behavior of the PDF increments. Such behavior was detected in the HII regions Sh212 and Sh269. Electronic temperatures higher than the mean value of the nebula should be measured where intermittency is present. Is this the cause of the observed temperature fluctuations ? Observers believe that the velocity fluctuations come from strong vortex tubes while theoreticians believe that they originate from the interface of 2-D shock fronts. For completion's sake, it should be mentioned that turbulence may not be the sole culprit for these temperature/abundance variations. Giammanco and Beckman^[46] propose a two phase model where ionization by low energy cosmic rays plays a fundamental role. On the other hand, [47,48] propose a two zone model where cold and hot phases coexist without the need for cosmic-rays. Three-D spectroscopy and characterization of photoionisation (see below) will enable the distinction when helped with a proper knowlege of the velocity or density field, the latter being provided by the ratio of the [SII] 671.7,3.1 line doublet.

A related thorn in our understanding of these nebulae is the discrepancy between the abundances derived from the recombination lines and the collisionally excited lines the former giving higher abundances^[49]. Garcia-Rojas and Esteban^[50] have recently reviewed and used their accumulated data to find the reason of this behavior. The only clear conclusion is that the culprit is different for HII regions than for planetary nebulae ! There also seems to be a relation with t^2 giving more credibility to the turbulence hypothesis we would like to push forward. The only high quality data available for such studies come from long slit spectrographs. SITELLE with its mapping capability will enable a much better analysis with a full scale multivariate approach.

The fact that massive stars emit strong winds has been known for a long time. This translates into well documented interactions with the interstellar medium in the case of WR stars^[51]. Even then only about 50% of known WR stars have associated nebulae. Moving down in mass, very few O type stars (like in NGC 7635) show clear interaction with their environment. HII regions with stars more massive than about O8 should show interactions with the associated ionised gas originating from the parent neutral cloud in the form of shocks or velocity behavior. Kinematical studies^[52,53] do not provide clear evidence of such interaction. Diagnostic tools exist that can pinpoint the location of shocks in ionised gas (i.e. the [SII]/H α ratio) however, once again, 2-D mapping to sufficient sensitivity is missing to determine the extent, morphology and location of such interactions since they should exist. Long slit spectroscopy applied to NGC 7635^[54] confirms the feasibility of such a study. Understanding the kinematical and dynamical impact of such winds is important in our understanding of (1) giant extragalactic HII regions (where the origin and behaviour of their large line widths is still unresolved after so many decades), (2) of the topology of the ISM (what is the filling factor of the hot gas ?), and (3) the lack of galactic fountains in our Milky Way (we find a few candidates while we should have found many hundreds^[55]). These are just a few of the questions that can be tackled.

In summary, 3-D spectroscopy, at a resolution of $R \sim 5000$, of [NII], [OIII], [SII] and Balmer lines of diffuse nebulae provides a unique way to analyze their ionisation and abundance structure and thermodynamical behaviour on large and small scales (close and away from the ionisation fronts). These nebulae contain in their mist, more often than not, massive stars that emit copious winds. However their impact on the nebula's structure lacks observational evidence. Shocks should be seen.

2.3 – Milky Way : Galactic planetary nebulae

2.3.1 – Introduction

The comprehensive study of extended and complex sources like Planetary Nebulae (PN) which contain ionized region, molecular envelope, dust ring around a central hot star, supposes the use of a 3D-technique. As for any extended gaseous region with emission lines, imaging in the strongest lines have been made, which can only give the morphology of the nebula. Spectroscopy is often conducted but on few directions with a long slit, or on a small area of at the most $\sim 10 \times 10''$, not allowing a global view for many of the much larger objects. With an instrument like SITELLE, even NGC 7293 (Helix Nebula), the closest ringed PN, could be for the first time entirely observed by spectroscopy. With BEAR several galactic young PNs were observed, showing the power of an imaging FTS to study this class of object. However, with the available field of $24''$ only the compact sources could be studied. Ideally, to separate and qualify all the components, the appropriate spatial and spectral resolution is needed. The spectral resolution makes possible to have access to the dynamics of the gas. The increasing complex morphology found from recent observations requires a new tool to make significant progress in the understanding of all the observed features. Only through a full field coverage of the nebula, combining imagery and integral spectroscopy, can make construction of a 3D view possible, giving its exact structure, mandatory to build a correct model of its formation.

2.3.2 – Scientific interest of Pne

The planetary nebulae are the ionized and photo-dissociated remnants of extensive mass loss which the central star experienced when it was a cool AGB star. They represent the short-lived transition ($\sim 10,000$ yr) of low and intermediate-mass stars (1 to $\sim 8 M_{\text{sol}}$) from AGB to white dwarf. These stars lose up to 80% of their initial mass during the AGB phase. The winds emitted by the central star compress and accelerate the neutral envelope, and as the central star evolves to higher temperatures, it emits UV radiation that photo-dissociates and gradually ionizes the expanding envelope. There is also generation by the dying star of outflows and an equatorial torus. The fast wind from the central star sweeps up the slow wind emitted in a previous epoch. The combined action of the stellar rotation, of the radiatively accelerated winds, of multiple outflows and equatorial tori during the transition from the AGB to the PN phase and the stellar radiation shapes the circumstellar envelope, which characterizes its morphology. The observed envelopes account for a wide variety of shapes, from spherically symmetric through elliptical to bipolar which have to be combined with the angle of inclination to the plane of the sky to explain the observed shape. In addition, high resolution imaging, especially with the Hubble Space Telescope, has revealed a surprising array of structures in the nebulae: multiple shells, arcs, myriads of small fragments as globules. All involve the gas component. Some show the presence of a magnetic field which is a new element to be introduced with hydrodynamical mechanisms to fully simulate the dynamical evolution of PN.

Therefore, PN provide insights in the ejection process and the mass-loss phenomenon on the AGB and beyond. From the measurement of chemical abundances, the detailed study of the structures, the kinematics and the excitation conditions of the nebula, the final goal is the reconstruction of the history of the final phases of the progenitor through an appropriate modeling, related to stellar evolution, able to

reproduce successfully all the observed features. All this ejected material contributes to the chemical enrichment of ISM with elements He, C, N and O, which can be predicted from these analyses.

2.3.3 – Observing program

The planetary nebulae observing programs should focus on the sources of largest size to make full use of the available field, which means the nearest and the oldest Galactic PNs. From about 2500 PN known in our Galaxy, there are a little more than 40 extended PN, larger than 4', observable from Mauna Kea.

These PNe should represent a large enough sample of circumstellar envelope structure from a wide range in progenitor mass to explore the final phases from the different evolutionary paths for PN formation. The visible domain probes the neutral and ionized envelope. PNe spectra are rich of emission lines. They depend on the nature of the central hot star which can be of B[e]-type as well as Wolf-Rayet (WN or WC). Among them, the most prominent are H α , H β and the [NII] λ 658.4 and [OIII] λ 500.7 lines. There are also several interesting diagnostic lines of temperature and density as [O III] λ 436.3, He I λ 587.6, 667.8, He II λ 468.6, [Fe II] λ 423.3, 442.4, [C II] λ 426.7, [S II] λ 671.6, 673.1 ...

To understand the formation of all the observed structures in the gas, their role in the fragmentation of PN nebulae, imaging spectroscopy at a spectral resolution of 10^4 is required, and at good angular resolution. The line profiles are typically double due to the approaching and receding side of the nebula, but they often show more complicated profiles with multiple components revealed by high resolution, and signature of the complex dynamical structure. Applied to a wide field, detailed studies of PN will become possible with SITELE on the CFH telescope, which will offer for the first time, unique field coverage of 15' at this spectral resolution, with good sub-seeing conditions. From deep observations, low-surface brightness shells predicted by models, creating a halo around the nebula which contains most of the ionized mass, should be detectable, which will also benefit from a wide field, knowing that this halo can be two times larger than the bright region.

2.4 – Milky Way: Nebulae around evolved, massive stars

A meaningful link between local heavy element enrichment and the global chemical evolution of galaxies can only be established by detailed studies of individual wind-blown bubbles in our own galaxy. As for the case of planetary nebulae discussed in the previous section, the winds of evolved massive stars, and their surrounding bubbles (Luminous Blue Variables and Wolf-Rayet ejecta, supernova remnants from types SNIbc or SNII) are known to be globally enriched with products of nucleosynthesis. While planetary nebulae are ejected by low-mass stars, with slow (20-30 km/s) winds, LBVs and WRs are the late evolutionary stages of the most massive stars with wind velocities of hundreds to thousands of km/s. The wind-blown bubbles surrounding these stars are often the result of complex interactions between the winds of different evolutionary phases and the surrounding interstellar medium. A complete survey of abundances, density, temperature and kinematic measurements in nebulae surrounding individual evolved stars and ionizing clusters of young HII regions, looking for inhomogeneities in the distribution of processed material (primarily nitrogen and oxygen), which has never been undertaken because it requires wide-field spectroscopic mapping, will provide firm grounds for the interpretation of global galactic abundance studies. Extended galactic supernova remnants, such as the Cygnus Loop, will also be prime targets for SITELE.

2.5 – Milky Way : Massive stars in galactic open clusters

2.5.1 – Introduction

Galactic open clusters cover large areas of the sky, with diameter from few arc-minutes to more than 1° . The youngest clusters contain emission line stars which are indicators of the presence of massive stars, sources of particular interest. Many examples of these stars have been observed to study their properties but more rarely in the context of the cluster in which they formed. A full census of the massive stars in clusters can become efficiently feasible with an instrument like SITELLE, thanks to the combination of the wide field coverage and the spectral resolution, allowing to detect all the massive stars in a field through their emission line, and to resolve their line profiles which depend on the mass of the star, its internal structure and its evolutionary phase.

The massive stars are grouped in classes defined by typical lines in the visible range. The proportion of each class in a cluster gives precious information on its formation conditions. The main classes of massive stars are:

- *classical Be stars*, main sequence B stars near critical rotation which can be identified through their H α and H β emission lines,
- *Of stars*, dwarf to supergiant O-type stars with emission in the NIII 4634-40-42, NIV 4058, NeII 4686 and SiIV 4088, 4116 lines,
- *Wolf-Rayet stars*, with two wide sub-types WC and WN, which represent final phases of stars with strong winds and masses at ZAMS higher than $30M_\odot$, effective temperatures $\log T_{\text{eff}} > 4.0$, and the mass fraction of hydrogen at their surface roughly $X < 0.4$. They result from the following evolutionary-phase changes:

O star \rightarrow Of/WN \rightarrow LBV (Luminous Blue Variable) \rightarrow WN \rightarrow WC

- The classification criteria of WN stars are based on the emission lines of NIV 348.0, NIII 464.0, CIV 580.8, HeII 468.6, 541.1 and HeI 587.5 lines. The classification of WC is based on the strong emissions in the HeI 587.5, HeII 468.6, CIII 465.0, 569.6, CIV 580.8 lines.
- *Stars with the B[e] phenomenon*, O, B, A-type stars with strong emission in the visible range of the Balmer lines, of the low-ionized species like [FeII] and [OI], making them easily detectable.

2.5.2 – Scientific interest of massive stars in stellar clusters

Since stellar clusters and associations are characterized by a simultaneous formation, they are privileged laboratories to study for each of them i) **star formation rate** (SFR) and **initial mass function** (IMF), ii) **chemical evolution**. Due to the high luminosity of the emission line stars, clusters up to large distance in our Galaxy can be observed, providing different initial chemical compositions. In addition, from the resolved line profiles can be studied iii) the **rotational velocity distribution** in a cluster.

i) As massive stars have strong winds, they virtually evaporate producing a trail of stellar populations, O, Of, WR, supergiant ..., characterized each by different lasting time scales, and depending on their initial mass. The counting of these stellar populations, through direct detection by spectral imaging of clusters, enables to characterize the SFR and to estimate the slope of the IMF as a function of the chemical composition. Generally, the higher metallicity the higher is the mass-loss rate and the larger the number of WR stars. However, smaller metallicities produce massive stars with smaller radii, which imply that those stars with same angular momentum content than similar objects in regions with high-Z, will rotate faster. In turn, fast rotation increases the internal mixing, which finally reduces the mass at which a star can enter the WR phase. Accordingly, fast rotation increases the duration of the WR phase which leads to larger WR/O and WN/WC population ratios. Extended to an entire cluster all these ratios are important statistical information that enables to predict the evolution of clusters.

ii) Massive stars play a leading role in the chemical evolution of galaxies, for they are fast nuclear reactors that can contribute efficiently to the nucleosynthesis of heavy elements. Due to their fast evolutionary pacing, their evolutionary time scales from the ZAMS are used to determine the age of clusters to which can be compared other time dependent phenomena assumed in the theories of stellar evolution. They are the main source of UV and ionizing radiation. Thus, for distant galaxies, the integrated luminosity provided by the emission lines enables to estimate the total number of hot stars of different classes. The integrated intensities in the $H\alpha$ and $H\beta$ lines are related to the number of Lyman ionizing continuum photons, which in turn give the number of O-type stars in the studied environment. The ratio between the $H\beta$ and $HeII\ 468.6/CIII-IV\ 465.0$ emission line intensities are proportional to the WR/O and WN/WC stellar number ratios, respectively. Thus, refined calibrations of these quantities can be obtained by the complete study of nearby clusters in these spectral lines, then to be used to analyze distant galaxies.

iii) The spectral resolution of 5000 to 10,000 of SITELLE is well adapted to derive the rotational velocity of the emission line stars. From the spectral imaging of a cluster at this resolution can be inferred the rotational velocity distribution to correlate it with the counting of hot-star populations. These studies are cornerstones to test the mixing and angular momentum redistribution processes assumed and currently parameterized using only first principles in the stellar evolution computation of rotating stars. As a by-product of spectral imaging of clusters at specific wavelengths is the identification of interacting regions between stellar winds of hot stars with their surrounding interstellar medium (ISM), through the emission in the H and He lines of the circumstellar bubbles or rings that these interactions create.

2.5.3 - Observing programs

The data on the galactic open clusters (coordinates, apparent diameter, distance, age, metallicity when available) are gathered in the WEBDA database, originally developed by J.C. Mermilliod. Tables have been extracted of clusters hosting classical Be stars and those containing WR stars and Herbig Be stars. In each category about 75 clusters are observable from Hawaii. Their distances go from 150 pc for the closest one, the Pleiades, to more than 6000 pc and the age from 6 to 300 Myr, giving a large choice of targets for different conditions of metallicity and evolution. Some emission line stars are already detected in these clusters but for most of them a full census has never been possible, which can be undertaken for the first time with SITELLE. Emission lines stars are easier to detect than stars with absorption lines since they give a high S/N ratio at their emission peak, providing filters well adapted to cover several emission lines and a minimum of continuum level to minimize the photon noise.

Other methods of detection are made by imaging the cluster with narrow-band filters centred on typical emission lines. Providing a correct subtraction of the continuum level which is not an easy task, this method gives only candidates without information on their type. Subsequent observations are required with a multi-object spectrometer (MOS), depending on the field size and the number of candidates. With SITELLE, from a single observation, all the emission line stars in a 15' field, with the possible identification of several lines, can be detected in a cluster and characterized. A good spatial resolution makes possible to identify the stars in the crowded parts of the cluster. In addition, the interstellar gas can be observed simultaneously, which is not feasible with a MOS.

2.6 – Nearby galaxies

2.6.1 - Introduction

Metals in the Universe are directly related to the appearance of life. Processing from evolving and dying stars inject freshly processed metals in the Interstellar Medium (ISM) which is in turn used to form a

news generation of stars that will inject more metals. This process eventually produces enough metals to start forming objects that are entirely made of metals like planets, comets and meteorites. Studying the abundance of metals in the Universe is inherently difficult. Before knowing how things happen at high redshift, a good understanding of the local distribution of metals is needed.

Powerful constraints on models of galactic chemical evolution, on the star formation histories of galaxies and on the dynamical processes that transform them can be derived from accurate and homogeneous determinations of (a) chemical abundances in individual gaseous nebulae; (b) the distribution of their stellar populations in terms of age and metallicity, and (c) the gaseous and stellar kinematics. So far, systematic studies between chemical properties (central abundance or radial abundance gradient), and other parameters have been conducted for a small sample of spirals. The effects of the morphological type, the presence of bars, and environment have all been studied to some extent. However, although informative, these studies suffer from several severe limitations :

- Abundances derived from a few individual HII regions in each galaxy : long-slit, MOS and IFU spectroscopy is limited to a tiny fraction of the total surface of their targets ;
- Lack of uniformity in the calibration methods used to determine the abundances ;
- Limited sample of galaxies across the Hubble sequence ;
- Large uncertainties arising from diverse spectrophotometric techniques (narrow slits, narrow-band imaging).

Moreover, most studies so far, performed with slit spectrographs, have concentrated on global properties of stellar ejecta or abundance gradients in galaxies, thereby neglecting possible small-scale variations caused by multi-phase stellar wind (individual stars) or localized enrichment by starburst clusters in peculiar evolutionary stages. SITELE will be an ideal instrument to conduct a systematic study of abundances and thus easily detect evidence for small-scale enrichments and establish conditions under which they take place. The possibility to study the multiple emission line ratios and kinematics for hundreds of HII regions simultaneously in each individual galaxy would completely remove some of the limitations mentioned above. With the availability of several lines *simultaneously* (e.g. [OII] 372.7, 732.0, 733.0 ; [OIII] 436.3, 495.9, 500.7 ; [NII] 575.5, 654.8, 658.4 ; Balmer series) as opposed to FP or interference filter data which cover a single line, diverse abundance calibrations could then be applied and evaluated. Absorption lines due to the presence of underlying stars will be obtained simultaneously, thereby providing crucial information about older stellar populations, such as age and metallicity. With its high efficiency and large field of view, SITELE will be the ideal instrument to carry a large program on the chemical abundances, kinematics and stellar populations of a significant sample of nearby galaxies across the Hubble sequence. Since most of the conclusions drawn so far on the chemical composition of galaxies are based on restricted and inhomogeneous data, such a dataset would revolutionize the study of galaxy chemical evolution.

Abundance studies in H II regions of local galaxies are thus numerous but remain essentially affected by incompleteness of the samples, abundance determination techniques, spectroscopic and photometric systematic issues. Abundances are usually calculated using hydrogen and oxygen optical narrow emission lines. Oxygen narrow line emission is the main process for cooling an H II region. This process produces strong optical emission lines that are easy to observe. On the other hand, abundance determinations can also be done on elements like sulfur, nitrogen and neon. Mainly two methods have been developed over the years to determine extragalactic abundances. The direct method uses the measurement of nebular lines in concert with determinations of electronic density and temperature, atomic parameters and the model of an H II region to determine the abundance of a certain atom. This method has the advantage of giving reliable results but it relies on the measurement of weak lines which severely limits its sensitivity. In order to circumvent this problem, an empirical method is often used. This approach uses the direct method on bright H II regions to calibrate the relationship between abundances of a certain element and the flux in the brightest lines emitted by this element. In the case of

oxygen, three very bright lines are emitted by the O⁺ and the O⁺⁺ ions at 372.7, 495.9 and 500.7 nm. These lines have been widely used to determine oxygen abundances in local galaxies. Even though the empirical method makes it easier to measure abundances, it is affected by several systematics and relies on models for higher values of oxygen abundance. Recently, abundances measured in H II regions of M33 using mid-infrared neon emission lines and new measurements and recalibration of the optical oxygen lines lead to a revision of the abundances in M33. This shows that abundance determinations in local galaxy need to be systematically revisited. Revising this local calibration has an important impact on the interpretation of the observations at high redshift.

2.6.2 - Abundances in Local Galaxies

The direct method - When an ion of a certain element transits from an excited energy state to a lower, more stable state of excitation, mono-energetic photons are emitted and these produce an emission line in the spectrum of the studied object. Several of these transitions from the same element at different stages of ionization will produce emission lines and the analysis of the measured flux in these lines can then be used to calculate elemental abundance.

When measuring abundances in galaxies, the electronic temperature (T_e) and density (N_e) are the quantities of interest. They are measured by observing the strength of the narrow lines emitted by ions excited by collisions with thermal electrons. The population of ions in different excitation states can then be calculated and used to determine the electronic temperature and density. If two excited states of the same ion have a large difference in excitation energy, the ratio between the population of the two ionic species can be used to measure the electronic temperature. On the other hand, if two excited states of the same ion have a small difference in excitation energy, then the line ratios can be used to measure the electronic density^[56].

For the electronic temperature, measurements of the narrow lines of the O⁺⁺ ion are often used. If an H II region has a higher amount of oxygen, cooling will be more efficient and the equilibrium temperature will be lower thus lowering the flux in the oxygen lines. The triplet [O III] $\lambda\lambda 436.3, 495.9, 500.7$ nm lines are good tracers of electronic oxygen temperature. However, the usage of these lines is limited to object with low abundances. As the amount of oxygen available to cool an H II region rises, the temperature of equilibrium of the electronic gas lowers, thus lowering the oxygen line emission. Since the transition probabilities between the energy levels responsible for the emission of the [O III] $\lambda 436.3$ nm line is much lower than the transition probabilities of the energy levels responsible for the emission of the [O III] $\lambda\lambda 495.9, 500.7$ lines, the [O III] $\lambda 436.3$ line becomes too faint rather quickly as the oxygen abundance becomes higher. Once the electronic temperature and density are known, the abundance of the corresponding element can be calculated using atomic parameters and a model of the H II region.

In the simplest case, the H II region is modeled using a single layer of constant electronic temperature and density. More sophisticated modeling can also be done using multiple layers of T_e and N_e for the H II region^[57]. Together with atomic parameters and line strength, the abundance of the ion that emits the line can be determined. Assuming a correction factor for ions and atoms whose lines aren't measured, a total abundance of the element can then be derived. Three-dimensional modeling can also be performed. In this cases, the radial and angular distribution of T_e and N_e are modeled instead of using a uniform layers^[58].

Abundance determinations using this method are heavily biased toward low oxygen abundances. It is however considered a reliable way of determining abundances since it is based on sound physical principles. This method can also be applied to other elements, given that the relevant lines are measured.

Empirical Calibrations - Empirical calibrations are necessary to derive oxygen abundances in objects where the [O III] $\lambda 436.3$ line is too faint to be detected. The purpose of this calibration is twofold. First, abundances need to be measured at higher metal content and second, empirical calibrations enable the use of brighter lines making it easier to do the actual measurement. Using the direct method described

above, Edmunds & Pagel^[59] (EP84) constructed one of the most widely used abundance calibrators. It consisted in measuring the electronic temperature in low metallicity galaxies using the $([\text{O III}] \lambda 495.9 + [\text{O III}] \lambda 500.7) / [\text{O III}] \lambda 436.3$ line ratio and derive the abundance of oxygen using the direct method. The actual calibrators are constructed using the derived abundances and the measured $([\text{O III}] \lambda 495.9 + [\text{O III}] \lambda 500.7)/\text{H}\beta$, $([\text{O III}] + [\text{N II}]) / \text{H}\beta$ and $([\text{O III}] + [\text{O II}]) / \text{H}\beta$ (R23) line ratios. For the high abundance end of the relationship, photoionization models were used to infer the flux of the bright lines versus the number of oxygen atoms and ions an H ii region. These abundance calibration were widely used to derive the distribution of the abundance of oxygen in local galaxies. In general, R23 is greatly preferred over the other calibrators since it uses two ions of the same atom and shows little spread when calibrated against the oxygen abundance. The $([\text{O III}] \lambda 495.9 + [\text{O III}] \lambda 500.7)/\text{H}\beta$ ratio is often thought to be the least reliable and is usually not seen as a reliable indicator of oxygen abundance. However, comparison of the $([\text{O III}] \lambda 495.9 + [\text{O III}] \lambda 500.7) / \text{H}\beta$ ratio with R23 shows that it gives may give surprisingly accurate results. This indicator is used often since the $[\text{O II}]$ line is difficult to observe due to the usually poor efficiency of telescopes in this wavelength range. However, a good system response at that wavelength is one of the key requirements of SITELLE, which will make a significant contribution to his field by obtaining maps of the R23 ratio in galaxies. Using empirical abundance calibrators makes the measurements of abundance sensitive to systematic uncertainties like the assumed electronic temperature, the assumed ionization parameter, the model used for extinction correction and the photoionization model used for the extrapolation at higher oxygen abundances.

Inaccuracies of the empirical calibrations - Recently, problems have been uncovered regarding the distribution of metals in M33. Discrepancies in the measurement of the abundance gradient using mid-infrared observations lead Willner & Nelson-Patel^[60] to suggest that the neon gradient in M33 was shallower then the one measured using optical oxygen lines and the method of EP84^[61]. They suggested that the discrepancy they observed could be due to supernovae ejecta of progenitor masses of 15 to 25 M_{\odot} or that the oxygen abundance determinations were wrong and that these need to be revisited. Later on, optical measurements of abundances in M33 were done by Crockett et al.^[62] and Magrini et al.^[63] using the direct method where the $\lambda 436.3$ nm line was detected and a different empirical calibration when this line was absent. Also, [62] recalibrated the data of [61] using their own method while Magrini et al.^[63] used the calibration of Izotov et al.^[65] to recalibrate Vilchez's data. Both studies found a shallower gradient in the gas on the order of $0.04 \text{ dex kpc}^{-1}$, in agreement with the measurements of Willner & Nelson-Patel.

2.6.3 Why SITELLE is better

Abundance calculations using either of the techniques described above can be done using either narrow band images or optical spectroscopy. These two methods are mutually exclusive. Narrow band imaging techniques allow to derive abundances by observing the narrow line emission directly. The central wavelength and bandpass of the filter are tuned to match a certain emission line. However, the sample of galaxies that can be observed is strongly dependent on the characteristics of the filter used and the redshift of the galaxies. In general, more custom made filters are needed to include more galaxies in the sample. Tunable filters can also be used to gather narrow band information on galaxies^[66] but these observe only one bandwidth at a time and several exposures are need in order to collect data on several lines and the adjacent continuum.

On the other hand, spectroscopic observations give a complete coverage in wavelength (thus redshift) but this is done at the expense of the field of view. If a decent field of view is needed, several pointings are required which is very time consuming. Multi-slit spectroscopy or fiber spectroscopy offers a nice compromise between wide field imaging and single slit spectroscopy. However, the filling factor of the observed field is quite small, even with several thousand fibers or apertures. With SITELLE, each pixel

on the field of view is an aperture so in terms of today's detector sizes and Mauna Kea's weather conditions, SITELLE puts millions of apertures on the sky.

SITELLE is a unique instrument that is perfect to carry abundance studies. It allows simultaneous observation of a wide field of view over a wide range of wavelength at a covering factor of 100%. This allows simultaneous observation of several optical lines in local galaxies. SITELLE also allows to perform these observations at high redshift. Observation of lines other than oxygen are desperately needed but are really hard to obtain. Current techniques prefer to concentrate on oxygen measurements since the lines are very bright.

2.6.4 - Scientific Return

With its wide field of view and large spectral coverage, SITELLE will be the ideal instrument to perform measurement of narrow emission lines in external galaxies. These measurements will help advance the field of abundance studies to reliable measurements of metal content in local and high redshift galaxies.

Measuring abundance gradients - SITELLE could perform the same type of studies on local galaxies than those performed by [62, 63, 65] on a much larger sample of galaxies and of HII regions within these galaxies. Magrini et al.^[63] used a wide field multi object spectrograph and observed 72 emission line objects within M33. SITELLE has the potential to detect several hundreds of these objects making the likelihood of detecting the [O III] λ 436.3 higher and thus the derivation and calibration of the other lines more reliable because of a bigger sample size. Also, SITELLE can simultaneously observe emission lines from other elements. Observation of hydrogen lines is crucial for abundance studies. Hydrogen flux at H β is used as a reference for abundance calculations while any other combination of two or more Balmer lines can be used as an indicator of extinction. A good estimate of this quantity is crucial to have precise abundance calculations. It is often useful to use more than two Balmer lines to estimate extinction. Also, observation of emission lines other than oxygen can be used to derive abundances build and empirical calibrations for other elements. A good example is the [N II] ion which has an energy-level structure similar to that of the [O III] ion with emission lines at $\lambda\lambda$ 654.8, 658.3 and 575.5 nm. Observation and calibration of lines other than oxygen are needed but are really hard to obtain. Current techniques prefer to concentrate on oxygen measurements since the lines are very bright. It is not well known how the observation of the abundance of other elements varies with respect to the theoretical prediction. For example, the measurement of Neon abundances in M33 done by Willner & Nelson-Patel^[60] was expected to vary with oxygen since both elements are the product of primordial nucleosynthesis. A discrepancy was indicative of a problem somewhere. It turns out that in this particular case, nucleosynthesis predictions seems to be correct. It would be interesting to see if the trend seen in M33 can be reproduced in other galaxies where physical conditions might be quite different. Also, understanding galaxy formation and evolution can be greatly improved with a better understanding of galactic chemical evolution. Several factors are responsible for this process. The local initial composition of metals, the star formation history along with stellar yields, the gas infall and outflow are all physical parameters that are probed by studying the abundance gradients in galaxies. Oxygen abundance gradients are also used to find correlations with macroscopic properties of galaxies^[67, 68].

Cosmological impact - In the Cosmological context, we need to have an accurate picture of the content and the evolution of metals and in local galaxies to estimate what is happening at high redshift. The calibrations of bright oxygen lines with oxygen abundance described in the previous sections will be most helpful for high redshift studies since detecting the [O III] λ 436.3 gets harder for more distant galaxies. On the other hand, bright oxygen lines like [O III] λ 495.9, [O III] λ 500.7 and [O III] λ 372.7 become extremely useful for abundance determination as redshift increases. It is not clear how metals

are distributed as a function of redshift. There is now substantial evidence that the amount of metals is as high as $1/3 Z_{\odot}$ as early as $z = 1.3$ ^[69]. Systematic studies using bright oxygen lines along with an accurate calibration will help approach this problem from a different point of view. SITELE can observe the [O III] triplet lines up to a redshift of ~ 0.9 . The abundance of metals as a function of redshift can thus be derived in different environments and compared with the results found by Tozzi et al.^[69] in galaxy clusters.

While the emphasis has been put here on the emission lines from regions ionized by young, massive stars, SITELE will also be able to characterize the old stellar population with the detection of absorption lines such as FeII (527.0 and 533.5 nm), the H β absorption or the Ca triplet (849.8 nm, 854.2 nm and 866.2 nm). These indices are then used to constrain the age of the population and the stellar metallicity^[70].

2.7 – Distant galaxies & cosmology

Because SITELE can be used without predefined filter in the whole visible waveband, or with relatively large-band filters, it will be extremely useful to study the intermediate-to-high- z Universe in a relatively unbiased way. It will, for example, allow detection of Ly- α emission in objects from $z = 2$ to 6.5. The power of SITELE in this type of study is that it will sample the redshift space uniformly on a wide field, allowing spectroscopic redshift determination and line profile analysis on several galaxies in a single observation. In the same vein, chemical abundance studies at intermediate redshift, or the study of the kinematics in the intergalactic gas in clusters, could also be performed.

2.7.1 – Observing the High-Redshift Universe

Most of our knowledge of the high-redshift universe has been acquired through multi-slit spectroscopic observations. The fundamental bias of this technique is the need to pre-select targets from a set of broadband images that may miss objects with strong emission lines but very weak continuum. In order to overcome this bias, some studies have used narrow-band filters with fixed or tunable bandpasses. The large field of view of SITELE is ideal to conduct surveys over cosmological volumes much larger than previously observed and can thus overcome the effects of cosmic variance. We focus here on two exciting applications of SITELE observations namely the cosmic star formation density as a function of redshift and the population of Lyman-alpha emitters at very high redshift that many consider to be linked to the first galaxies and the epoch of reionization.

2.7.2 – Star-Formation Density Survey

The cosmic star formation density has been extensively studied over the past decade starting with the work of Lilly et al.^[71] and Madau et al.^[72]. A recent version of the Lilly-Madau plot is shown in Figure 10. It shows a significant rise from $z = 0$ to 1, a peak between $1 < z < 2$ and a flattening or decline depending on the adopted dust obscuration correction. Juneau et al.^[73] have further shown that the cosmic star formation density was dependent on galaxy stellar mass with more massive galaxies producing their stars earlier than low mass ones. This was taken as support for “downsizing”, a process in which galaxy formation proceeds from larger to smaller mass scales in *apparent* contradiction with the canonical cold dark matter hierarchical mass assembly model.

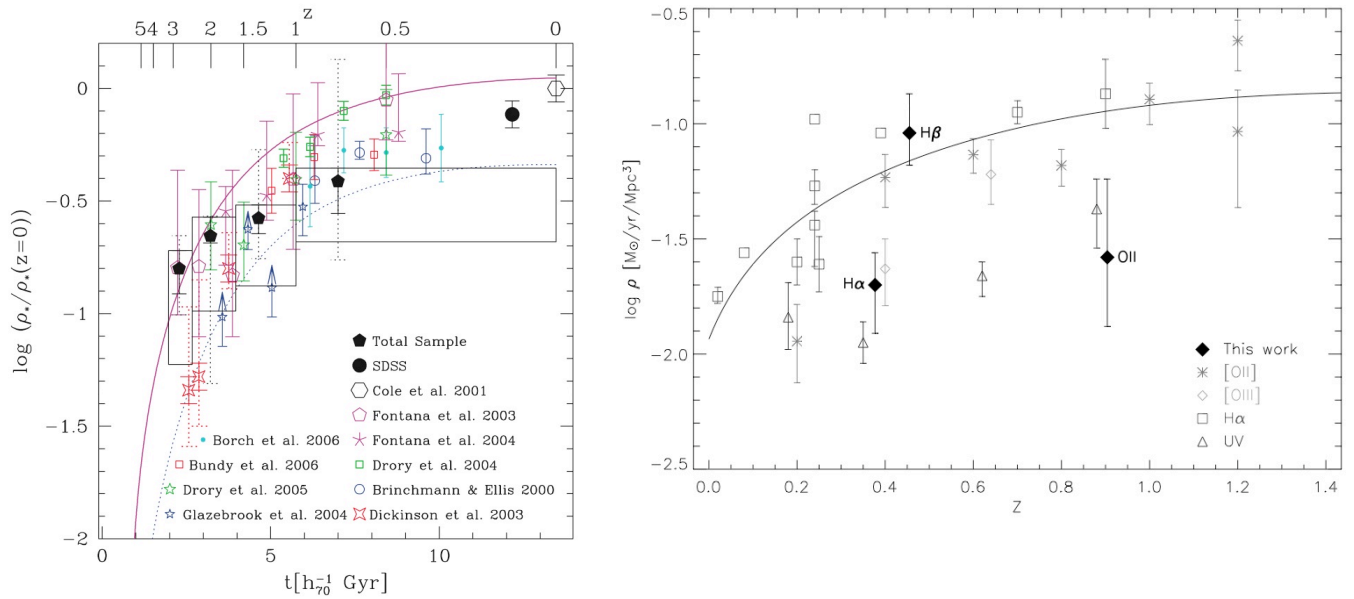


Figure 9 - Cosmic star formation density as a function of z . *Left* : Measured from broadband+multi-slit observations ^[74]. *Right* : Measured from narrow-band observations ^[75].

There are many unique advantages to mapping star formation as a contiguous datacube in wavelength/redshift space. A line can be identified via a peak in flux without reference to any broadband image. Higher resolutions ($\Delta\lambda \sim 10\text{\AA}$) can be achieved, and this provides a better match to the typical line widths with corresponding gains in S/N. A scan through the datacube also allows to precise removal of the background from the line profile, and “three-dimensional” photometry can be then performed to measure the *total* line flux without the need for slit aperture corrections. The deepest tunable bandpass survey to date is from Glazebrook et al. ^[75]. They reached a limiting flux of $1.7\text{--}2.4 \times 10^{-17}$ ergs $\text{s}^{-1} \text{cm}^{-2}$ albeit over a relatively small area of 20 arcmin^2 . As shown in Figure 9, their measured star formation densities are somewhat discrepant in comparison to previous broadband-based works. These discrepancies can be entirely attributed to the effect of large-scale structures. Cosmic variance has been and remains a fundamental limitation on this type of measurement, and this is where the large field of view of SITELLE will play a critical role.

An ambitious program that could be tackled with SITELLE would cover $6500 \text{ square arcmin}$ down to a 5.5σ flux limit of 4.3×10^{-17} ergs $\text{s}^{-1} \text{cm}^{-2}$ (line luminosity of 2.3×10^{41} ergs s^{-1} at $z = 1$) over the redshift range $0.6 < z < 1.0$. This area would require 30 pointings with an exposure time of four hours per pointing for a total of 20 nights. The resulting cosmological volume of this survey would be $4.5 \times 10^6 \text{ Mpc}^3$. This volume is over 1000 times larger than the Glazebrook et al. survey volume and should produce measurement of the cosmic star formation density good to ~ 0.05 dex in addition to probing its dependence on galaxy stellar mass in greater details.

2.7.3 – Lyman-Alpha Emitter Survey

The identification of galaxies at the earliest cosmic epochs is a key goal in probing galaxy formation and the epoch of the reionization of the Universe. We still do not know whether the latter is linked to the first galaxies or another population of objects such as population III stars. Recent studies of Lyman-Alpha Emitters (LAEs ^[76–78]), which are thought to be young galaxies, have placed some constraints on their nature on their luminosity functions and star formation rates (Figure 10). LAE ages and masses range

from 1 – 1000 Myr and 10^{6-10} solar masses respectively. However, there is growing evidence that the LAE population may in fact be composed of multiple subpopulations. In addition to young, low-mass galaxies, LAEs may also be dusty starbursts and even evolved galaxies!

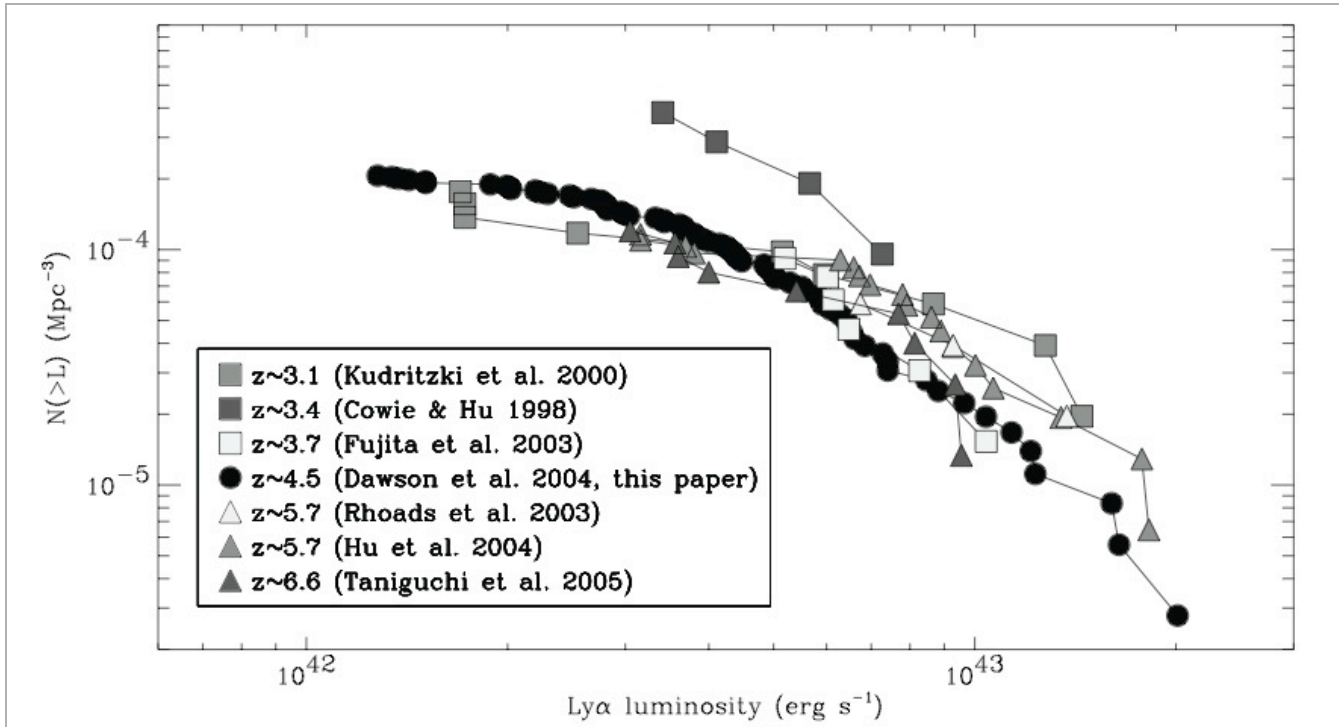


Figure 10 - The cumulative luminosity function of Lyman-Alpha emitters from previous works ^[77]

LAE studies are transitioning from single detections to statistically significant samples as the efficiency of various searches dramatically improves. Owing to its field of view and its sensitivity, SITELE is very well positioned to make an important contribution to the task of disentangling the different LAE populations. The numbers of LAEs in each population must first be established. A significant fraction of dusty starbursts and evolved galaxies would place interesting challenges on duty cycles of metal production and stellar mass assembly in the early Universe. If most LAEs are in fact found in these two subpopulations rather than being young, primitive galaxies, then constraints on the elusive epoch of reionization and the role of galaxies in this process would have to be re-thought.

In order to assemble a sample of 1000 LAEs above a luminosity of 6.5×10^{42} ergs s⁻¹ at redshifts of $4 < z < 5$ (look-back time of 13.666 Gyr) – more than a tenfold increase in sample size, one would have to observe a volume of 2×10^7 Mpc³. This corresponds to ~30 SITELE pointings. The current estimate for the SITELE overall throughput requires an exposure time of four hours per pointing (5.5σ flux limit of 4.3×10^{-17} ergs s⁻¹ cm⁻²) for a total of 20 nights. Such a survey would be sensitive to LAEs with a star-formation rate down to 5 solar masses yr⁻¹ ^[79]. It is likely that this SITELE LAE observing program will overlap with the cosmic star formation survey proposed in Section 1, and that the two programs may in practice be combined into a single survey (the observed wavelength range of the [OII] 3727 line at $0.6 < z < 1.0$ corresponds to the Lyman-alpha line at $4 < z < 5$).

3 – Instrument requirements

The science requirements mentioned in the previous section define the technical requirements of SITELLE :

- Wavelength range - In the local universe, the [OII] 372.7 nm line defines the short wavelength requirement. It is used to measure the oxygen abundance in ionized nebulae. The long wavelength limit is defined by the Ca triplet at 849.8 nm, 854.2 nm and 866.2 nm, which characterize the old stellar population in galaxies. In the case of the high redshift objects, the wavelength range accessible with the instrument defines the redshift range in which the Ly α line can be detected. The above-mentioned limits (370 – 870 nm to include some margin) set this range to $2.0 < z < 6.15$. A small gain will be obtained by enlarging the wavelength range to 350 nm – 950 nm ($1.9 < z < 6.8$).
- Spectral resolution – The cosmology projects do not require a high spectral resolution. The minimum resolution required for the analysis of the ionized nebula in the Milky way and other galaxies, is set by the necessity to separate the [SII] 671.7 / 673.1 nm doublet, the H α 656.3 nm from its [NII] 654.8 nm and 658.4 nm neighbors, and H γ 434.1 nm from [OIII] 436.3 nm. This implies a minimum value of $R = \lambda/\Delta\lambda = 1000$. However, kinematics of HII regions and the studies of stars in clusters impose a more stringent requirement of $R = 10^4$.
- Field of view – The maximum field of view of dispersive integral field spectrometers reaches one arcminute (SAURON, and the future MUSE). A FOV of 5 arcmin would represent a significant improvement. Most projects on stellar ejecta and nearby galaxies would also be feasible with a 5 arcmin FOV. However, for the study of extended HII regions in the Milky Way and the high-redshift galaxies, reasonable amounts of observing time require a FOV > 10 arcminutes, which set the constraints for SITELLE.
- Spatial resolution – Most of the projects presented here put the emphasis on the wide field observation of extended, diffuse objects and do not on the spatial resolution. However, observations of individual stars in clusters and distant galaxies require that the pixel size be no larger than the typical seeing, 0.6 arcsec. The panchromatic image quality (350 – 950 nm) should be no worse than one arcsec.
- Sensitivity – Two of the most stringent constraints in terms of sensitivity, from the science case, are the ability of SITELLE to detect the faint [OIII] 436.3 line, which is not always detected in HII regions, and its capacity to detect Lyman alpha emitters down to a flux of 4.3×10^{-17} ergs s $^{-1}$ cm $^{-2}$ (5 sigma detection) in a reasonable integration time.
- High observing efficiency – The readout time, combined with the displacement time of the interferometer should be a small fraction of the total on-target exposure time.
- Filter wheel – To increase the spectral resolution and reduce the photon noise from the sky or the intrinsic continuum of the objects, most observations will be performed with filters, either wide-band (cosmology, low resolution observations; $\Delta\lambda \sim 100 - 200$ nm) or medium-band (nebular analysis; $\Delta\lambda \sim 10 - 50$ nm). A standard set of filters, to be defined later, will be provided, and each user could choose the appropriate filter tailored to its needs.

4 – Instrument concept

(ABB document – section 3)

4.1 – Introduction

The design of the instrument was performed by engineers and scientists (led by Grandmont, system engineer) at ABB Bomem Inc., a Québec city-based world leader in the development of Fourier transform spectrometers, with numerous interactions (via teleconfs or personal meetings) with the SITELLE science team and the CFHT staff. Grandmont's Ph. D. thesis at Université Laval, under the supervision of Drissen, entitled *Développement d'un spectromètre imageur à transformée de Fourier pour l'astronomie*, describes the design, construction and use of SpIOMM. The initial optical design was performed by S. Thibault at Université Laval. The Instrument concept, a preliminary but relatively detailed design, the development requirements and a first cost estimate are described in a separate document appended at the end of this one. We add below some comments on the detectors to be used for SITELLE.

4.2 – Detectors

As in all astronomical instruments, the detector is an essential component. In the case of an imaging FTS, two characteristics are especially important. As the datacube is built by acquiring multiple images of the target at different optical path differences, the readout time must be a negligible fraction of the on-target exposure time, and the readout noise must be small compared with the photon noise (from the target or the sky). Typical exposure times per step range from 10 seconds to one minute; the displacement of the interferometer's moving mirror takes one second. Therefore, the readout time dominates the « dead time » between exposures; it must be kept to a minimum, ideally smaller than 2 - 3 seconds is required.

The total field of view and sampling specified in the requirements implies a 2k x 2k (13-15 μm pixels) detector for each of the two output ports. Moreover, the requirement for high sensitivity in the near UV ([OII] 372.7 nm line) implies a high quantum efficiency below 400 nm; this is now a regular feature of UV-enhanced, back-illuminated CCDs. Typical CCDs on the market (Princeton Instruments for instance) are capable of readout rates ~ 1 MHz (4 seconds readout time for a 2k x 2k CCD) but with a significant readout noise of 7 – 9 electrons. The readout noise can be significantly reduced, at the expense of slower rates. Both characteristics are above our requirements. A CCD equipped with four output amplifiers would reduce the readout time accordingly.

As developments in detector technology are still ongoing, we have assumed in this study that the detector is a Princeton Instruments VersArray 2048B. It is not the best CCD available, in terms of quantum efficiency or readout noise, but its pixel size (13.5 μm) and overall dimensions and characteristics are standard. A better alternative would be the back-illuminated CCD 3041, from Fairchild Imaging : this back-iluminated, 2k x 2k detector, with 15 μm pixels, has a QE higher than 80% in the 350 – 800 nm range, and can be read with four output amplifiers.

We are also considering a new technology, developed at Université de Montréal, by Olivier Daigle and collaborators (Daigle et al. 2008, astro-ph.0807.0363), for instruments such as the 3D-NTT. The new system uses Electron Multiplying CCDs combined with a novel controller, allowing fast readouts (up to

20 MHz) with sub-electron readout noise. However, the largest CCDs available with this type of technology are currently E2V 1600 x 1600. Drissen participates, with C. Carignan and R. Doyon, in a consortium (to be funded by the Canadian Foundation for Innovation) to work with E2V to build larger (2048 x 2048 pixels) detectors.

Finally, charge-transfer CCDs have a much lower readout noise by first transferring the charges from one part of the CCD to the other, allowing to read the detector while integrating with the other half. Only 1k x 2k detectors of this type exist at the moment.

Extensive simulations of signal-to-noise ratios and exposure time efficiency with the three types of CCDs (traditional, charge transfer or EM-CCDs) will be performed during Phase-A.

5 – Development requirements (ABB document – section 4)

6 – Operations and data processing

6.1 - Operations

Our experience with SpIOMM indicates that three people (two astronomers, one night assistant) are needed to install the instrument at the telescope, fill the CCD dewar, start the interferometer and adjust the observing parameters. The whole process takes about three hours. Regular observations can then be made by a single, trained, astronomer. Full training can take about half a day. However, SITELLE is designed to be essentially « plug and play ». As mentioned in the ABB document, most ABB customers know very little about FTS and just want to obtain a spectrum by pushing on a button. Although a detailed users' manual will be provided, our aim is to simplify the observing sequence as much as possible. A resident astronomer will have to be trained in case of a technical problem with the instrument. Because SITELLE will have a wide field of view, pointing the source will never be a problem.

Observing procedure :

Standard calibration include, for each night :

- Bias frames; standard
- Flatfield exposures; standard
- Spectral calibration : the precise spectral calibration is internal to the system (laser metrology), so there is no need for external spectral calibration measurements.
- Flux calibration : observation of standard spectrophotometric stars

Before obtaining a data cube, the observer will have to specify :

- The exposure time per step;
- The spectral resolution; this will determine the number of steps.
- The wavelength range (defined by the filter);
- The detector read mode (full frame or a section of it; binning or not).

An acquisition can be paused at any time (clouds) and then restarted later, without any impact on the data quality. Two datacubes can also be combined to increase the S/N ratio.

After each exposure, the computer will display :

- Both images (from the two output ports);
- The deep, combined image from all exposures (after, say, 10 steps);
- Spectra from selected regions within the FOV, with an increasing resolution after each step.

Storage : the typical size of a data cube is 10 Gb

6.2 - Data processing

The raw data consist of two series of CCD images of the targets (typically 100 – 500), one for each output port of the interferometer. The final product is a single data cube (RA, Dec, λ) from which spectra of individual objects, or monochromatic images of the targets can be extracted. Between the two datasets, the following steps must be followed :

- Standard CCD processing : bias removal, flatfield correction for each image.

- Alignment of the individual images. Unperfect telescope tracking or flexion in the instrument during the observations, however small, can cause slight drifting of the images which need to be corrected. This is done by measuring the centroid of a dozen stars in the field and shift every image accordingly.
- Correction for sky transparency variations.
- Spectral calibration.
- Combination of the two output ports and Fourier transform.

Most of these steps can be performed with standard IRAF procedures (imarith, imshift, daophot, imstack, ...). We have however developped a complete package written in IDL to reduce SpIOMM data. If the proper calibration files (Bias, flatfield, calibration cube) have been taken before the beginning of the night, the whole procedure can be performed on a laptop computer in less than one hour. Data processing would in principle take longer with SITELLE because of the larger CCDs, although by the time SITELLE is installed, the speed and power of laptop computers will have increased. To visualize the data cubes and help with the analysis of the SpIOMM data, we use the free software Karma (<http://www.atnf.csiro.au/computing/software/karma/>), developped by Richard Gooch (Figure 13).

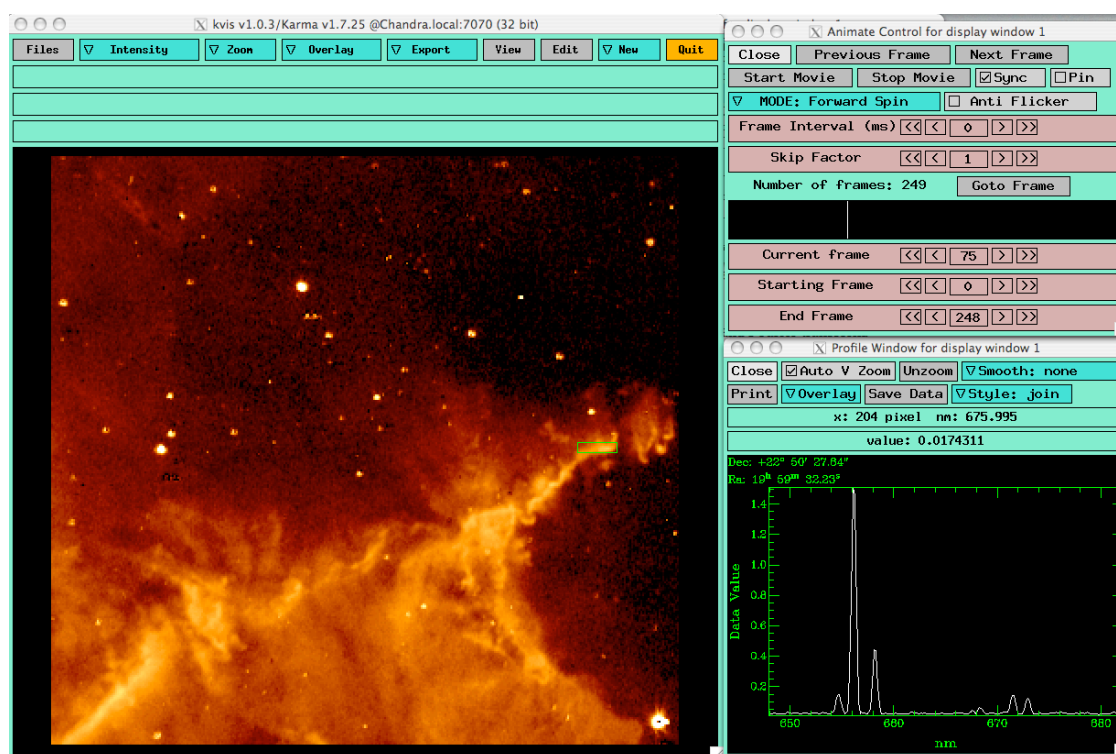


Figure 13 - Example of SpIOMM data as seen with the subroutine *kvis* from the visualisation tool *karma*. The image on the left is the monochromatic image (at 658 nm) of the galactic HII region W4. The average spectrum from the region circled in green is shown in the lower right panel.

In parallel, a similar package was developped for BEAR data; it includes the following programs : *bear_process*, written for the full processing of the BEAR data; *bear_calibration* to flux-calibrate the spectral cubes; *cubeview* to visualize interferograms and spectral cubes, extract spectra or spectral images and save them; and *merge_cube* for merging cubes. All these programs can easily be adapted to SITELLE. A complete data reduction package, based on the two above-mentioned softwares, will be written at Université Laval and provided to the users. We will also provide a « quick look » software

tool that will allow the users to visualize the interferograms and spectra of selected regions as they are built during an acquisition sequence.

7 – Development roadmap and first cost estimate (ABB document – section 5)

7.1 - Sources of funding

Drissen and his colleagues Doyon, Carignan and Bastien (Université de Montréal) have recently submitted a proposal to the Canadian Foundation for Innovation (entitled *Rehaussement de l'Observatoire du Mont Mégantic et Développement d'Instrumentation Astronomique d'Avant-Garde*; PI René Doyon) which includes a significant contribution to SITELLE (2.6 M\$) as well as for the development of large format EM-CCDs. Maillard will also secure funding from the Agence Nationale de Recherche from France if this project is accepted for Phase-A studies.

References

- [1] Stoughton, C. et al. 2002, AJ, 123, 485
- [2] Colless, M. M., et al. 2002, MNRAS, 328, 1039
- [3] Allington-Smith, J., et al. 2002, PASP, 114, 892
- [4] Sanchez, S. F., Becker, T., & Kelz, A. 2004, Astron. Nachr., 325, 171
- [5] Bacon, R., et al. 2001, MNRAS, 326, 23
- [6] Krajinovic, D., et al. 2008, arXiv0807.1505
- [7] Epinat, B., et al., MNRAS, 388, 500
- [8] Maillard, J.-P. & Simons, D. 1992, in *Progress in Telescope and Instrumentation Technologies*, ESO Conference and Workshop Proceedings, ESO Conference on Progress in Telescope and Instrumentation Technologies, ESO, p.733
- [9] Flasar, F. M., et al. 2004, SSRv 115, 169
- [10] Bernath, P. F., et al. 2005, Geoph. Res. Let. 32, L15S01
- [11a] Ridgway, S. T., Carbon, D. F., Hall, D. N. B., & Jewell, J. 1984, ApJS, 54, 177
- [11b] Scoville, N., Hall, D. N. B., Kleinmann, S. G., & Ridgway, S. F. 1979, ApJ, 232, L121
- [11c] Paumard, T., Maillard, J.-P. & Morris, M. 2004, A&A, 426, 81
- [11d] Naylor, D. A., Gom, B. G., Tahic, M. K. & Davis, G. R. 2004, SPIE, 5498, 685
- [11e] Friesen, R. K., Johnstone, D., Naylor, D. A. & Davis, G. R. 2005, MNRAS, 361, 460
- [12] Griffin, M., Swinyard, B. & Vigroux, L. 2005 in *Proceedings of the dusty and molecular universe: a prelude to Herschel and ALMA*, p. 17
- [13] Wurtz, R., et al. 2003, Proc SPIE, vol. 4842, p. 352
- [14] Ridgway, S. T. & Brault, J. W. 1984, Ann. Rev. Astron. Astrop. 22, 291
- [15] Bennett, C. L. 2000, in *Imaging the Universe in Three Dimensions*, ASP Conf. Ser. Vol 195, p. 58
- [16] Graham, J. R. 2000, in *Next Generation Space Telescope Science and Technology*, ASP Conference Series, vol. 207, p. 276
- [17] Morris, S. L., et al. 2000, in *NGST Science and Technology*, ASP Conf. Ser., vol. 207, p. 276
- [18] Posselt, W., et al. 2000, in *NGST Science and Technology*, ASP Conf. Ser., vol. 207, p. 303
- [19] Cox, P., Huggins, P. J., Maillard, J.-P., et al. 2002, A&A, 384, 603
- [20] Drossart, P., Maillard, J.-P., Caldwell, J., et al., 1989, Nature, 340, 539
- [21] Bezard, B., de Bergh, C., Crisp, D., & Maillard, J.-P. 1990, Nature, 345, 508
- [22] Mitchell, G. F., Maillard, J.-P., & Hasegawa, T. I. 1991, ApJ, 371, 342
- [23] Cox, P., Maillard, J.-P., Huggins, P. J., et al. 1997, A&A, 321, 907
- [24] Noel, B., Joblin, C., Maillard, J. P., & Paumard, T. 2005, A&A, 436, 569
- [25] Grandmont, F., Drissen, L., & Joncas, G. 2003, Proc. SPIE, 4842, 392
- [26] Bernier, A.-P., Grandmont, F., Rochon, J.-F., Charlebois, M., & Drissen, L. 2006, Proc. SPIE, 6269, 135
- [27] Drissen, L., Bernier, A. -P., Charlebois, M., Brière, É., Robert, C., Joncas, G., Martin, P., & Grandmont, F. 2008, Proc. SPIE, 7014, 70147K
- [28] Bernier, A. -P., Charlebois, M., Drissen, L., & Grandmont, F. 2008, Proc. SPIE, 7014, 70147J
- [28b] Baldwin, A., Phillips, M. M., & Terlevich, R. 1981, PASP, 93, 5
- [29] Olive, K. A. , & Steigman, G. 1995, ApJ, 489, 1008
- [30] Porter, R. L. et al. 2007, ApJ, 657, 327
- [31] Osterbrock, D. 1989, in *Astrophysics of Gaseous Nebulae and Active Galactic Nuclei* (Sausalito :USB)
- [32] Stasinska, G. 1998, in *Abundances Profiles*, ASP Proc. 147, 142
- [33] Peimbert, M. 1967, ApJ, 150, 825

- [34] Garnett, D.R. 1992, AJ, 103, 1330
- [35] Steigman, G., et al. 1997, ApJ, 490, 187
- [36] Mathis, J.S., et al. 1998, ApJ, 495, 328
- [37] Walter, D.K., et al. 1992, ApJ, 397, 196
- [38] Shaver, P.A., et al. 1983, MNRAS, 204, 53
- [39] Liu, X.W. et al. 1995, ApJ, 450, L59
- [40] Esteban, C. et al. 2004, MNRAS, 355, 229
- [41] Rubin, R. H., et al. 2003, RMxAA Ser. Conf. 18, 113
- [42] Binette, L., Ferruit, P., Steffen, W., & Raga, A. C. 2003, RMxAA 39, 55
- [43] Copetti, M. V. F. 2006, A&A, 453, 943
- [44] Joncas, G. 1999 in *Interstellar Turbulence*, (Cambridge :CUP), 154
- [45] Lis, D.C. et al. 1996, ApJ, 463, 623
- [46] Giammanco, C. & Beckman, J. E. 2005, A&A, 437, L11
- [47] Pilyugin, L.S. 2003, A&A, 399, 1003
- [48] Zhang, Y. et al. 2007, A&A, 464, 631
- [49] Tsamis, Y. G. et al. 2004, MNRAS, 353, 953
- [50] Garcia-Rojas, J. & Esteban, C. 2007, ApJ, 670, 457
- [51] Moore, B. D. et al. 2000, AJ, 119, 2991
- [52] Barriault, L. & Joncas, G. 2007, ApJ, 667, 257
- [53] Lagrois, D. & Joncas, G. 2008, ApJ, in press
- [54] Moore, B. D. et al. 2002, AJ, 124, 3313
- [55] Norman, C.A. & Ikeuchi, S. 1989, ApJ, 345, 372
- [56] Osterbrock, D. E. & Ferland, G. J. 2006, *Astrophysics of gaseous nebulae and active galactic nuclei*, University science books.
- [57] Ferland, G. J., et al 1998, PASP, 110, 761
- [58] Morisset, C. 2006, IAU Symp. 234, 467
- [59] Edmunds, M. G. & Pagel, B. E. J., 1984, MNRAS, 211, 507
- [60] Willner, S. P., & Nelson-Patel, K. 2002, ApJ, 568, 679
- [61] Vilchez, J. M., et al. 1988, MNRAS, 235, 633
- [62] Crockett, N. R., Garnett, D. R., Massey, P., & Jacoby, G. 2006, ApJ, 637, 741
- [63] Magrini, L., Vilchez, J. M., Mampaso, A., Corradi, R. L. M., & Leisy, P. 2007, A&A, 470, 865
- [65] Izotov, Y. I., et al. 2006, A&A, 448, 955
- [66] Bland-Hawthorn, J. & Kedziora-Chudczer, L. 2003, PASA, 20, 242
- [67] Martin, P., & Roy, J.-R. 1994, ApJ, 424, 599
- [68] Zaritsky, D., Kennicutt, R. C., & Huchra, J. P. 1994, ApJ, 420, 87
- [69] Tozzi, P., Ettori, P., Rosati, P., & Borgani, S. 2004, NuPhS, 132, 48
- [70] Molla, M., Cantin, S., Robert, C., & Pellerin, A. 2008, IAU Symp 245, p. 293
- [71] Lilly et al. 1996, ApJ, 460, 1
- [72] Madau et al. 1998, ApJ, 498, 106
- [73] Juneau et al. 2005, ApJ, 619, L135
- [74] Rudnick et al. 2006, ApJ, 650, 624
- [75] Glazebrook et al. 2004, AJ, 128, 2652
- [76] Finkelstein et al. 2008, astro-ph/0806.3269
- [77] Dawson et al. 2007, ApJ, 671, 1227
- [78] Ly et al. 2007, ApJ, 657, 738
- [79] Veilleux, S. 2005, RMxAC, 24, 70



585 Charest Blvd. East, Suite 300
Québec, Québec G1K 9H4, Canada
Phone (418) 877-2944
Fax (418) 877-2834 or (418) 266-1422
www.abb.com/analytical

SITELLE

A wide-field imaging Fourier transform spectrometer for the CFHT

Preliminary Project and Instrument Description

Document Number:	RSSLN19092008	Issue Date:	26 September 2008
Issue:	1	Revision:	b
Distribution:	See page vi	Classification:	N/A
Contract Number:			

PROPRIETARY

The information contained herein is proprietary to and should be considered a trade secret of ABB Bomem Inc. It shall not be reproduced in whole or in part without the written authorization of ABB Bomem Inc.

PR-2100-FO

APPROVALS

	Stamp	Reason for signing
Prepared by Frédéric Grandmont System Engineer		
Prepared by Stéphane Lantagne System scientist		
Prepared by Sylvio Laplante Electronic engineer		
Prepared by Louis-Phillipe Bibeau Mechanical engineer		
Checked by Gaétan Perron Project Manager		
Approved by Andreas Strauch Advanced Eng. supervisor		
Approved by Laurent Drissen, PI		

TABLE OF CONTENTS

1. INTRODUCTION.....	1
1.1 Purpose of Document	1
1.2 Scope of Document	1
1.3 Bibliography.....	1
1.3.1 Applicable Documents.....	1
1.3.2 References	1
1.4 Acronyms.....	2
1.5 Definitions.....	2
2. INSTRUMENT REQUIREMENTS	3
2.1 Preliminary Specifications	3
3. INSTRUMENT CONCEPT	4
3.1 Design Heritage.....	4
3.2 Optical design.....	5
3.2.1 Design Context.....	5
3.2.2 Input / Output Optics Layout	5
3.2.3 Image Quality	6
3.2.4 Transmission	8
3.3 Fourier Transform Spectrometer.....	10
3.3.1 General Description	10
3.3.2 4-port Approach.....	10
3.3.3 Retro-Reflector.....	12
3.3.4 Beamsplitter / Recombiner.....	14
3.4 Mechanical Design and general instrument Layout.....	16
3.4.1 General Description	16
3.4.2 Scanning Mechanism.....	19
3.4.3 Budget Allocations	21
3.5 Electronic design.....	22
3.5.1 General Description	22
3.5.2 Interferometer Control	22
3.5.3 Cameras.....	27
3.6 Key Features Summary.....	28
3.6.1 Key improvements over SpIOMM.....	28
4. DEVELOPMENT REQUIREMENTS.....	30
4.1 Flowdown	30
4.2 Risks	30
4.2.1 Overview	30
4.3 Risks Mitigation	32
4.3.1 Overview	32
4.3.2 I/O optic	32
4.3.3 CC approach.....	33
4.3.4 Instrument Mass	33
4.3.5 Finite Element Analysis.....	33
4.3.6 Performances Simulation	33

LIST OF FIGURES

Figure 1: Unfolded optical design (with telescope).....	5
Figure 2: Unfolded optical design (SITELE only).....	6
Figure 3: Panchromatic Spot Size (center of FOV, 7.2' and 14.4')	6
Figure 4 Panchromatic Spot Size Vertical Cross-Section (Center of FOV)	7
Figure 5 Panchromatic Spot Size Vertical Cross-Section(at 7.2').....	7
Figure 6 Panchromatic Spot Size Vertical Cross-Section(at 14.4').....	8
Figure 7: SF1 Internal Transmittance (20 mm).....	9
Figure 8: New Durable, Protected and Enhanced Silver Coatings from Acton Optics (2007).....	9
Figure 9: An Astronomical IFTS; the dash-dotted square represents the modulator space.....	10
Figure 10: CC based 4-port configuration FTS (CC are represented as 2-D “rooftop” mirrors to ease visualisation of the beam separation).....	11
Figure 11: Plane mirror and corner cube retro-reflectors with their sensitivity to shear and tilt effects.	12
Figure 12: Different Types of Hollow CCs (from left to right: zerodur petals on invar mount, all zerodur, silicon carbide).....	13
Figure 13: Filled Glass CCs (Total Internal Reflection).....	13
Figure 14: CC Useful Area.....	14
Figure 15: Beamsplitter / Compensator Approach using a Single Substrate	14
Figure 16: Beamsplitter / Recombiner Plate	15
Figure 17: 3D Folded Optical Layout.....	16
Figure 18: SITELE Exploded View	17
Figure 19: Honeycomb Construction and Reinforcements Alternatives	18
Figure 20: SITELE Structure Finite Element Model	18
Figure 21: Proposed Long Range Piezo Actuator	19
Figure 22: Moving Mirror Sweep Mechanism (Upside Down View).....	20
Figure 23: Inside View.....	20
Figure 24: SITELE Enveloppe Dimensions	21
Figure 25: Proposed SITELE Preliminary Electronic Design.	22
Figure 26: Servo control loop.....	22
Figure 27: Sampling sequencing.	23
Figure 28: Effect of increasing actuator drive resolution.....	24
Figure 29: Modulated laser reference vs science signal	24
Figure 30: Multi-pass laser reference.	25
Figure 31: Resolution Enhancements.	26
Figure 32: Standard ABB Bomem control board.....	26
Figure 33: New ABB Bomem control board developed under CSA programs.	27
Figure 34: From user requirements to instrument design.	30
Figure 35: SITELE’s influence flow	32
Figure 36: Product development process.....	34

LIST OF TABLES

Table 1: Preliminary Specifications.....	3
Table 2: Honeycomb Preliminary Calculations.....	17
Table 3: Preliminary Mass Budget.	21
Table 4: SITELLE Risk Register.....	31
Table 5: Project milestones	35
Table 6: Cost Estimates.....	Erreur ! Signet non défini.

DOCUMENT CHANGE RECORD

Issue	Rev.	Date	Change Description
1	–	19 Sep 2008	First version
1	a	25 Sept 2008	Second version (various updates)
1	b	30 Sept 2008	Third version (typo corrections by PI)

DISTRIBUTION LIST

The following persons (or company) shall receive this document:

Project Team ☒

Client ☒

Other ☐

<p>ABB</p>	<p>Sitelle</p> <p>Preliminary Project and Instrument Description</p>	<p>Document No: RSSLN19092008</p> <p>Issue: 1 Rev: b Page 1</p> <p>Date: 26 September 2008</p>									
<div> <div>1. INTRODUCTION</div> <div> <div>1.1 PURPOSE OF DOCUMENT</div> <p>The purpose of this document is to report on the work conducted at ABB for the concept study of an imaging Fourier transform spectrometer for astronomy on the Canada-France-Hawaii telescope.</p> <div> <div>1.2 SCOPE OF DOCUMENT</div> <p>The document covers the presentation and justification of the preliminary design established along with suggested development roadmap for ongoing phases.</p> <div> <div>1.3 BIBLIOGRAPHY</div> <div> <div>1.3.1 Applicable Documents</div> <div>1.3.2 References</div> <table> <tr> <td data-bbox="147 1062 217 1089">RD 1</td><td data-bbox="261 1062 440 1089">No doc Name</td><td data-bbox="524 1062 1451 1131">Grandmont F., Développement d'un spectromètre imageur à transformée de Fourier pour l'astronomie, Thèse de doctorat, Université Laval, 2006</td></tr> <tr> <td data-bbox="147 1152 217 1180">RD 2</td><td data-bbox="261 1152 440 1180">No doc Name</td><td data-bbox="524 1152 1369 1222">Morris S. et al., A Canadian IFTS for the NGST, ASP Conference Series, Vol. 207, San Francisco, p. 276-280, 2000</td></tr> <tr> <td data-bbox="147 1243 217 1270">RD 3</td><td data-bbox="261 1243 440 1270">No doc Name</td><td data-bbox="524 1243 1369 1346">Wurtz R. et al., Gallery of datacubes obtained with the Livermore imaging Fourier transform spectrometer, Proceedings of the SPIE, Vol. 4842, p. 352-354, 2003</td></tr> </table> </div> </div> </div> </div> </div>			RD 1	No doc Name	Grandmont F., Développement d'un spectromètre imageur à transformée de Fourier pour l'astronomie, Thèse de doctorat, Université Laval, 2006	RD 2	No doc Name	Morris S. et al., A Canadian IFTS for the NGST, ASP Conference Series, Vol. 207, San Francisco, p. 276-280, 2000	RD 3	No doc Name	Wurtz R. et al., Gallery of datacubes obtained with the Livermore imaging Fourier transform spectrometer, Proceedings of the SPIE, Vol. 4842, p. 352-354, 2003
RD 1	No doc Name	Grandmont F., Développement d'un spectromètre imageur à transformée de Fourier pour l'astronomie, Thèse de doctorat, Université Laval, 2006									
RD 2	No doc Name	Morris S. et al., A Canadian IFTS for the NGST, ASP Conference Series, Vol. 207, San Francisco, p. 276-280, 2000									
RD 3	No doc Name	Wurtz R. et al., Gallery of datacubes obtained with the Livermore imaging Fourier transform spectrometer, Proceedings of the SPIE, Vol. 4842, p. 352-354, 2003									

1.4 ACRONYMS

AR	Anti-reflection
BS	Beamsplitter
CAD	Computer Aided Design
CC	Cube Corner
CCD	Charge-Coupled Device
CFHT	Canada-France-Hawaii Telescope
CSA	Canadian Space Agency
FEM	Finite Element Analysis
FOV	Field of View
FTS	Fourier Transform Spectrometer
FWHM	Full Width at Half Maximum
IFTS	Imaging FTS
IFU	Integral Field Unit
ILS	Instrument Line Shape
IR	Infra Red
OPD	Optical Path Difference
PM	Plane Mirror
PFOV	Pixel Field of View
ROM	Rough Order of Magnitude
STDP	Space Technology Development Program
TBC	To Be Confirmed
TBD	To Be Determined
TBR	To Be Reviewed

1.5 DEFINITIONS

Word: Word Definition

2. INSTRUMENT REQUIREMENTS

ABB has participated to the elaboration of the SITELLE high level specification by helping scientist to constraint their science goals in light of the technology readiness of the associated instrument sub-systems. The SpIOMM instrument is a good starting point to define the technology readiness level of an astronomical IFTS although some of its components (ex. actuator) presents obsolescence issues or are viewed as not sufficiently robust for the reliability level aimed at for a CFHT instrument.

2.1 PRELIMINARY SPECIFICATIONS

Table 1 summarize the main instrument requirements that were drawn from the science goals.

Table 1: Preliminary Specifications

Description	Value
Spectral Range	350 – 950 nm
Spectral Resolution	Better than 4 cm^{-1} (ILS FWHM)
Detector type	$2 \times$ CCDs 16 bits, 2000×2000 pixels
Instrument Field of View (FOV)	20' goal (PFOV = 0.6") 10' threshold (PFOV = 0.3")
Panchromatic image quality	FWHM (350-950 nm) < 1"
Instrument transmittance	> 50% (both output port combined)
Interferometer type	Dual output port
Scanning type	Servoed step scan
Operational temperature range	-15 to 10 °C
Operational vibration	TBD
Humidity	0 to 100%
Mass	750 kg max
Torque	4500 Nm (750 kg @ 0.6 m)
Volume (width x width x length)	$2 \times 2 \times 1.5 \text{ m}$

In comparison to the SpIOMM specification [RD 1], the SITELLE throughput stands as the main challenge. The CFHT primary mirror diameter is 2.2 times the one of Mégantic and the goal FOV is 1.7 x larger than the one of SpIOMM (0.8 x for threshold). Hence the SITELLE throughput requirements sits between 3.4 (threshold) and 13 (goal) times the one of SpIOMM which was already quite an achievement. We think this added challenge is surmountable given the much higher weight/torque limit of CFHT and larger budget. The volume limitations are very similar to the Mégantic ones and as such the SITELLE layout may require additional folding mirrors in the optical path. The remaining requirements are somewhat similar to values that have already been achieved with SpIOMM.

3. INSTRUMENT CONCEPT

3.1 DESIGN HERITAGE

The instrument concept was elaborated based on past experience at ABB Bomem and among team members. The ABB heritage with FTS technology is internationally recognised. Dr. Henry Buijs, co-founder and today's Chief Technology Officer at ABB Bomem started to work on FTS design as an undergraduate student. The balloon borne FTS systems he worked on obtained in 1962 the first spectra of night airglow even before the introduction of the FFT algorithm in 1965. ABB Bomem celebrated in 2008 its 35th anniversary of existence in design, manufacturing and commercialisation of FTSS. ABB delivered its first multi-pixels FTS instrument in the early 90's in the form of a 4 X 8 parallel output array IR detector. Since then other custom imaging systems have been delivered but with limited capacity in terms of number of pixels due to availability and cost of IR array detector. In 2008, the ABB commercial line of spectrometer was expanded with the introduction of the first standard imaging FTS product capable of up to 32 cubes per seconds on arrays of 240 x 320 pixels. Visible range FTS were commercially sold by ABB since the early 80's but the first imaging version in this wavelength range came with the JWST (formerly NGST) IFTS proposal in 1999 [RD 2]. A joint Canadian-US technology demonstration effort involving a team from ABB and the Lawrence Livermore National Laboratory resulted in the construction of the LIFTS instrument which was used at Apache point 3.5 m, Lick 3m and Palomar 5m [RD 3]. The LIFTS used two 1K x 1K CCD which were binned to form 512 x 512 pixels images. Building on lessons learned from the LIFTS, the SpIOMM project was started and is the IFTS with the largest number of pixel (1340 x 1300) ever built across all science fields and wavelength range in the world.

ABB's heritage in space design also benefit to the current effort by bringing specialized expertise in the following field:

- Thermal & structural modeling
- Lifetime and reliability modeling
- Thermal vacuum operation & testing
- Contamination control

Our design software suite includes the following:

- Zemax for optical design & performance simulation
- ProEngineer for CAD modeling
- NASTRAN for FEM
- Matlab for end to end performance simulation
- Orcad Pspice for electronic design

3.2 OPTICAL DESIGN

3.2.1 Design Context

The design of an IFTS with such emphasis on the imaging/throughput aspect obviously starts by attempting to meet the FOV and image quality requirement over the desired wavelength range simultaneously. This is a challenging task compared to similar astronomical instrument. One on side, wide field camera system can typically suffer from chromatic aberrations to some degree since band pass filter are typically used and allows for a focus correction. On the other side, Integral field unit spectrometer will typically image a much smaller FOV than SITELLE or, if not, allow for very coarse spatial sampling of it (hence poor image quality). All images acquired with an IFTS are meant to be panchromatic and take full advantage of all the available detector pixels for imagery. Band pass filters can still be used but primarily to reduce the photon noise in the spectra and not specifically to improve image quality.

The optical design process can be carried out almost independently from the interferometer design as the latter typically adds only folding or transmissive flat interfaces which effect on the optical performances are often negligible. However the IFTS configuration brings some additional requirements to the optical design such as the need to dispose of a collimated beam section of sufficient length to place the interferometer. In this first optical design iteration, the free collimated space length was fixed at 1 meter.

3.2.2 Input / Output Optics Layout

The I/O optics design was realised by S. Thibault at Laval University. The intent was to converge to a solution that provided the largest FOV without compromising the wavelength range and image quality threshold as dictated by the science requirements. The SpIOMM design was used as a starting point. The proposed layout is composed of a triplet for input optics and 5 lenses in the output optics. It is presented in Figure 1 and Figure 2.

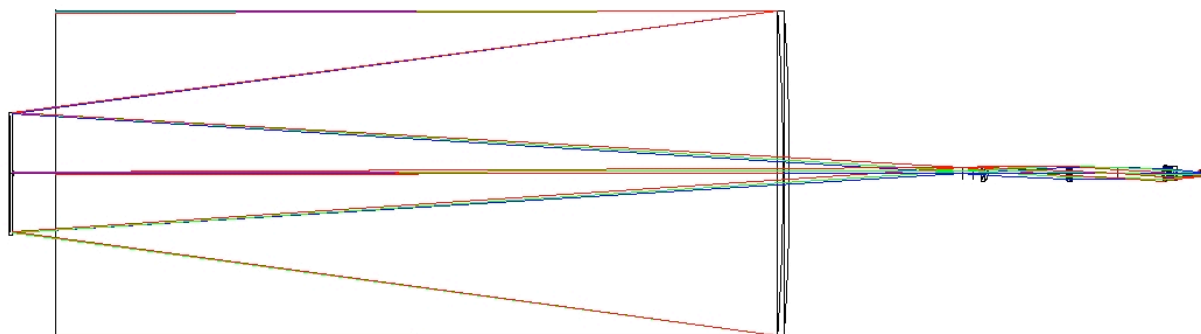


Figure 1: Unfolded optical design (with telescope)

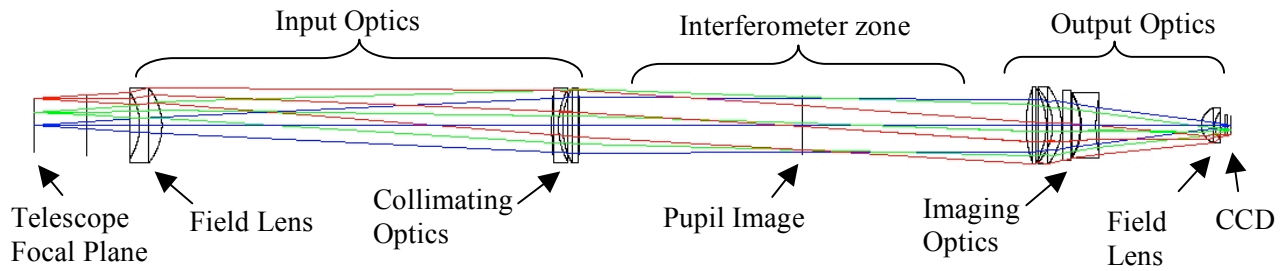


Figure 2: Unfolded optical design (SITELE only)

The pupil size is a free parameter in the design. It is directly linked with the size and hence cost of the interferometer. However a small pupil makes the design of the output optics more difficult and may reduce the attainable FOV. The first design iteration fixed the pupil at 120 mm and a resulting **FOV optimised over a diameter of 14.4 arc minutes.**

3.2.3 Image Quality

The proposed design generates the spot size presented in the four following Figures.

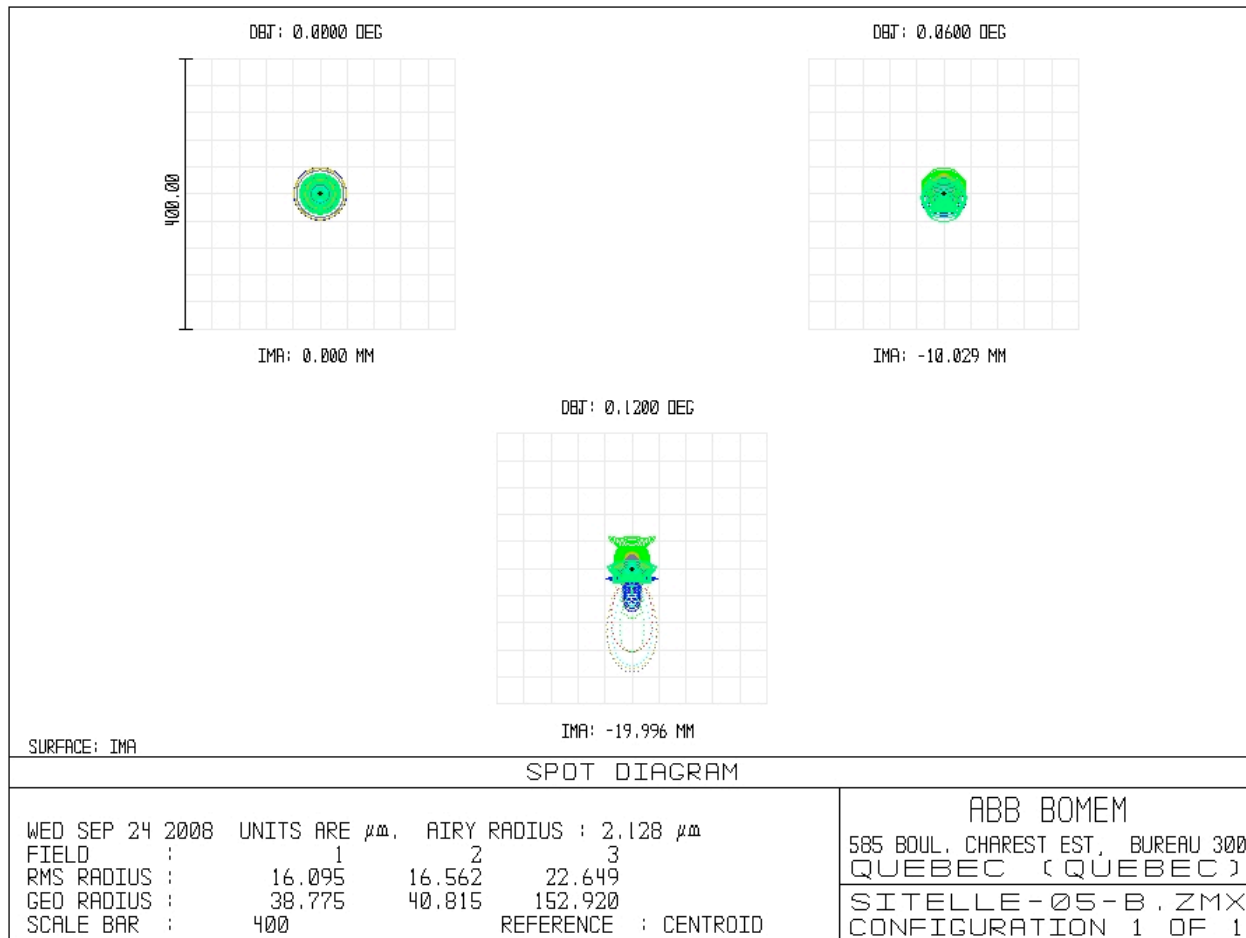


Figure 3: Panchromatic Spot Size (center of FOV, 7.2' and 14.4')

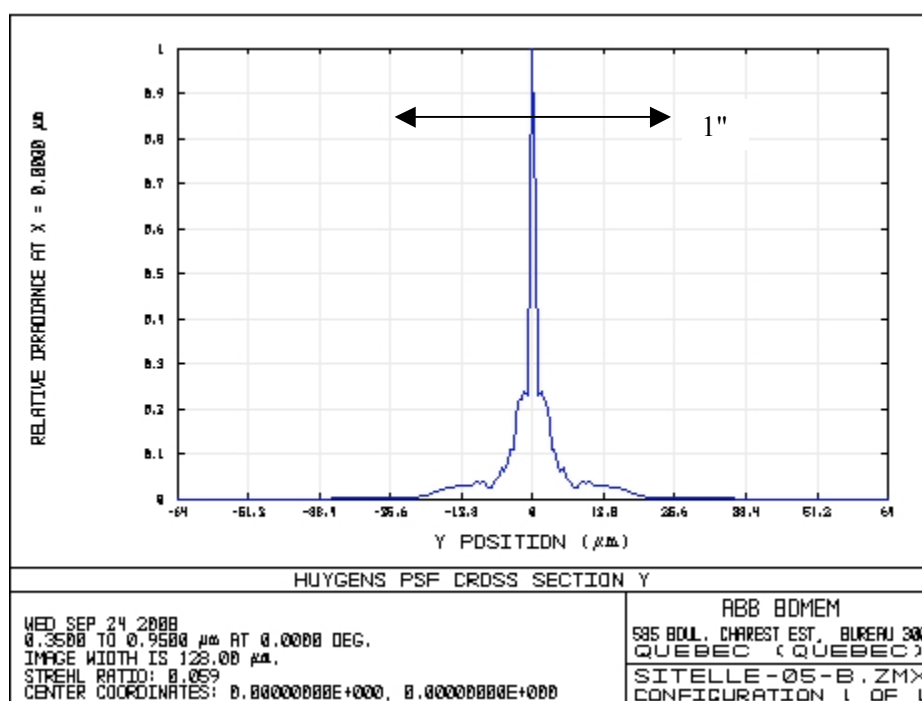


Figure 4 Panchromatic Spot Size Vertical Cross-Section (Center of FOV)

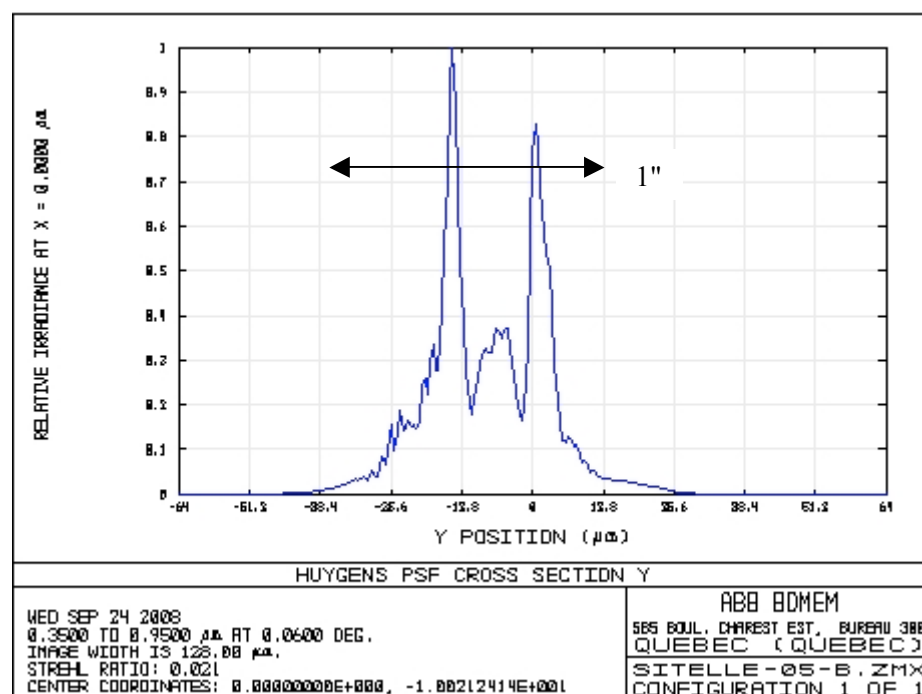


Figure 5 Panchromatic Spot Size Vertical Cross-Section (at 7.2')

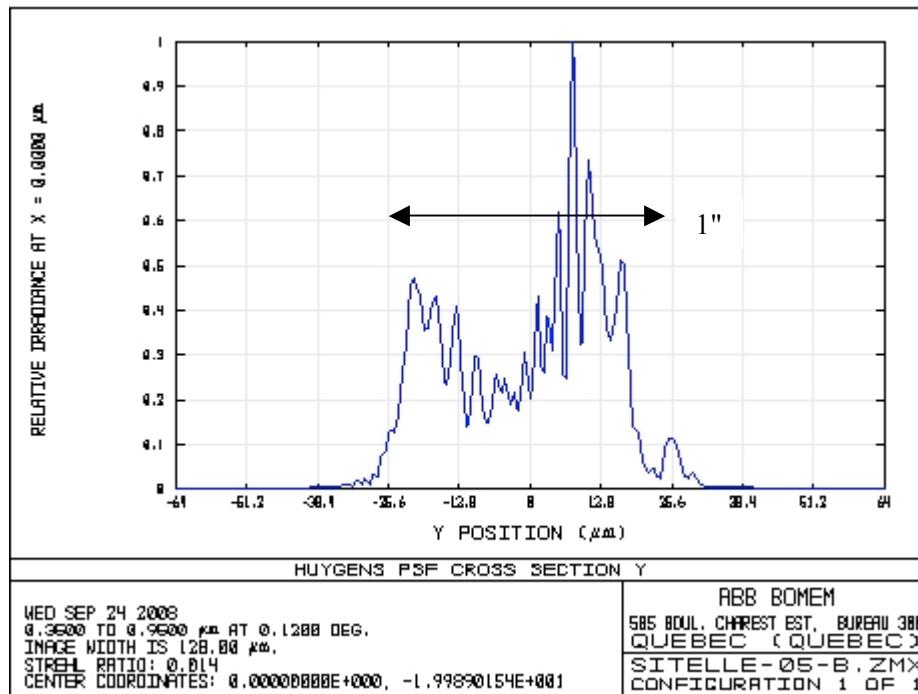


Figure 6 Panchromatic Spot Size Vertical Cross-Section(at 14.4')

We chose the Y axis cross section (in direction to the center of the FOV) view since it is the one that shows the widest spread. One can see that the spot size FWHM falls below the 1 arc second limit for the optimised FOV. Note that these cross section graph were generated using a finite number of wavelength between 350 – 950 nm (by increments of 50 nm) and that flat continuum source simulation would generate figures with less high frequency variations but similar general shape.

3.2.4 Transmission

The glasses used in the design are UV grade fused silica, CaF₂ and SF1 (only one lens). This latter material has a high index of refraction and exhibit transmittance that quickly drops below 400 nm. The transmittance for a 20 mm path is shown in Figure 7 and corresponds to the overall system transmittance as it is by far the dominant contributor. Other alternative to the SF1 should be studied in the next phase in order to improve transmittance at the short wavelength end.

On top of the curve shown in Figure 7, one must add the AR coating performance on each of the 16 surfaces of the lens train. Typical values attainable on glass of 4% Fresnel reflection (uncoated surface with $n = 1.5$) will average near 1%. The result will be slightly higher for SF1 which Fresnel reflection is 6.7 %. Hence, one can expect the AR coating to have a global transmission between 80% and 85% and also show additional variation of this order (5%) as a function of wavelength typical of multilayer interference coatings.

It will also be seen in the mechanical section that 3 folding mirrors were added to the optical train in order to fit the mass/volume allocation of CFHT. The losses caused by these mirrors can be limited to less than 6% across the spectral range using the latest developments in coating technology (<http://www.piacton.com>) as seen in Figure 8.

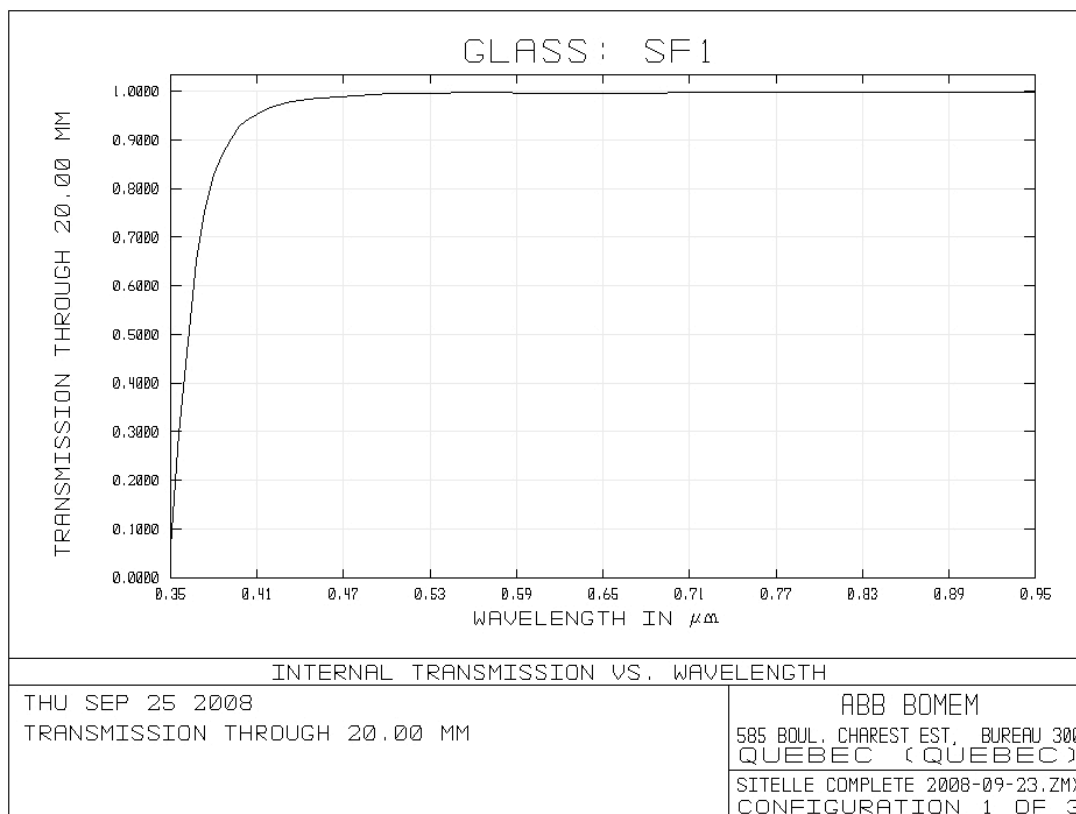


Figure 7: SF1 Internal Transmittance (20 mm)

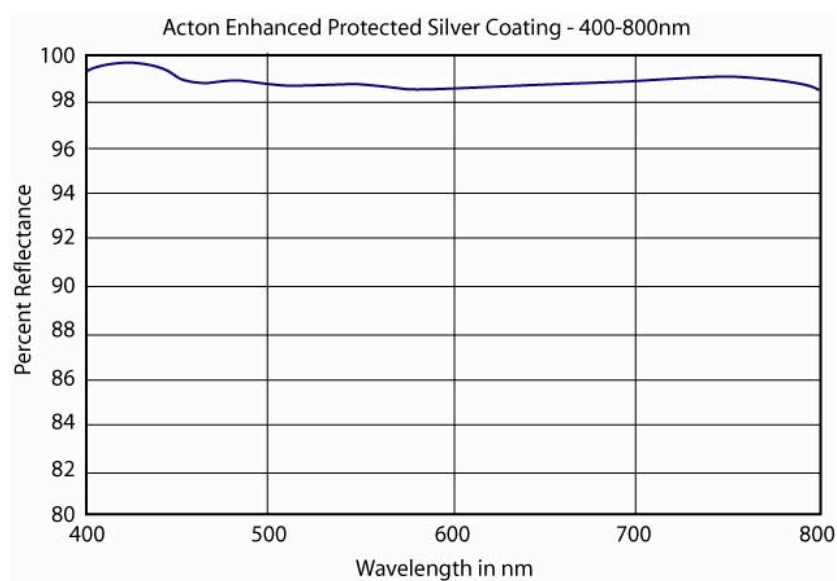


Figure 8: New Durable, Protected and Enhanced Silver Coatings from Acton Optics (2007)

3.3 FOURIER TRANSFORM SPECTROMETER

3.3.1 General Description

The purpose of the modulator (or interferometer) in a IFTS system is to modulate the panchromatic image intensity of the scene. This is done by splitting the collimated beam in two parts, applying an optical path difference (OPD) between them and finally recombining both beams such that they interfere. In a FTS measurement, the OPD is scanned over a given range around the zero path difference (ZPD) and the measured signal intensity recorded as a function of OPD is called an interferogram. The desired optical spectrum of the source, more precisely the spectral density of its intensity, is obtained after a Fourier transform of the interferogram. We can consider the FTS as a device that performs a Fourier transform mechanically.

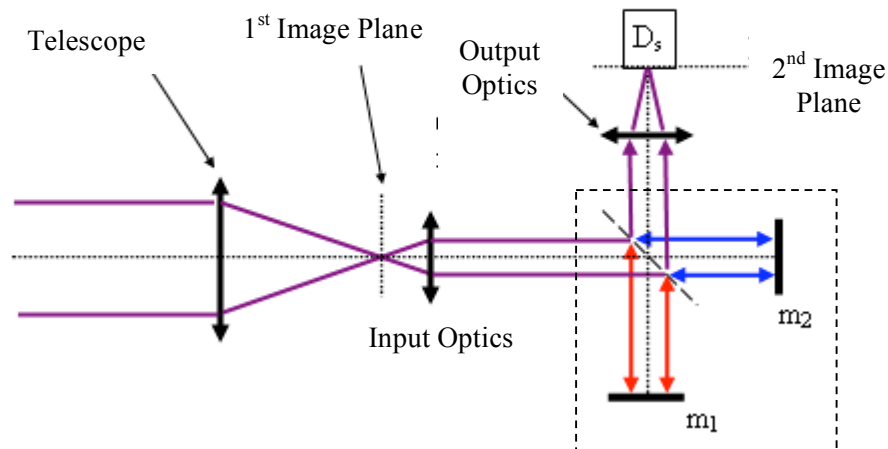


Figure 9: An Astronomical IFTS; the dash-dotted square represents the modulator space.

3.3.2 4-port Approach

A classic Michelson interferometer is shown inside the dash-dotted square box of Figure 9. Such interferometer configuration is said to have two ports; one entrance port and one output port hence a single detector. In fact, interferometers inherently generate two output beams. In the classic configuration shown, the second output port is superimposed on the input port. Hence half of the light goes back to the source. In practice, the proportion is not necessarily 50% but depends on the OPD. The total incident power from a point source will exit in one output or the other depending on the interference at a given OPD hence the two output ports are complementary.

The 50% light loss of 2-ports FTS can be avoided using a 4 ports design in which each of the 4 ports occupy a different position in space. This separation allows the use of 2 cameras and collection of the total incident power. The same can be said about the second input port that is superimposed on the main output port of Figure 9. i.e. the detector sees itself in the m1 mirror across the beamsplitter.

Decision to enter light through either input is a question of space optimization. Nevertheless the second input must be controlled to prevent stray light from adding to the signal.

A 4-ports interferometer can be obtained in various ways. The most common way is to use retroreflectors (cat's eye mirror or cube corner, CC) that translate the beam sideways before returning it. Figure 10 presents a CC based interferometer used in 4-port configuration. The figure shows divergent beams of symmetrical situation in respect to the beam splitter (BS) plane because the pupil in the collimated space is chosen at the location of the corner cubes (CC) apex

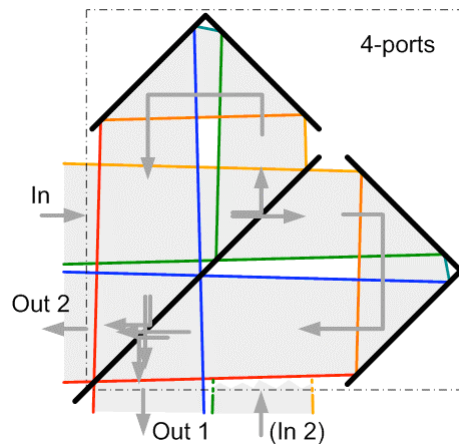


Figure 10: CC based 4-port configuration FTS
(CC are represented as 2-D “rooftop” mirrors to ease visualisation of the beam separation)

The SpiOMM IFTS achieves the beam separation with plane mirrors by inserting the science beam at an angle. The reflected beam exits at twice the incident angle with respect to the input which can allow for a complete separation of the two beams at a certain distance from the reflection point. The comparison of CCs and PMs in terms of footprint and mass in a 4-port configuration gives a large advantage to PMs because the CC's must be at least twice as large in one axis and their depth is at least half the beam diameter and the total surface is larger (and thus the mass).

The description of the plane mirror is trivial and the main parameters of interest are its surface quality (flatness) and its spectral reflectivity. On the other hand, corner cubes are much more complex items because they require three orthogonal surfaces that are accurately at right angle from each other, forming a 3D object that is well described by the corner of a cube (thus their name). A CC is also known under the name of retroreflectors because they reflect any incoming light exactly at the same angle as it entered the CC but with a potential lateral translation (shear) that depends on the distance and orientation between the beam center and the CC's apex (location in the CC where the three surfaces intersect). In addition to the surface quality and spectral reflectivity properties, the alignment mismatch of the three surfaces is a critical parameter. A deviation from the right angle condition in the CC assembly induces tilt effects on the reflected beam and due to multiple reflections in the CC, no less than six reflected sub-components with different angles are possible. Nowadays, the error in the expected angle of reflection (parallelism loss) is under 1 arcsec for state-of-the-art CCs, which leads to low impact in FTS applications.

However, in the case of an imaging FTS, the shear effect is greatly reduced, but not the tilt. Using CC greatly improves the stability and the performances of an imaging FTS. Once CCs are built and tested, their geometry does not change and performances are stable. For PM, a dynamic alignment system is required, and the instrument performances depend on the dynamic alignment performances. For these reasons and also based on the SpIOMM experience, a CC based approach is preferred.

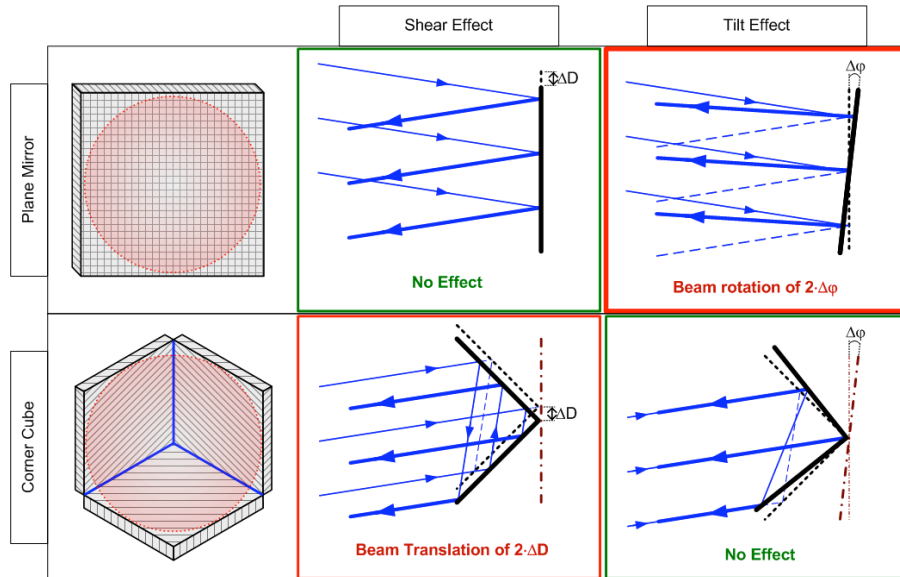


Figure 11: Plane mirror and corner cube retro-reflectors with their sensitivity to shear and tilt effects.

3.3.3 Retro-Reflector

Two types of corner cubes are considered. The first type is made of glass and the second type is made of 3 mirrors treated for UV performances. The required characteristics for corner cubes in general are: excellent orthogonality to minimize wave front errors, high reflectivity to minimize losses, and insensitivity to temperature changes. Of course, surfaces quality must be appropriate for UV measurements. Because SITELLE is a 4-port FTS, only a portion of each retro-reflector is used, and their shape can be optimized to reduce their mass, volume, and cost. Anti-reflection coating need to be applied to the front surface for glass retro-reflector, while 3-mirror corner cubes require a high reflecting coating. The reflecting surfaces for glass retro-reflectors don't need any special treatment since the reflections occur by total internal reflection. The final choice of retro-reflector type will be done after comparative studies are completed.

The advantages for filled glass corner cubes are:

- 1) Two AR reflection losses are smaller than 3 broadband metallic coating reflection losses
- 2) Corner cube orthogonality does not change with temperature
- 3) Ease of polishing (external surfaces)

The disadvantages for fused silica corner cubes are:

- 1) Wave front deformation caused by refractive index non-homogeneity.

- 2) High mass
- 3) OPD could present a strong spectral dependence (temperature effect linked to dispersion)

The use of glass retro-reflector has a major drawback, the optical path inside the medium is important. The homogeneity of the substrate will affect the wave front error and the modulation efficiency of the modulator. The 3-mirror corner cubes do not suffer from this.

The advantages for 3-mirror corner cubes are:

- 1) Lighter mass
- 2) Independent of index of refraction

The disadvantages for 3-mirror corner cubes are:

- 1) 3 reflecting surfaces for each corner cube
- 2) Corner cube orthogonality may change with temperature
- 3) Very difficult (or expensive) to manufacture to the accuracy and size required.

In both cases, the 2 corner cube size used as retro-reflector is determined by the beam diameter. The mass is important at the current size, 320 mm height and 160 mm width. The need for orthogonality is amplified because of the beam diameter.

In the end, what is needed for the current design is a transmitted wave front error lower than $\lambda/20$ RMS and a beam deviation (input to output residual angle) of less than 0.5 arc second (goal 0.25").

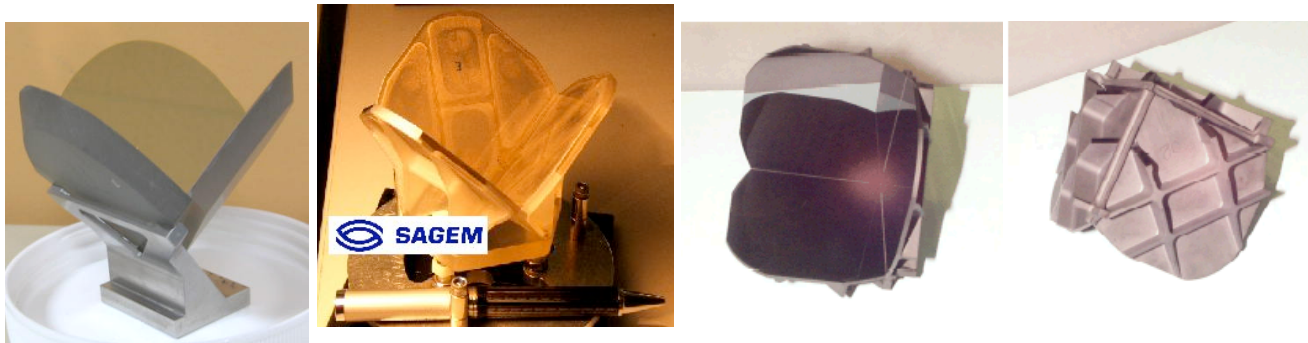


Figure 12: Different Types of Hollow CCs
(from left to right: zerodur petals on invar mount, all zerodur, silicon carbide)



Figure 13: Filled Glass CCs (Total Internal Reflection)

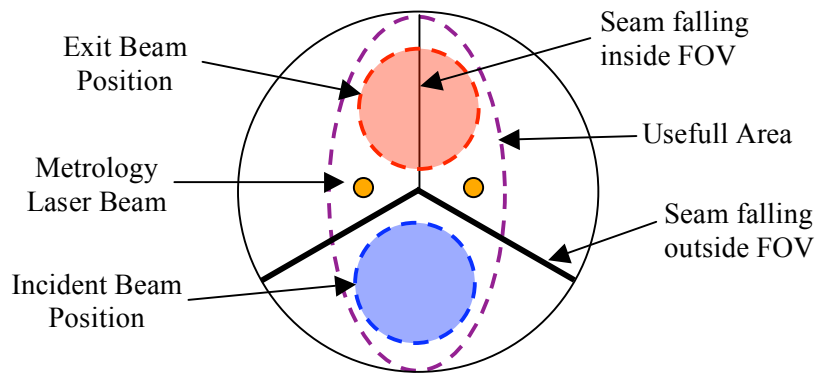


Figure 14: CC Useful Area

3.3.4 Beamsplitter / Recombiner

Because SITELLE is a CC-based 4-port FTS with 120 mm pupil, the beam splitter must have a diameter of 320 mm and a suggested thickness of 30 mm. Like the corner cubes, the beam splitter, which acts as a recombiner too, is only partially used (Figure 16). Its shape can also be optimized for mass, volume, and cost and to minimize wave front deformation caused by gravity or temperature gradient. The proposed material is UV-grade fused silica. Also, wavefront deformation must be minimized, the impact on performances is more challenging in the UV; at least $\lambda/20$ RMS is needed.

The complete separation of the input and output beams on the beamsplitter allows the use of a single substrate to carry the functionality of splitting, recombining and compensation between both interferometer arms' optical path. The compensation ensures that light goes through the same total thickness of glass in each arm as shown in Figure 15. Anti-reflection coating and semi-reflection coating position must be flipped between the first and the second pass for this to work. The compensation is needed to obtain a symmetric interferogram and compensate the chromatic dispersion in the BS substrate glass.

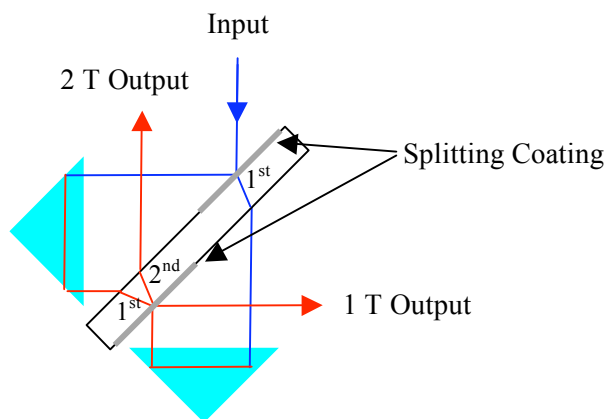


Figure 15: Beamsplitter / Compensator Approach using a Single Substrate

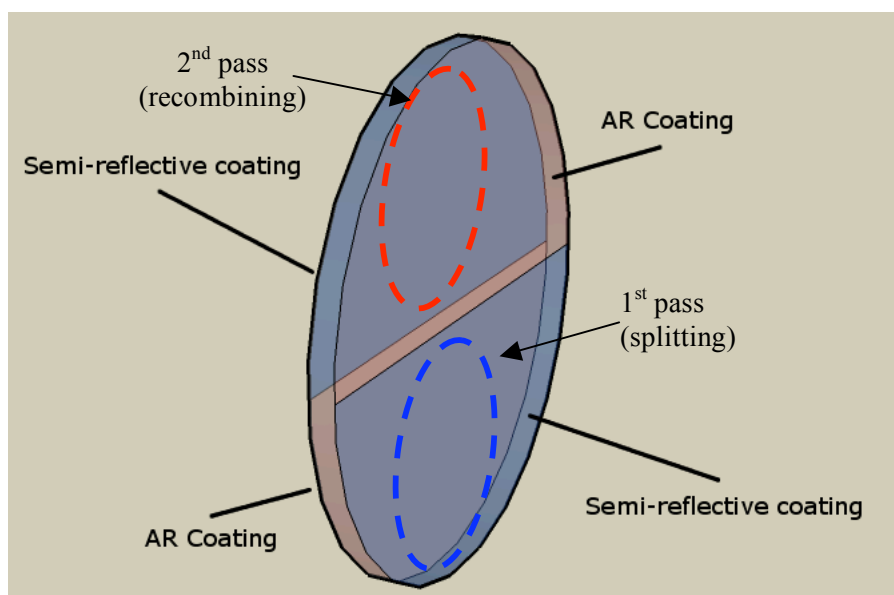


Figure 16: Beamsplitter / Recombiner Plate

3.4 MECHANICAL DESIGN AND GENERAL INSTRUMENT LAYOUT

3.4.1 General Description

The instrument is divided in four parts: the input optics, the modulator, the output optics, and the cameras. When layered sequentially, the total instrument length extends much beyond the 1.5 meter limit and must therefore be folded. Two folding mirrors located before and within the input optics lens set are used to fit the volume allocation and position the instrument's center of gravity as close as possible to the telescope's optical axis. After exiting the input optics, the science beam enters the modulator at the bottom of the beam splitter. Each corner cube retro-reflector will translate the beam up, and returning it to the beam splitter upper portion. After that, both outputs are folded up toward the telescope in order to bring the camera and lens assembly closer to the mounting interface.

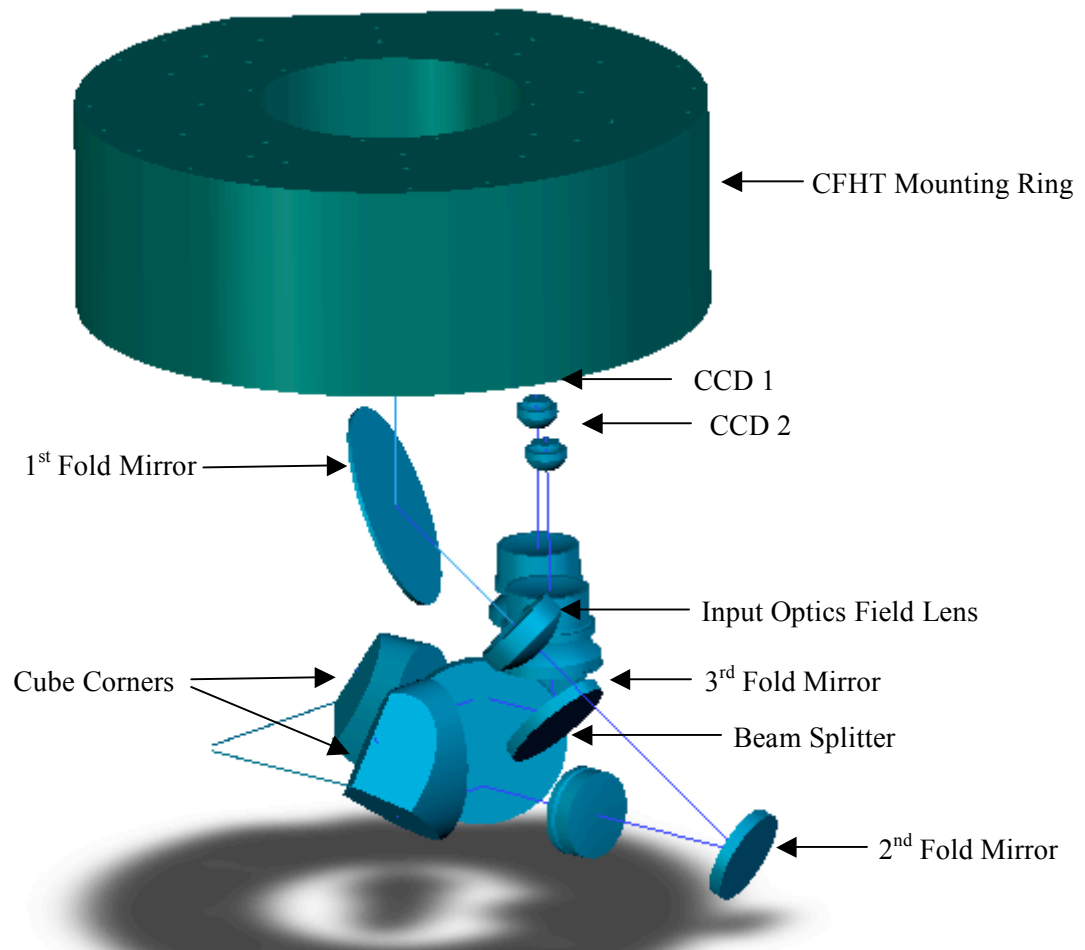


Figure 17: 3D Folded Optical Layout

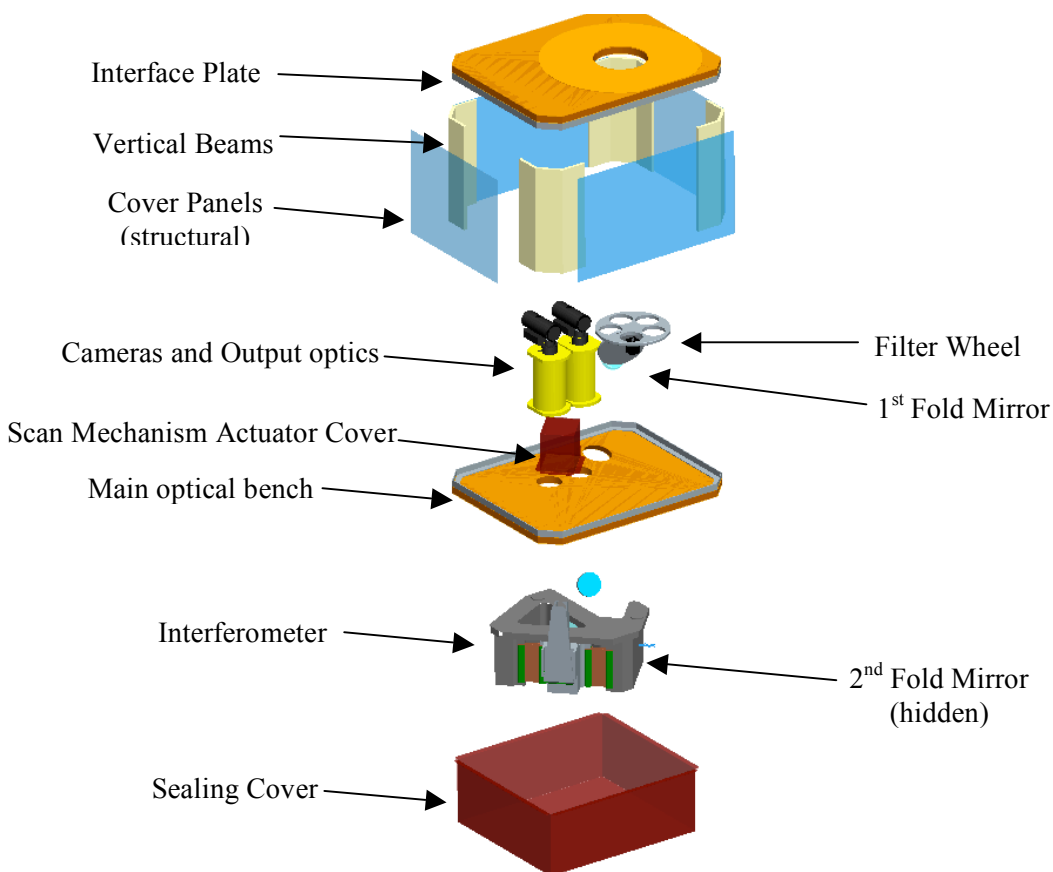


Figure 18: SITELLE Exploded View

Structural integrity is assured by two main honeycomb panels due to instrument size and stiffness-to-weight ratio (designed as the optical bench and the interface plate). These will be customised in order to get local reinforcements for instrument mounting points (see Figure 19). Preliminary calculations were made using Hexcel Composites or Paneltec datasheet (www.panelteccorp.com) and are summarised in Table 2.

Table 2: Honeycomb Preliminary Calculations.

Parameters	Value
Approximate dimensions	1 m X 1m
Core designation	3003 aluminum, 6 mm cells, density of 83 kg/m³
Faces sheet	Thickness of 50.8 mm
Load	6061-T6 aluminum (1 mm each)
Deflection (maximum at center, edges simply supported)	3200 N/m² (320 kg)
Racing stress	0.35 mm
Core stress	3.1 MPa
Local compression	0.02 MPa
Mass	Negligeable (uniform load)
	7 kg

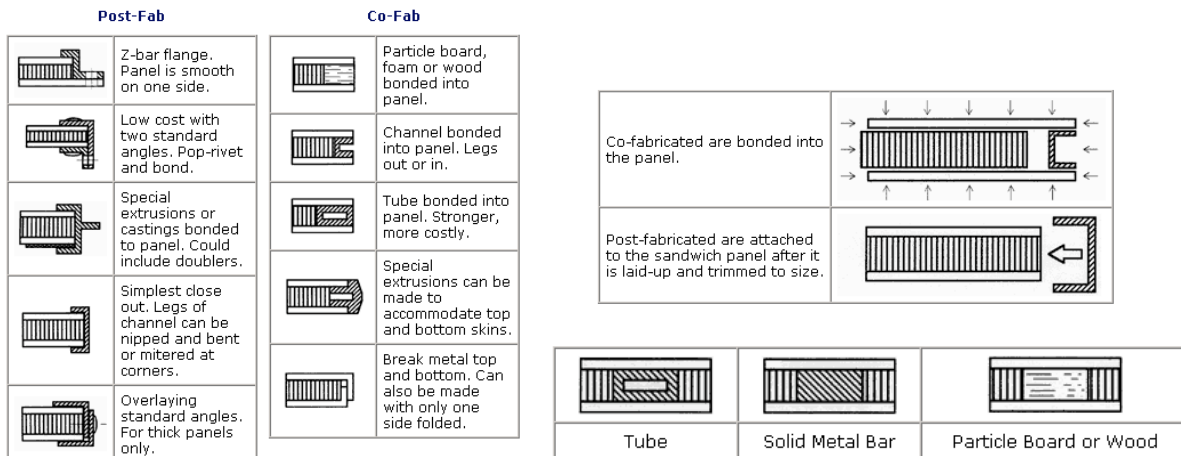


Figure 19: Honeycomb Construction and Reinforcements Alternatives

The proposed design is assuming standard 2 inches, all-aluminum panels. However, if we need to get a higher stiffness and a lower thermal expansion coefficient, other materials like Kevlar or carbon fiber laminate (with a proper orientation choice) may be more suitable but more expensive.

Around both plates, L-shape beams will be mounted in order to connect both plates to the lateral frame. Upper and lower honeycomb will be connected by custom aluminum beams and another set of honeycomb panels (approx. 1 inch thick). Side panels will be sized in order to get an acceptable stiffness in all directions based on detailed FEM results and final optical tolerances. To minimize air turbulence, the modulator section will be sealed using panel pressed against a groove enclosed rubber seal similar to what is found in vacuum equipment. The concept also has a filter wheel located directly under the mounting plate.

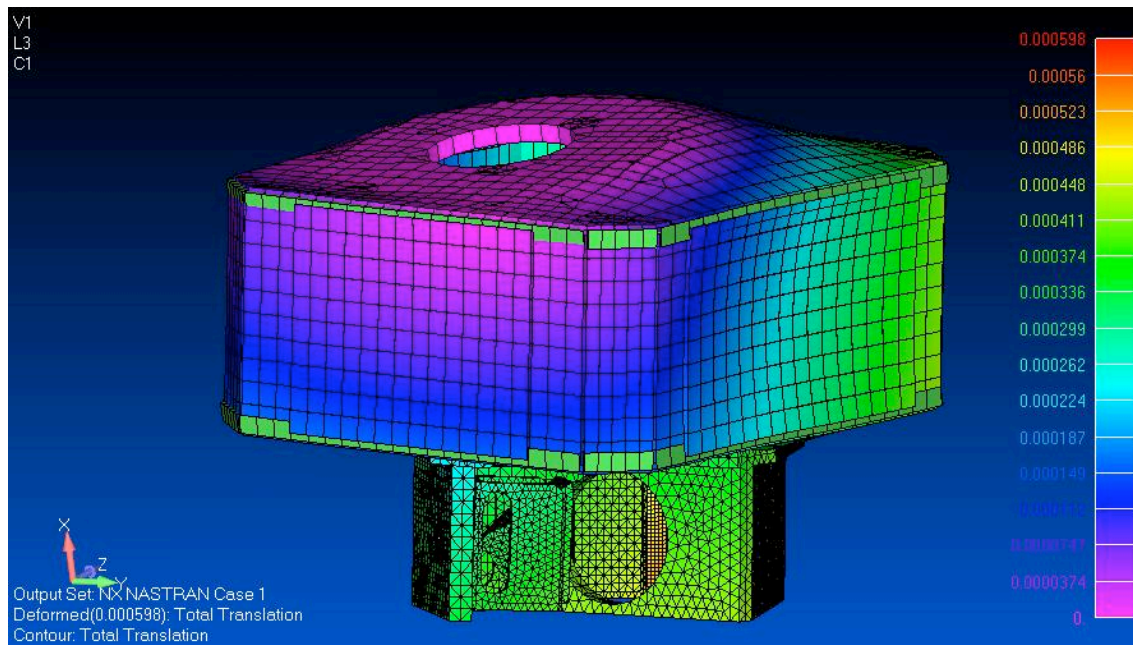


Figure 20: SITELLE Structure Finite Element Model

3.4.2 Scanning Mechanism

For SITELLE, the scanning mechanism must combine the following capabilities:

- Nanometer-level precision
- Travel range > 1.5 mm
- Fast response (kHz)
- No backlash
- Strong hold/push force

In order to achieve this kind of performance, a dual stage actuator scheme is proposed. For coarse displacement, one corner cube will be displaced by a long range, medium force and relatively slow piezo-actuator. The current proposed actuator is the PI Nexline (www.pi-usa.us) shown in Figure 21.

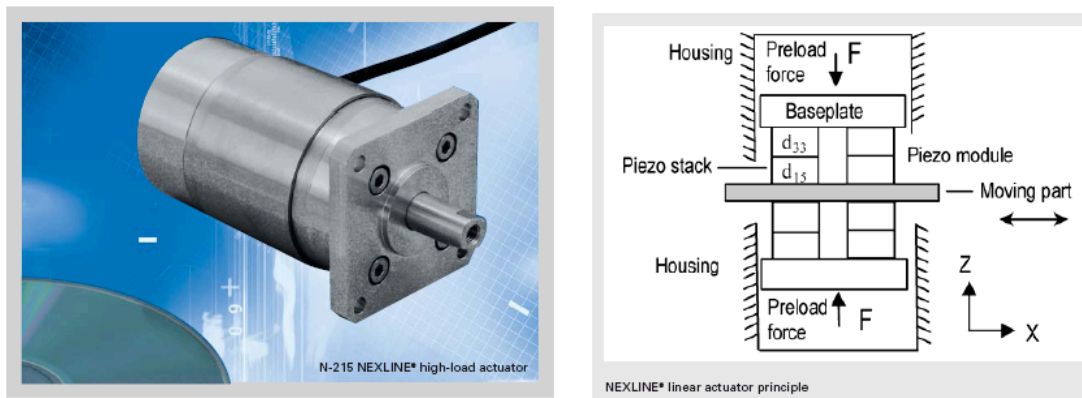


Figure 21: Proposed Long Range Piezo Actuator

Total displacement will be about ± 0.75 mm around mechanical equilibrium position. Rectilinear and frictionless motion will be assured by a proper flex blade design (see Figure 22). Blade thickness will be adjusted in order to get maximum stiffness and acceptable stress and required forces (taking into account the membrane effect). Initial calculations show that the blade stiffness required to properly hold the CC generate push force above the proposed actuator capacity. Hence, a simple flex blade based lever arm mechanism is used to increase the actuator force.

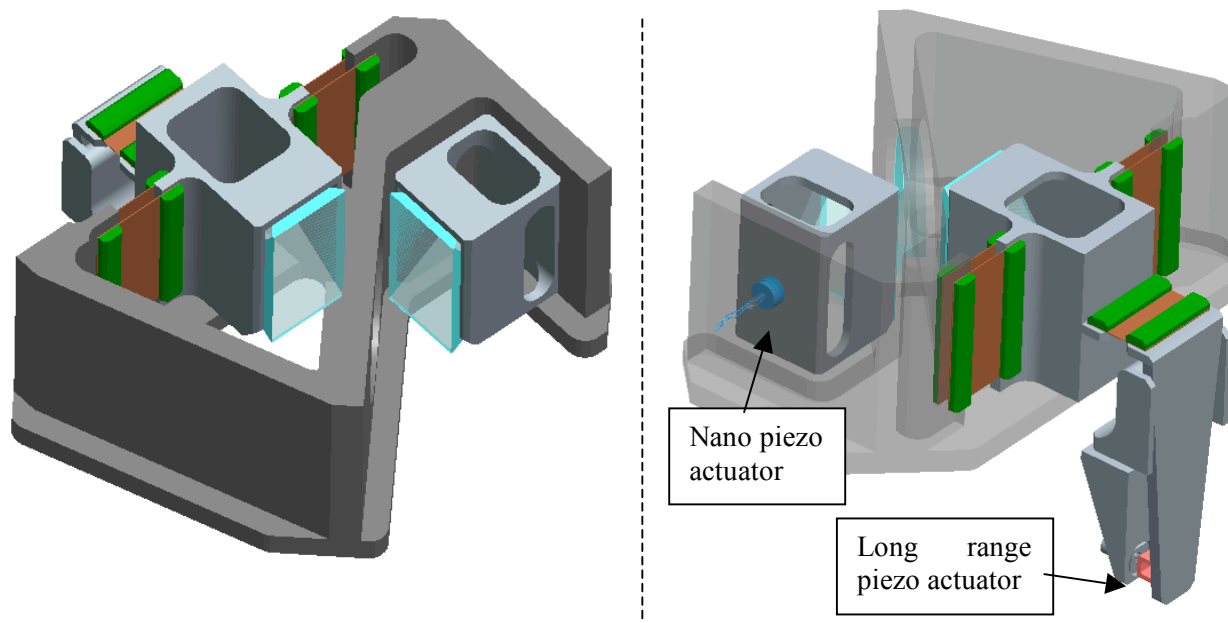


Figure 22: Moving Mirror Sweep Mechanism (Upside Down View).

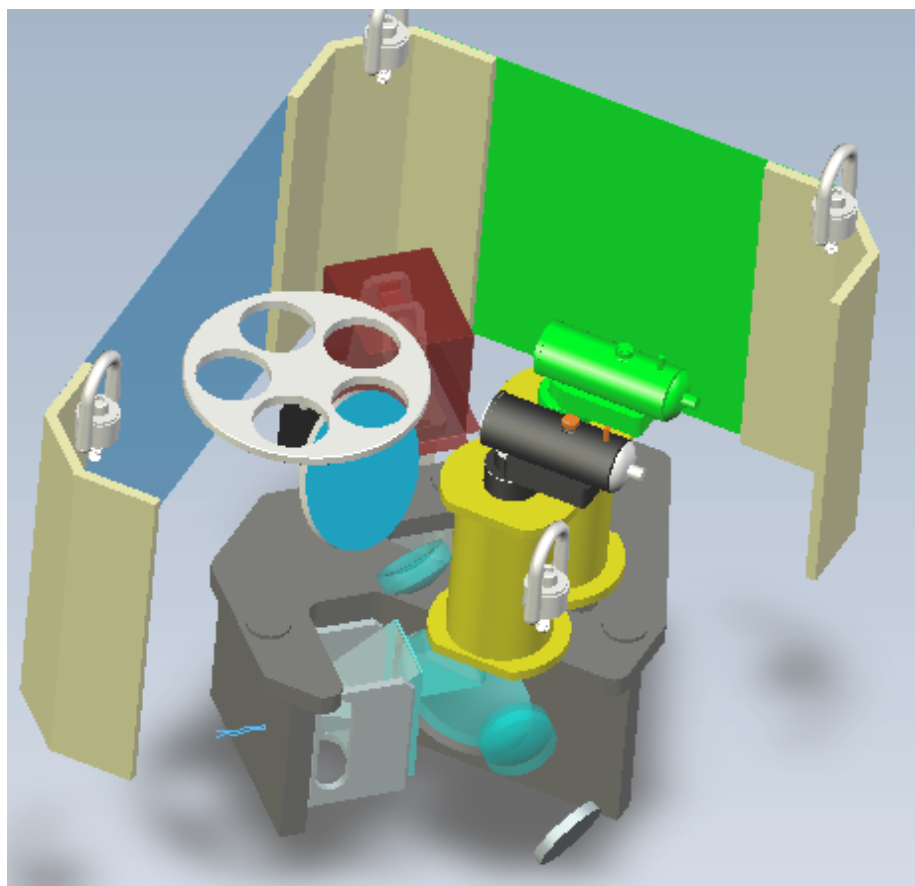


Figure 23: Inside View

3.4.3 Budget Allocations

Table 3: Preliminary Mass Budget.

Components	Preliminary mass [kg]	Mass with contingency [kg]
Interface bench	7	14
Optical bench	7	14
Cover Panels (4)	12	24
Corner cube assembly (long range travel)	95	95
Corner cube assembly (short range travel)	44	44
Structural ring (L shape beams)	27	34
Vertical beams (4)	80	100
Camera lens assembly (2)	70	90
Beam splitter	15	15
Interferometer structure (BS wall)	105	131
Filter wheel	9	14
Pivot mechanism (long range)	14	21
Black camera (2)	12	12
Other (lens, brackets, folding mirrors, etc...)	25	50
Total	520	660

The mass budget assumes that the filled glass CCs are used (worst case). It is clear looking at the mass distribution that additional gain can be made on the heaviest elements such as the interferometer structure from pocketing or use of composite material. It is expected that if the interferometer beam size can be reduced to 80 mm (at the expense of a smaller field of view however), the first high incidence angle fold mirror can be removed. This would have a positive impact on the optical performance but would bring the instrument length very close to the 1.5 meter length limit and increase the weight slightly due to the increased distance between the main optical bench and the mounting surface.

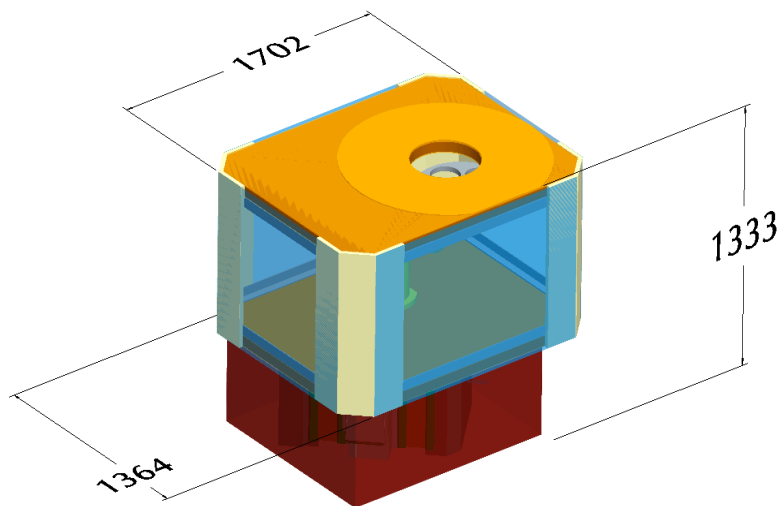


Figure 24: SITELLE Enveloppe Dimensions

3.5 ELECTRONIC DESIGN

3.5.1 General Description

The instrument electronics is kept as simple as possible (Figure 25). The plan is to use an existing standard communication interface like USB to communicate with the Interferometer Electronic. This will allow the use of standard embedded PC as Local Control Electronic to manage the instrument sequencing. The command and data transfer between the instrument and the remote PC is done via a Gigabit Ethernet. The CCD cameras can use a specialised interface connected directly to the Remote PC or be driven by the Local Control Electronic directly. It is expected that the selected camera will have PC compatible frame grabber card with communication functions ready to use

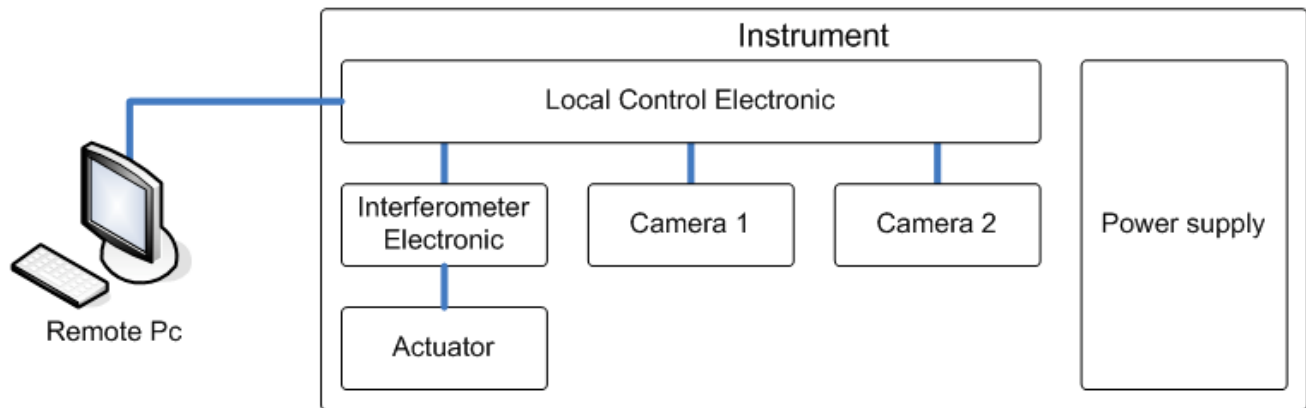


Figure 25: Proposed SITELE Preliminary Electronic Design.

3.5.2 Interferometer Control

Since the SITELE instrument has to integrate the light for a relatively long time to achieve an accurate measurement a given interferogram point we have to stop the interferometer at fix OPD intervals and keep this position as stable as possible. This will be done by a servo control loop. To ensure good performance of the servo loop we have to work on every element of the chain schematically represented in Figure 26: the command, the controller, the actuator and the feedback.

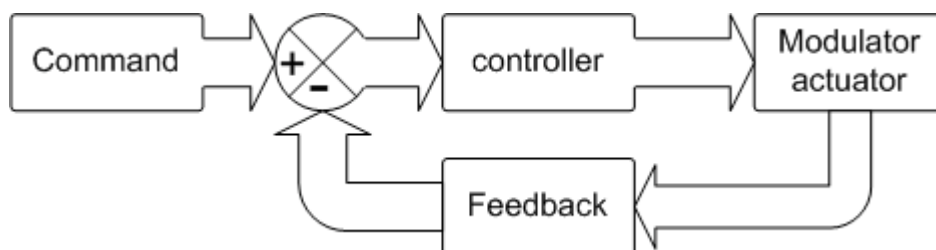


Figure 26: Servo control loop.

3.5.2.1 Command

In the case of a step scanning system as it is presented in this document, the command to the servo control loop is the desired position. The local Control Electronic will manage the sequencing and synchronisation of the system sampling. It will change the command of the servo control loop to move the interferometer to the next OPD interval. Figure 27 shows an example of sampling sequencing.

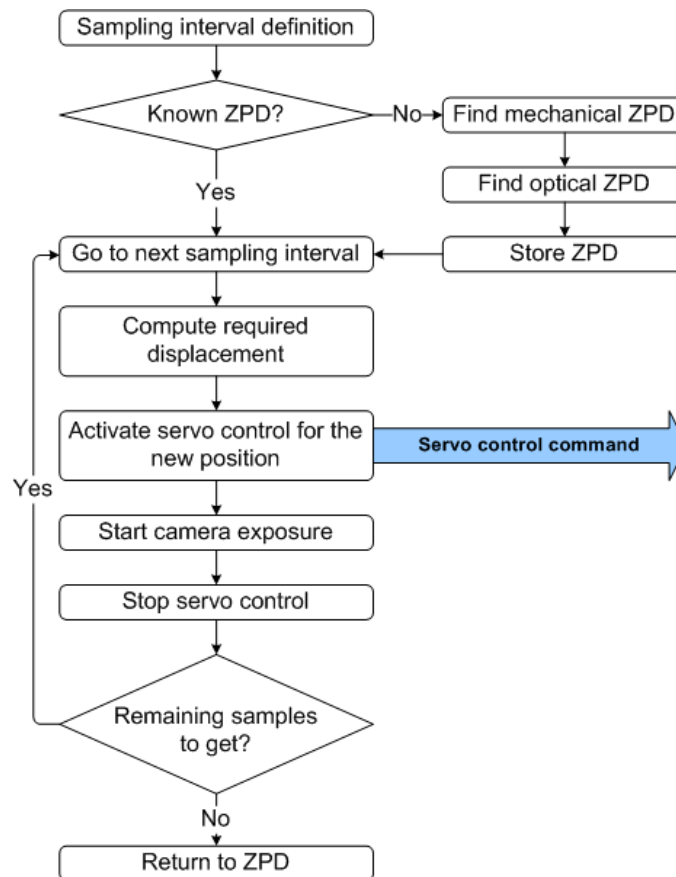


Figure 27: Sampling sequencing.

3.5.2.2 Controller

The controller is the core of the servo control loop. It tries to keep the error between the requested and the real position as small and stable as possible. In the case of SITELLE, the controller will be digital to allow more flexibility on the control algorithm. It is planned to use a standard PID position control, but the digital controller will allow us to optimise the system as we wish. The chosen controller has to be fast enough to not introduce phase lag in the servo control loop.

3.5.2.3 Actuator and Drive

The modulator actuator has to provide enough force to maintain the position of the system in case of disturbance. Another important aspect is the resolution of the actuator drive. If the resolution of the

actuator drive is lower than the rest of the servo loop resolution it will cause dither and affect the positioning performances.

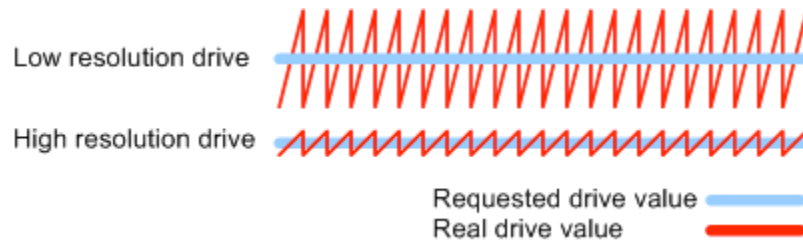


Figure 28: Effect of increasing actuator drive resolution.

3.5.2.4 Feedback

In FTS the OPD feedback is given by a modulated mono-mode laser. The polarized laser beam is sent in the interferometer and in order to be able to determine the OPD scan direction, a retardation plate is placed in one arm of the interferometer at an angle of $\pi/4$ to the polarization direction of the laser. After the plate, two polarization encoded light signals are observed with a known OPD mismatch. After recombination with the light traveling in the other arm, the two signals are split by the polarization cube and detected by two separated detectors.

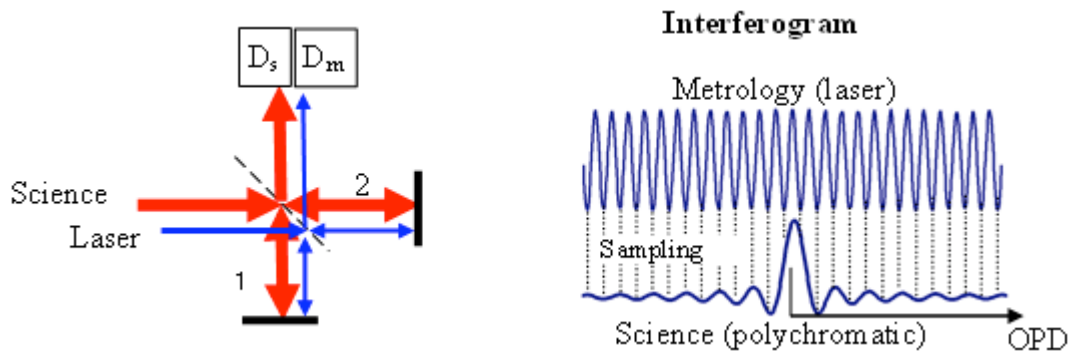


Figure 29: Modulated laser reference vs science signal

In order to improve the servo control performance we have to work on three main feedback parameters: Accuracy, resolution and responsiveness.

The accuracy can be improved using a shorter wavelength reference. As an example, instead of using an infrared laser source, an ultraviolet laser source can be used. The main drawback of this method is the availability of shorter wavelength stable laser sources and, most importantly, the sensitivity of the science detector to laser straylight. A more suitable approach is to have a multiplication factor between the reference source wavelength and the observed interference pattern. One way to achieve this is to force multiple passes of the laser beam inside the interferometer cavity. This effect is well known in interferometry and happens when science light reflects off the detector window and is sent back into the interferometer. A low intensity ghost spectrum can then be observed superimposed on the base signal at twice the original frequency. By sending all of the laser light back into the interferometer, using

retroreflectors, the observed interference pattern recorded after the second pass will exhibit modulation at twice the frequency, thus enhancing intensity variation to OPD sensitivity. Note that the double modulation problem in the science path can easily be overcome using a combination of AR coating and window tilt. The difference between the optical path traveled by the reference laser beam compared to the one traveled by the science signal will be multiplied by the number of passes in the interferometer. More optical path difference is generated in the metrology channel compared to the science signal for the same mechanical displacement.

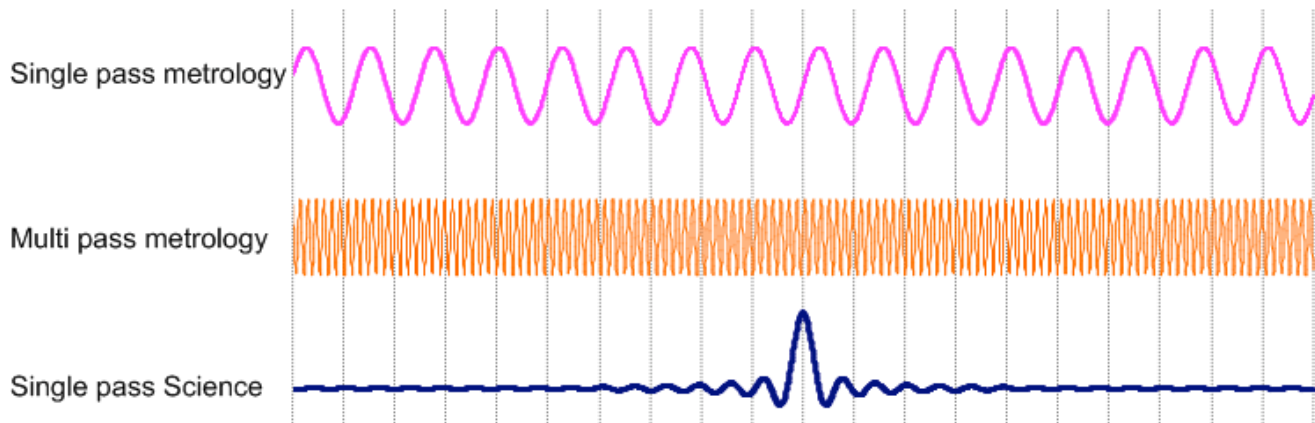


Figure 30: Multi-pass laser reference.

The resolution is the quantification of the position produced by the laser reference detection circuit. The conventional approach used in FTS to quantify the position is to detect the zero-crossing of the sinusoidal wave generated by the reference laser interference pattern. Since with this method the resolution is limited by the reference wavelength, this is not suitable to control the position of the interferometer in step-scan mode. The solution to enhance the resolution is to digitalize the sine wave generated by the source interference pattern with an analog to digital converter (ADC). Then knowing the sine wave's maximum amplitude and the current amplitude, the phase can be extracted. The more ADC resolution you have, the more position resolution you will get. Using 20 bits ADC will give about 1 million times more resolution than conventional methods.

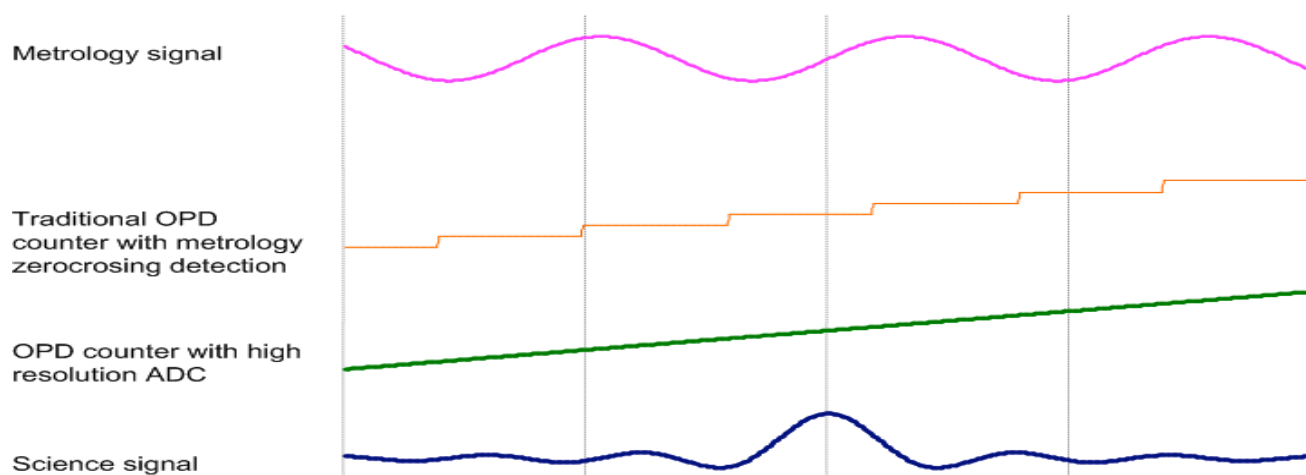


Figure 31: Resolution Enhancements.

The responsiveness of the feedback device can be improved using low delay circuits and high speed ADCs. A trade off should be made between the ADC resolution and its latency.

3.5.2.5 Interferometer Control Summary

A stable OPD position control is important to achieve high instrument performances. It implies a high performance controller, an accurate high resolution feedback, and a high resolution motor driver.

ABB Bomem started to work on digital servo control loop in the early 90's and has enhanced it through the years. Several servo control loops were developed that cover the needs for fast scanning interferometers (30cm/second) as well as low speed scanning (0.03cm/second) and step scanning. The standard ABB Bomem control board already supports all these modes with good performances.

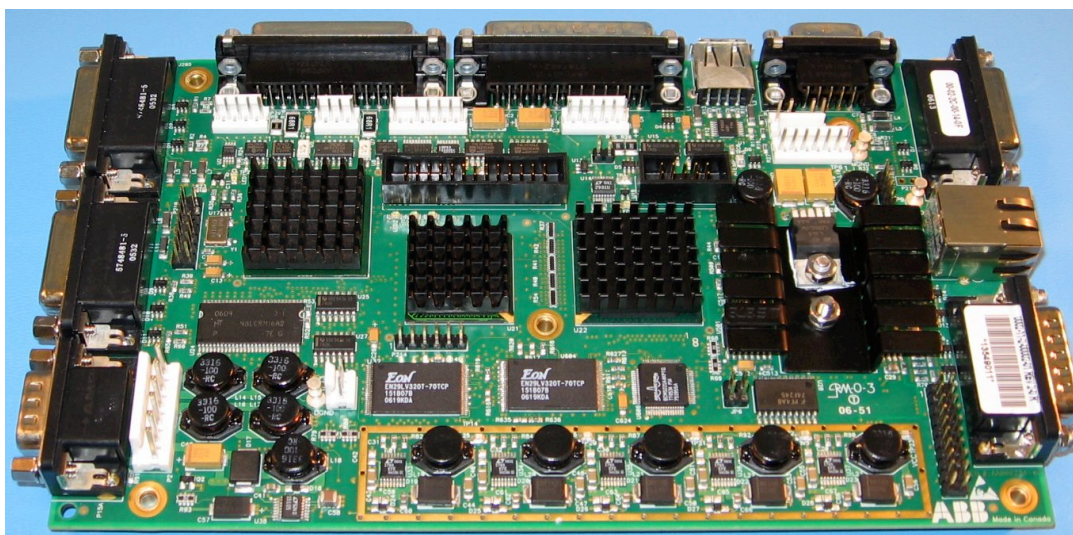


Figure 32: Standard ABB Bomem control board

The servo loop used in SpiOMM is a derivative of the one present in the standard ABB board which had much less maturity. Several new ideas were tested, some with mitigated success. A customization was suggested at that time due to the more complex nature of the servo tasks: OPD and Tip-Tilt corrections. The metrology laser approach was of novel design, a mean to feed the three required feedbacks simultaneously. The CC in SITELLE and their insensitivity to alignment allows the use of ABB standard servo systems.

The optimization of our standard line of control loop and electronics is always viewed as a work in progress at ABB. Recent efforts are under way to enhance the performances of the servo control loop. ABB Bomem currently works under two Canadian Space Agency programs to improve servo control loop robustness and stiffness. One of the programs will enable us the opportunity redesign our current electronics to improve the feedback and the motor drive. The other program allows us to work on new digital controller algorithms that will allow us to be more robust in case of external disturbances for slow speed scanning application. The objective of this latter program has recently been extended to also cover the step scan test cases in light of the SITELLE opportunity. These two enhancements will benefit all ABB Bomem products including the SITELLE instrument.

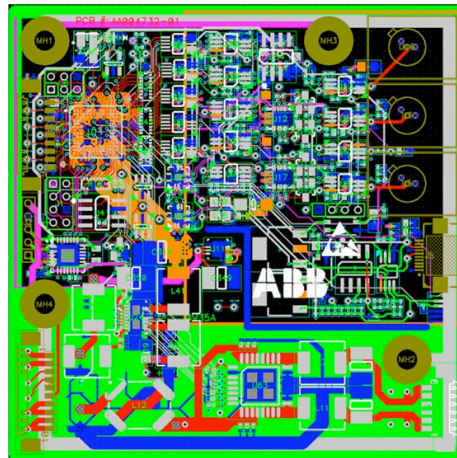


Figure 33: New ABB Bomem control board developed under CSA programs.

3.5.3 Cameras

No emphasis has been made in the study to the selection or development of the cameras as it is covered by other team members. The VersArray 2048B from Princeton Instruments was used as the baseline in the study. This camera has 2000×2000 pixels with a low readout noise and dark current.

3.6 KEY FEATURES SUMMARY

The current design meets all of the science derived instrument requirements:

- 1) **Dual-port:** 2 cameras are used to collect all the incident light.
- 2) **Image quality & FOV:** Panchromatic spot size with FWHM < 1" on a circular 14.4' field.
- 3) **Spectral Range:** from 350 to 950 nm, which include the [OII] line at 372.7 nm.
- 4) **Resolution:** The scan mechanism travel range allows to reach a spectral resolution of 2 cm⁻¹.
- 5) **Mechanical allocation:** The proposed concept meets volume, mass and torque allocation with reasonable margin.
- 6) **Humidity:** No optical parts are hydroscopic. Instrument enclosure is sealed and can be purged if needed.
- 7) **Operational Temperature:** All components are compatible with the operating temperature range of -15 to 10 °C. Performances of interferometer optical components at low temperature need to be further assessed in the next phases.

It should be pointed out that no SNR specification was defined. The current approach has been to treat this aspect as a best effort goal throughout the design development. The SNR performance model generated by ABB thus incorporates the presented subsystems performances and was used by the science team to evaluate the true potential offered by SITELLE.

3.6.1 Key improvements over SpIOMM

The SITELLE instrument proposed designs build on the lessons learned with the design, manufacturing, testing and operation of the SpIOMM instrument which has produced amazing results so far. It was said in the introduction (page 3) that the SITELLE requirements were in general very similar to the ones of SpIOMM. It could be then questioned as to why the final design presents such fundamental differences with SpIOMM, especially for the modulator. The easy answer to this is beam size and mass allocation. The Mégantic weight limit of 130 kg makes it very difficult if not impossible to fit a derivative of the SITELLE proposed design (CC based 4-ports configuration). Also the developments of suitable performance CC was judged too risky back in 2000 given the much smaller budget or realisation. Plane mirrors were a much more logic choice and allowed to explore new metrology & servo approaches.

In summary, the SITELLE instrument is expected to have the following improvements over SpIOMM:

- 1- SITELLE collects 7x more photons than SpIOMM
- 2- Imaging with more than 2x more pixels
- 3- A 40% increase in FOV
- 4- "Interferometer aligned by design" will result in much more stable modulation efficiency (no need for tip-tilt corrections servo). This will directly transfer in spectral noise reduction (1:1 relation)
- 5- OPD scanning and servo are based on robust ABB standard electronic boards

- 6- Increased metrology precision (2x to 4x more sensitive) through the use of the double modulation technique.
- 7- Single plate Beamsplitter/recombiner/compensator prevents ghost images and increases transmittance
- 8- Improved interferometer sealing
- 9- Metrology log during cube acquisition will enable the use of unevenly sampled interferogram correction algorithm (reduced noise)
- 10- OPD actuator compliant with temperature range

Another very important aspect to consider is the ease of operation of the instrument. The current design intent remains to manufacture an instrument with the same reliability and ease of use as other standard or custom instruments sold by ABB. The SITELLE instrument is not considered a R&D project. In the case of SpIOMM, the project aimed at developing promising new technologies and as such, the reliability aspects was in some cases deliberately treated second to the desire to explore the limits of the IFTS capabilities to generate valuable science. The institutional/pedagogic context of realisation of the SpIOMM instrument also influenced to adopt a more open architecture approach which would facilitate rework and evolution. Most of ABB standard FTS systems are used for quality control in industries and operated by individuals knowing very little about interferometer or even spectroscopy in general. These customers generally look for very precise quantitative absolute measurement of a given molecule concentration extracted from the spectral information. Instabilities or measurement errors can sometime have substantial financial impacts for our customer. Hence a successful relationship can only be guaranteed by very reliable and repeatable instrumentation which is one of ABB's biggest strength.

4. DEVELOPMENT REQUIREMENTS

4.1 FLOWDOWN

Figure 34 shows where the “flowdown” activity is located in the flow of design activities. The flowdown is the process of translating the User Requirements into System Requirements. This process is iterative by nature: the design process influences the flowdown, which can influence the instrument definition by the different analyses performed.

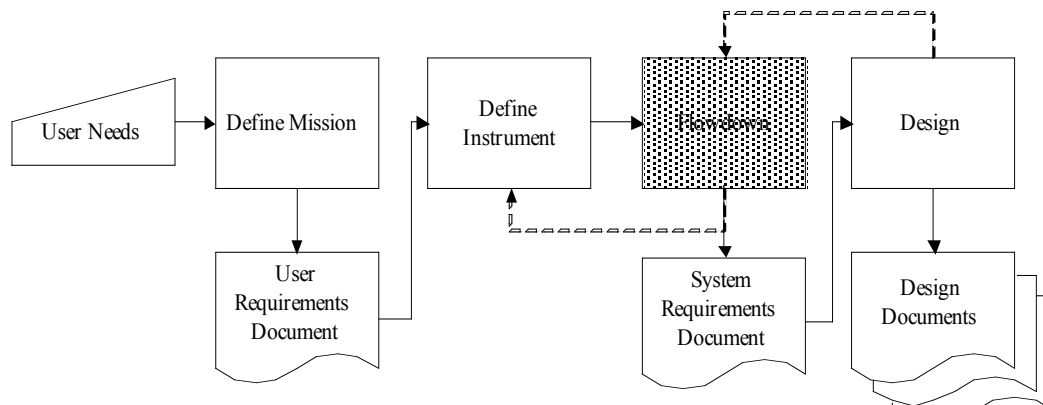


Figure 34: From user requirements to instrument design.

During the flowdown, parameters influencing performances and errors are mathematically linked to each other to estimate their mutual impact. Simulation of the instrument performance are done, finite element analysis are performed to estimate the impact of each design parameter. From this, it is possible to select the best design approach based on performances, cost, and risk to meet the user requirements.

The result of the flowdown is the creation of different budgets: error budget, mass budget, thermal budget, and optical alignment budget. Each budget is somewhat a summary of the analysis results that need to be done to construct them. They impose design guidelines and limits on what the design team can do to meet the user requirements.

4.2 RISKS

4.2.1 Overview

Table 4 lists the main risks associated with the development of the SITELLE instrument. Each risk is presented with a qualitative rating. The Impact column presents the consequence of a risk becoming a reality. The Mitigation present alternatives or activities that should be carried out in the following phases in order to further asses or reduce the risk rating.

Table 4: SITELLE Risk Register

Risk	Rating	Impact	Mitigation
1. Retroreflector manufacturability/ performance (flatness & beam deviation)	Medium	Low modulation efficiency hence poor SNR (riskier for short wavelengths)	Conduct prototyping activities in next phase. Unsuccessful results could suggest a fold back to SpIOMM flat mirror and dynamic alignment approach.
2 Poor AR coating performance at short wavelength (350–400 nm)	Medium	Reduced instrument efficiency. Risk for 372.7 [OII] line.	Procure test coupons with AR coating for the various glasses present to better assess the impact.
3. Sensitivity to operational vibration	Low / medium	OPD instabilities when CCD exposed degrading recorded modulation.	Obtain operational micro-vibration data at CFHT & careful FEA
4. Interferometer optics flatness (& transmitted wavefront) sensitivity to temperature variation	Low / medium	Degraded modulation efficiency at low temperature (riskier for short wavelengths)	ABB heritage for cold design (200K). Prototyping & testing of proposed B/S cell in phase B and CC in phase A.
6. Difficulties to meet optical design tight tolerance after integration	Low / medium	Degraded image quality	Explore less sensitive optical design in phase A (no aspheric lenses)
7 Sensitivity to refractive index variation in air	Low	Degraded modulation efficiency through non-uniform OPD across the pupil. (Riskier for short wavelengths)	Interferometer sits in sealed enclosure. Conduct more detailed analysis of the impacts of running the system in vacuum
7. Poor OPD Servo performance	Low	Uneven sampling of the OPD grid.	The log of average OPD sampling positions can be used to correct interferograms
9. Incapacity to meet mass allocation	Low	Forced to compromise rigidity to meet allocation. Optical misalignment with telescope tracking	Use of composite material for structural parts.
10. Incapacity to meet volume allocation	Low	Constrain telescope pointing to avoid contacts between instrument and telescope structure	Use of additional folding mirrors in the optical path

The most obvious risk items are the development of suitable retro-reflectors and variations in the anticipated performance for short wavelength (many contributors in the table). These items should be looked at carefully in the next phase through the execution of the proposed mitigation plan.

Figure 35 shows how the instruments requirements relate to some of the listed risks. Instrument requirements determine the characteristics of “optics quality” and “beam size”. Those last two elements determine the configuration for the “beam splitter/recombiner” and the “retro-reflectors”. Finally, the instrument mass is dependant on all the previous choices. The “optics quality” is primarily dependant on the spectral range of the system which is a key requirement. However, the “beam diameter” is a design choice. Working on reducing the “beam diameter” may influence positively many of listed risks at the cost of complexity the optical design. It is not obvious at this level of development that we reached the best balance between those two items.

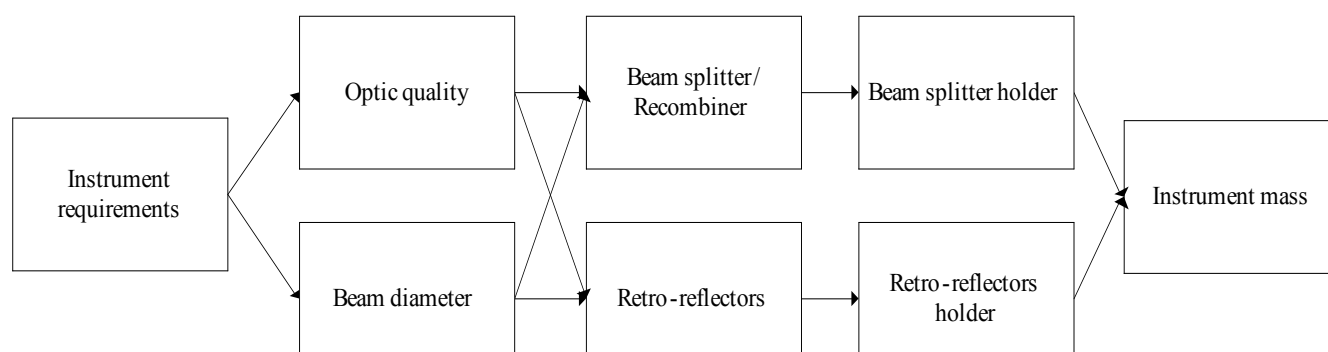


Figure 35: SITELLE’s influence flow

4.3 RISKS MITIGATION

4.3.1 Overview

Some obvious risks mitigation activities are proposed, while some aim at better assessing the risk rating:

- 1) Optical design optimization for beam diameter reduction.
- 2) Procurement of prototype CC.
- 3) More detailed FEM for the instrument or for some of its critical part compared against the optical tolerance budget
- 4) Update to the performance simulation model for predicting and evaluating impact of design choices on the science case.

4.3.2 I/O optic

New iterations in the design of the I/O optics is key to the reduction of the instrument size. The beam diameter is determined by the input optics. The input optics takes the incoming energy from the focal point of the telescope and collimates the incoming light in the modulator. The modulator can accept a

certain amount of divergence, which increases as the beam diameter is reduced. Current evaluation shows that the modulator can accept more divergence.

Two of the contributors for the modulation efficiency of the modulator are the tilt error and the shear error. Tilt error is amplified by the beam diameter, while the shear error is amplified by the divergence in the modulator which as stated is inversely proportional to the beam diameter. However, the sensitivity to shear error (hence larger divergence) is negligible because SITELLE is an imaging FTS (the influence of the shear error is divided by the 2000 pixels). There is no such simplification for the tilt error impact which can only be reduced by using a smaller beam or improving the CC residual tilt error itself (also referred to as beam deviation).

The beam diameter can be reduced from 120 mm to 80 mm without modulation and spectral resolution degradation. It is expected that the optical design will become more demanding as we reduce the beam size thus reducing the image quality at the edge of the FOV. Nevertheless, it is possible that the benefits outnumber the disadvantages that will appear. Further optimization is needed to select the best beam diameter for the selected design. Further studies are also required to identify possible substitute to SF1.

4.3.3 CC approach

One option for the filled glass CC approach is to use fused silica. The size of raw material blanks is limited. This may constrain the size of fused silica retro-reflector. Also, material homogeneity must be investigated. Different homogeneity grades exist, and studies must be performed to identify the best options.

4.3.4 Instrument Mass

Because of their size, the retro-reflectors impose some design limitations and constraints.

4.3.5 Finite Element Analysis

Detailed FEA will allow to assess or mitigate some of the perceived current risks. Mechanical deformations will be estimated as the gravity field orientation and temperatures change and will be used to evaluate the impact on the optical performance.

4.3.6 Performances Simulation

Performances simulation is another key element for success. A first performance model of the instrument already exists. It is essential to update the model as more precise information is obtained on the sub-system or component performance. This model will have to evolve during development in order to reassess the validity of the science case.

5. DEVELOPMENT ROADMAP AND FIRST COST ESTIMATE

Development project goes through a life-cycle which allows efficient management of cost, quality and schedule. For space-related projects and projects of this order of magnitude, a scheme widely used by agencies and large companies, divides it into the following phases:

- Phase A : Concept Phase with feasibility studies
- Phase B : Definition and Design
- Phase C : Development
- Phase D : Manufacturing

Each phase ends with a review with the customer and allows feedback/follow-up of progress.

Phase A ends with the concept review. It ensures with all stakeholders (users, customers and developers) that the requirements are understood, complete, needed, prioritized, etc...and that the concept is compliant with them. Phase B ends with a preliminary design along with a compliance w/r to requirements. Phase C ends with the final design review which allow the start of procurement. Phase D ends with the acceptance of manufactured and tested instrument.

ABB's product internal development process (management and engineering) is based on it and is illustrated in the figure below. The process has a large heritage since it was used several times on internal and external R&D projects with success.

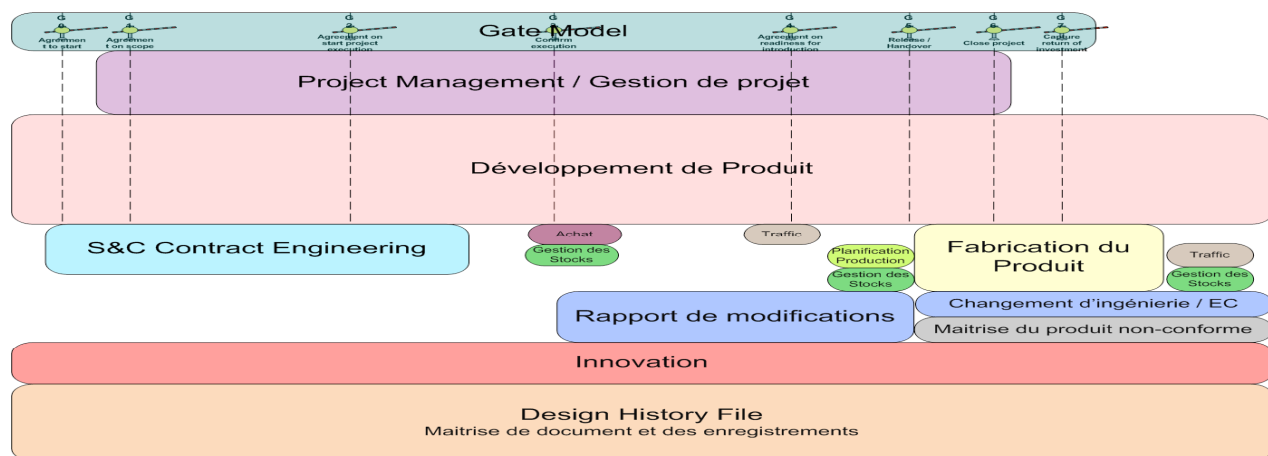


Figure 36: Product development process

Schedule and cost estimation are tied to the development cycle and are presented in the following sections.

5.1 SCHEDULE

Table 5 contains the proposed main milestones along with their expected dates for the SITELLE instrument. Durations are based on similar past projects and planned resource availability (human and material). We have assumed here that the project will start in January 2009.

Table 5: Project milestones

Event	Delay from start	Expected date	Comment
Kick-off	T0	January 2009	Start of phase A
System requirement review	T0 + 3 months	April 2009	
Final concept review	T0 + 6 months	July 2009	Start of Phase B
Preliminary design review	T0 + 13 months	February 2010	Start of Phase C
Critical design review	T0 + 21 months	October 2010	Start of Phase D
Manufacturing readiness review	T0 + 24 months	January 2011	
Test readiness review	T0 + 27 months	April 2011	
Pre-ship review / Shipping	T0 + 30 months	July 2011	

5.2 FIRST COST ESTIMATE

WITHDRAWN FROM PUBLIC RELEASE OF THIS DOCUMENT

— End of document —